Surface Wave Analysis in Laterally Varying Media

Politecnico di Torino

Paolo Bergamo

Surface Wave Analysis in Laterally Varying Media

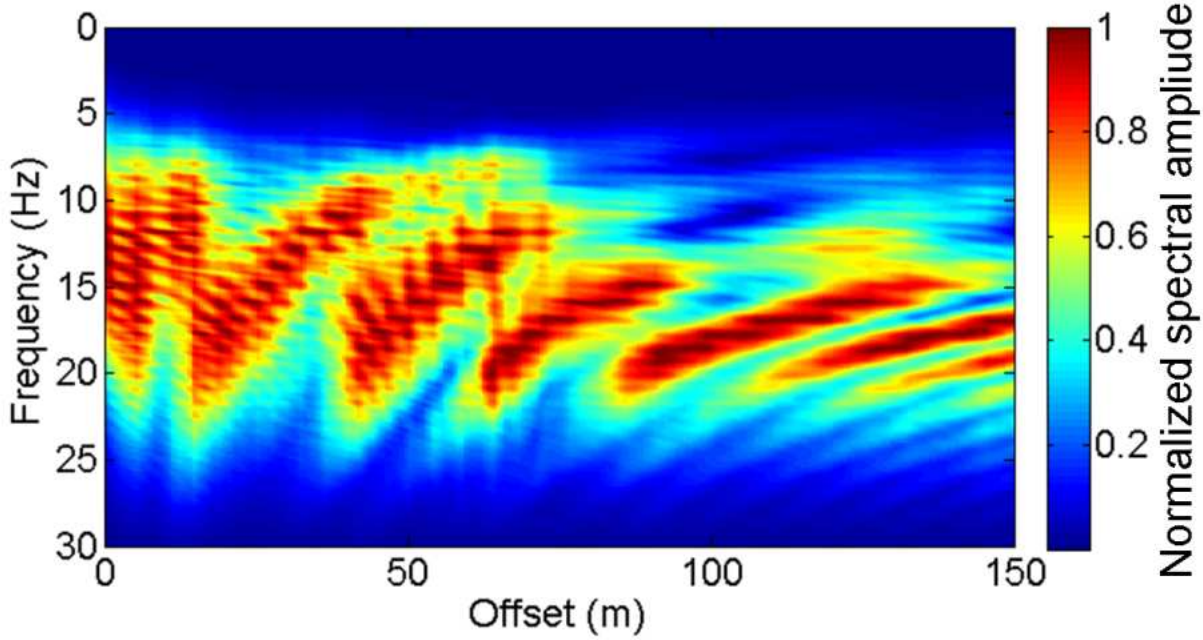

Ph.D. in Water and Territory Management Engineering

Ph.D. in Water and Territory Management Engineering (XXIV)

Politecnico di Torino
First School of Engineering

Surface Wave Analysis in Laterally Varying Media

Author:
Paolo Bergamo

Advisors:
Prof. Laura Valentina Socco
Prof. Sebastiano Foti

Head of the Ph.D. programme in Water and Territory Management Engineering:
Prof. Claudio Scavia

February 2012

Create the truth that you wish to know; and I, in knowing the truth that you have proposed to me, will make it in such a way that there will be no possibility of my doubting it, since I am the very one who has made it.

"Seeing knowing", 2004, Castello di Rivoli.
Joseph Kosuth quoting Giambattista Vico

ACKNOWLEDGEMENTS

I would like to thank all the people I happened to get to know and I've been working with during the past three years, who helped me with suggestions, doubts, corrections and new ideas, or simply with their company.

Thanks are therefore due to Hansrudolph Maurer and Ilaria Coscia from ETH Zurich, for welcoming and hosting me during my stay in Switzerland. Thanks also to the students of the Joint Master in Applied Geophysics, for the pleasant time spent together.

Thanks to Giampiero Bianchi, for his help during the L'Aquila and Sicily campaign.

Thanks to Ken Tokeshi for his friendship and patience in sharing a cold office in winter and a hot office in summer.

Thanks to Stefan Carpentier from ETH Zurich for involving my research group into the New Zealand-Alpine Fault project.

Thanks to Ludovic Bodet for his hospitality during my visit at Université du Maine and his willingness in introducing me to small-scale experiments and sharing his great expertise. Thanks also to Régis Mourgues and Vincent Tournat for their valuable suggestions.

Thanks to Renato Orta, Luigi Sambuelli, Alberto Godio and Cesare Comina for their advice, available whenever required.

Thanks to Marguerite Jones, for her kindness and help in improving my knowledge of English.

Thanks to all the people I've worked with at the Environmental Geophysics Laboratory of Politecnico di Torino, for their continuous help and the pleasure to work in a very nice environment: Diego Franco, Alessandro Arato, Flora Garofalo, Silvia Bava, Erika Paltrinieri, Claudio Piatti, Roberto Rege, Daniele Boiero, Margherita Maraschini, Stefano Stocco, Emanuele Bena, and Corrado Calzoni.

ABSTRACT

This work studies the possibility of using surface wave analysis as a tool for a robust estimation of the S-wave velocity behaviour in laterally varying media. The surface wave method, in fact, can be effectively adopted for different purposes and at different scales, but I focused on the geo-engineering and geotechnical applications of surface wave analysis and also on the production of near-surface models for deep exploration: in both cases the aim is to retrieve the trend of the S-wave velocity in the first tens up to hundreds meters of depth of the subsoil. The surface wave method exploits the geometric dispersion proper of surface waves: in a non-homogeneous medium every frequency is characterized by a different phase velocity, as every frequency component travels through a portion of medium whose thickness is proportional to its wavelength. The curve associating every frequency component to its phase velocity is called dispersion curve, and it constitutes the experimental datum one uses for the solution of an inverse problem to estimate the behaviour of S-wave velocity in the subsurface. The inversion is performed by assuming a 1D forward modelling simulation and suffers from equivalence problems, leading to the non uniqueness of the solution. Despite its great ductility, the main limitation of surface wave method is constituted by its 1D approach, which has proved to be unsatisfactory or even misleading in case of presence of lateral variations in the subsoil. The aim of the present work is to provide data processing tools able to mitigate such limitation, so that the surface wave method can be effectively applied in laterally varying media.

As far as the inadequacy of surface wave method in case of 2D structures in the subsoil, I developed two separate strategies to handle smooth and gradual lateral variations and abrupt subsurface heterogeneities. In case of smooth variations, the approach I adopted aims at "following" the gradual changes in subsoil materials properties. I therefore propose a procedure to extract a set of neighbouring dispersion curves from a single multichannel seismic record by applying a suitable spatial windowing of the traces. Each curve corresponds to a different subsoil portion, so that gradual changes in subsoil seismic parameters can be reconstructed through the inversion of dispersion curves. The method was tested on synthetic and real datasets, but proved its reliability in processing the data from a small scale seismic experiment as well. In the context of characterizing smooth 2D structures in the subsurface via the surface wave method, I also developed a procedure to quantitatively estimate the (gradual) lateral variability of model parameters

by comparing the shape of local dispersion curves, without the need to solve a formal inverse problem. The method is based on a sensitivity analysis and on the applications of the scale properties of surface wave. The procedure can be devoted to different applications: I exploited it to extend a priori local information to subsoil portions for which an experimental dispersion curve is available and for an estimation of the lateral variability of model parameters for a set of neighboring dispersion curves. The method was successfully applied to synthetic and real datasets.

To characterize sudden and abrupt lateral variations in the subsurface, I adopted another strategy: the aim is to estimate the location and embedment depth of sharp heterogeneities, to process separately the seismic traces belonging to quasi-1D subsoil portions. I adapted several methods, already available in literature but developed for different purposes and scales, to the detection of sudden changes in subsoil seismic properties via the analysis of anomalies in surface wave propagation. I got the most promising results when adapting these methods, originally developed for single shot configurations, to multifold seismic lines, exploiting their data redundancy to enhance the robustness of the analyses.

The outcome of the thesis is therefore a series of processing tools that improve the reliability and the robustness of surface wave method when applied to the near surface characterization of laterally varying media.

CONTENTS

INTRODUCTION

Surface wave (SW) method has progressively established as an effective and reliable tool for the estimation of the mechanical properties of subsoil and materials. Its ductility has given birth to a wide range of applications, for different scales and purposes: from micro to macro scales, ultrasonic surface waves are exploited to identify material defects (Scales and Malcolm 2003), while seismologists use surface waves produced by earthquakes to investigate the structure of the earth's crust and of the upper layers of the mantle (see for instance Trampert and Woodhouse 2005). At intermediate scales, geophysicists and geo-engineers make use of surface wave for the estimation of S-wave velocity in the first tens or hundreds of meters of the subsurface. This particular field has in turn a great number of applications: surface waves are used for the characterization of the near surface weathering layers in seismic hydrocarbon exploration (Bohlen et al. 2004), but also for the estimation of the dynamic behaviour of soils in structural engineering. As for the latter application, SW method has nowadays become a standard for seismic risk assessment studies, and has involved part of the activity of my doctorate (Bergamo et al. 2011, Foti et al. 2011). Despite this great variety of purposes, all applications exploit the same property of SW, that is the geometric dispersion which occurs when surface waves travel through a non-homogeneous medium (Socco and Strobbia 2004). Different kinds of surface waves can be generated and therefore analyzed (Love waves, Scholte waves, P-guided waves) but generally SW method exploits Rayleigh waves, which are easily generated and/or recorded on the ground surface.

All surface wave analysis applications share the same procedure, which is based on three successive steps:

1) acquisition of the experimental data. Recorded signal can be either generated by an active source (active methods) or by ambient noise or earthquakes (passive methods);

2) acquired data are then processed to extract the experimental dispersion curve, that is a curve expressing the relationship between the frequencies and their respective phase velocities, caused by the geometric dispersion proper of SW. The dispersion curve can comprise more than one propagation mode;

3) finally, the experimental dispersion curve undergoes an inversion process through which model parameters are estimated.

According to the scale and the application, these three steps can be achieved following different approaches. However, for geotechnical and geo-engineering applications, which are of greater interest for this work, the acquisition is performed with a multichannel array of vertical low-frequency geophones: the recorded seismogram is then converted to the frequency-wavenumber (*f-k*) or frequency-slowness (ω-*p*) domain, where the energy maxima are identified to extract the experimental dispersion curve. As far as the inversion is concerned, it exploits 1D forward modelling to estimate a 1D S-wave velocity profile. Notwithstanding its great ductility, the SW method is however characterized by a 1D approach which might prove unsatisfactory, and sometimes misleading, when the method is applied in 2D environments (Semblat et al. 2005).

In literature some strategies to overcome this limitation are present. A first strategy is based on a spatial windowing of the seismic traces (Bohlen et al. 2004; Boiero and Socco, 2011), so that the dispersion curve becomes a local property of the subsoil beneath the receivers whose traces are weighted more. This solution can be successfully and effectively adopted in case of smooth lateral variations: if the spatial window is successively shifted along the seismic profile, a set of dispersion curves can be extracted and the gradual change in subsoil seismic parameters can be reconstructed with a laterally constrained inversion of the dispersion curves yielding a pseudo-2D section of the shear wave velocity in the subsurface (Socco et al. 2009, Bergamo et al., 2010). In case of sharp and sudden 2D effects in the subsurface, another strategy should be preferred: it consists in estimating the location of discontinuities in seismic parameters of the subsoil and in processing separately seismic traces belonging to quasi-1D subsurface portions (Vignoli and Cassiani 2010, Vignoli et al. 2011).

As for the last stage of SW analysis, that is the experimental dispersion curve inversion, different approaches have been developed. Most of them adopt deterministic (or local search) inversion techniques , that imply an iterative updating of the initial model based on the computation of partial derivatives. Being the data-model relationship for SW strongly non linear, the inversion suffers from equivalence problems (Tarantola 2005, Foti et al. 2009): great care must then be paid when choosing the initial model, as the non-uniqueness of the solution makes the inversion result very sensitive to it, driving the inversion towards local minima if the initial model is not correct (Sambridge 2001, Luke et al. 2003 and Wathelet 2005). The issue can then be faced by preferring a global search method inversion algorithm, which is able to highlight the presence of equivalence problems by providing a set of solutions equally satisfying the experimental

data. A global search approach, however, implies greater computational costs with respect to deterministic inversion methods (Socco et al. 2010). The robustness of SW inversion can be significantly improved by exploiting a priori information and/or other geophysical data available for the investigated site to produce a reliable initial model for local search algorithms or run a constrained or joint inversion (Wisèn and Christiansen 2005 and Schuler 2008). A similar strategy is also applied by laterally constrained inversion (LCI) algorithms, where a set of dispersion curves is inverted simultaneously and each 1D model is linked to its neighbours with mutual constraints to provide a single pseudo-2D model, thus increasing the robustness of the inversion process. Laterally constrained inversion, in particular, has proven to be an effective tool for the inversion of a set of neighbouring dispersion curves (Socco et al. 2009).

The research activity that is presented in this work is mainly devoted to analyse and mitigate the inability of SW method to adequately investigate lateral variations in the subsoil. I separately approached the problems arising from smooth, gradual 2D structures in the subsoil and from sharp lateral heterogeneities. As far as smooth lateral variations are concerned, I adopted the strategy to locally focus the investigation and to follow the gradual changes of subsoil seismic properties. The approach providing a local focusing of the examination has been chosen, among others, by Bohlen et al. (2004) who propose to spatially window the seismic traces: traces amplitudes are suitably weighted, to mitigate the effect of lateral variations and to centre the investigation within a certain spatial range. In this way the dispersion curve becomes a local property of the subsoil beneath the receivers whose traces are weighted more. I have set up a procedure to retrieve 2D structures from SW acquired with a limited number of receivers, for engineering or geotechnical purposes (Bergamo, Boiero and Socco 2010). My technique is based on a two-step process:

1) extraction of several local dispersion curves along the survey line using a spatial windowing based on a set of Gaussian windows with varying shape whose maxima span the array line;

2) inversion of the retrieved set of dispersion curves using a laterally constrained inversion (LCI) scheme based on a pseudo-2D model parameterisation together with 1D forward data simulation.

Another procedure I developed to face smooth lateral heterogeneities in the subsurface allows to quantitatively estimate the lateral variability of model parameters by comparing the shape of local dispersion curves, without the need to perform their

inversion. The algorithm is based on a sensivity analysis and on the applications of the scale properties of surface wave (Maraschini et. al 2011). The procedure can be devoted to different applications: I exploited it to extend a priori punctual information to subsoil portions for which an experimental dispersion curve is available and for an estimation of the lateral variability of model parameters for a set of neighbouring dispersion curves. The first application allows to produce a consistent initial model based on a priori information accustomed according to local SW data; the evaluation of the expected spatial variability of model parameters was used to provide a data-consistent setting of the lateral constraints for a laterally constrained inversion (Boiero et al. 2009).
As for handling sharp and abrupt subsoil heterogeneities, instead, I adopted a different strategy: the aim is not following smooth gradual variations but identifying the location of sudden discontinuities to process separately the traces belonging to quasi 1D subsoil portions (see for instace Vignoli et al. 2010). For this purpose, I tested the applicability and the effectiveness in retrieving discontinuities in the subsoil of three methods, all of them exploiting the detection of anomalies: multi-offset phase analysis of surface wave (MOPA, introduced by Strobbia and Foti 2006), autospectrum method (described by Zerwer et al., 2005) and the attenuation analysis of Rayleigh waves (AARW, Nasseri-Moghaddam et al., 2005). Although already available, these methods were originally developed for different purposes and different scale problems: therefore, I tested them on the same synthetic and real dataset, both of them characterized by the presence of a fault perpendicularly crossing the array line (Bergamo and Socco 2011).
The aforementioned methods were implemented in Matlab ® and were first tested on synthetic datasets and later applied to real data. In one case, the algorithm was also tested on seismograms derived from a small-scale seismic survey performed on a physical model.
As for the synthetic datasets, they were produced to verify the applicability of the developed algorithms and to test their effectiveness in facing different kinds of lateral heterogeneities. I adopted several methods to generate the synthetic data: finite element method (FEM) and finite difference method simulations were performed, but I also used a code implemented at Politecnico di Torino (Boiero 2009) able to model semi-analytically only the Rayleigh wave propagation through a layered medium. As already mentioned, I also processed a dataset obtained from a small-scale seismic survey performed on a physical model. The experiment was performed at the Acoustics Laboratory of the Université du Maine, in Le Mans, France. The small scale model was

constituted by granular materials and the acquisition was obtained with a laser-Doppler interferometer: thanks to a proper choice of the materials, grain size and deposition process, I managed to produce a layered medium characterized by a 2D geometry. Small scale experiments are in fact gaining popularity in surface wave analysis literature because they allow to perform measurements on models whose geometry and mechanical properties are known and, at the same time, they are able to yield datasets whose quality is not far from the real case acquisitions (their datasets are therefore more realistic than those derived from numerical simulations: see for instance Campman et al. 2005 and Bodet et al. 2010). The methods developed for the present work were eventually applied to real cases. Again, I used different kinds of field data: I exploited MASW (multichannel analysis of surface wave) acquisitions, but also seismic reflection surveys, performed in both cases for seismic risk assessment studies.

REFERENCES

Bergamo P., Boiero D., Socco L.V. 2010. Retrieving 2D Structures from Surface Wave Data by Means of a Space-varying Spatial Windowing, In: EAGE Near Surface 2010, EAGE Near Surface 2010, Zurich, Switzerland. 6-8 September 2010.

Bergamo P., Comina C., Foti S., Maraschini M. 2011. Seismic characterization of shallow bedrock sites with multi-modal Monte-Carlo inversion of surface wave data. Soil Dynamics and earthquake engineering, 31, pp 530-534.

Bergamo P., and Socco L.V. 2010. Localizzazione di discontinuità laterali tramite l'analisi degli spettri di potenza e di fase delle onde superficiali. In: Proceedings of XXX GNGTS, 30th GNGTS, Trieste, 14-17 November 2011.

Bodet L., Jacob X., Tournat V., Mourgues R.and Gusev V.2010. Elastic profile of an unconsolidated granular medium inferred from guided waves : toward acoustic monitoring of analogue models. Tectonophysics, 496, 99-104.

Bohlen, T., S. Kugler, G. Klein, and F. Theilen, 2004, 1.5-D Inversion of lateral variation of Scholte wave dispersion: Geophysics, **69**, 330-344.

Boiero D. 2009. Surface wave analysis for building shear wave velocity models. PhD. Thesis, Politecnico di Torino.

Boiero D., Bergamo P. and Socco L.V. 2009. Retrieving Consistent Initial Model for Surface Wave Inversion from Punctual a Priori Information, In: Proceeding of Near Surface Geophysics - EAGE, Near Surface Geophysics - EAGE Conference, Dublin 7 - 9 September 2009.

Boiero D.; Socco L.V. 2011. The meaning of surface wave dispersion curves in weakly laterally varying structures. Near Surface Geophysics, 6, 561-570.

Campman X., van Wikk K., Scales J.A. and Herman G.C. 2005. Imaging and suppressing near-receiver scattered surface waves. Geophysics 70, pp. V21-V29.

Foti S., Comina C., Boiero D., Socco L.V. 2009. Non uniqueness in surface wave inversion and consequences on seismic site response analyses. Soil Dynamics and Earthquake Engineering, 29, pp. 982-993.

Foti S., Parolai S., Bergamo P., Di Giulio G., Maraschini M., Milana G, Picozzi M., Puglia R. 2011. Surface wave surveys for seismic site characterization of accelerometric stations in ITACA. Bulletin of Eartquake Engineering, 9, 1797-1820.

Luke, B., C. Calderón, R. C. Stone, and M. Huynh, 2003, Nonuniqueness in inversion of seismic surface-wave data: Proceedings of Symposium on the Application of Geophysics to Engineering and Environmental Problems (SAGEEP), Environmental and Engineering Geophysical Society, Denver, CD-ROM SUR05, 1342-1347.

Maraschini M., Boiero D., Foti S., and Socco L.V. 2011 Scale properties of the seismic wavefield – perspectives for full-waveform matching. Geophysics 76, pp. 1-7.

Nasseri-Moghaddan A., Cascante G. and Hutchinson J. 2005. A new quantitative procedure to determine the location and embedment depth of a void using surface waves. Journal of Environmental and Engineering Geophysics 10, 51-64.

Sambridge, M., 2001, Finding acceptable models in nonlinear inverse problems using a neighbourhood algorithm: Inverse problems, **17**, 387-403.

Scales J.A. and Malcolm A.E. 2003. Laser characterization of ultrasonic wave propagation in random media. Physical Review E., 67, 046618

Semblat, J. F., M. Kham, E. Parara, P. Y. Bard, K. Pitilakis, K. Makra, and D. Raptakis, 2005, Seismic wave amplification: Basin geometry vs soil layering: Soil Dynamics and Earthquake Engineering, **25**, 529-538.

Schuler J. 2008. Joint inversion of surface waves and refracted P- and S- waves. M.Sc. thesis, ETH Zurich.

Socco L..V., Boiero D., Foti S. and Wisén R., 2009. Laterally constrained inversion of ground roll from seismic reflection records. Geophyiscs 74, pp 35-45.

Socco L.V., Foti S., and Boiero D. 2010. Surface-wave analysis for building near-surface velocity models – Established approaches and new perspectives. Geophysics 75, pp. A83 – A 102.

Socco, L.V., and C. Strobbia, 2004, Surface Wave Methods for near-surface characterisation: a tutorial: Near Surface Geophysics, **2**, 165-185.

Strobbia C. and Foti S. 2006. Multi-offset phase analysis of surface wave data (MOPA). Journal of Applied Geophysics, 59, pp. 300-313.

Tarantola A. 2005. Inverse problem theory and methods for model parameter estimation. Philadelphia, USA: SIAM.

Trampert J. and Woodhouse J.H. 1995. Global phase velocity maps of Love and Rayleigh waves 40 and 150 s period. Geophysical Journal International. 122, 675-690.

Vignoli G. and Cassiani G. 2010. Identification of lateral discontinuities via multi-offset phase analysis of surface wave data. Geophyiscal Prospecting., 58, pp.389-413.

Vignoli G., Strobbia C., Cassiani G. and Vermeer P. 2011. Statistical multi offset phase analysis for surface –wave processing in laterally varying media. Geophyics, vol. 76, no. 2, pp. U1-U11.

Wathelet, M., 2005, Array recordings of ambient vibrations: surface-wave inversion: Phd thesis Université de Liège – Faculté des Sciences Appliquées, France.

Wisén, R., and A. V. Christiansen, 2005, Laterally and mutually constrained inversion of surface wave seismic data and resistivity data: Journal of Environmental & Engineering Geophysics, 10, 251-262.

Zerwer A., Polak M.A. and Santamarina J.C. 2005. Detection of surface breaking cracks in concrete members using Rayleigh waves. Journal of Environmental and Engineering Geophysics, vol. 10, issue 3., pp. 295-306.

1 - RETRIEVING 2D STRUCTURES FROM SURFACE WAVE DATA BY MEANS OF A SPACE-VARYING SPATIAL WINDOWING

In this first chapter I introduce a processing technique I developed to reconstruct smooth lateral variations in the subsurface by means of the application of surface wave analysis. The technique is based on the spatial windowing of traces amplitudes, which allows to locally focus the investigation and, therefore, to "follow" gradual 2D structures in the subsoil, even when a limited number of shots is available.

ABSTRACT

Surface wave techniques are mainly used to retrieve 1D subsoil models. However, in 2D environments the 1D approach usually neglects the presence of lateral variations and, since the surface wave path crosses different materials, the resulting model is a simplified or misleading description of the site. We propose a processing technique to retrieve 2D structures from surface wave data acquired with a limited number of receivers. Our technique is based on a two-step process. First, we extract several local dispersion curves along the survey line using a spatial windowing based on a set of Gaussian windows with different shape; the window maxima span the survey line so that we are able to extract a dispersion curve from the seismogram for every window. This provides a set of local dispersion curves each of them referring to a different subsurface portion. This space varying spatial windowing provides a good compromise between wavenumber resolution and the lateral resolution of the obtained local dispersion curves. In the second step, we invert the retrieved set of dispersion curves using a laterally constrained inversion scheme. We applied this procedure to the processing of both synthetic and real data sets and the method proved to be successful in reconstructing even complex 2D structures in the subsurface.

INTRODUCTION

Surface waves (SW) analysis is usually applied to estimate 1D subsurface shear wave velocity (V_s) models. However, when applied in 2D environments this 1D

approach might prove unsatisfactory and, sometimes, misleading (Boiero and Socco, 2011). Indeed, in a fully 1D environment the dispersion curve represents the seismic properties of the subsurface, but the presence of lateral variations beneath the receiver spread affects the SW propagation and this should be accounted for when processing the data to retrieve the dispersion curves. Therefore, the question is: since the 1D approach neglects the presence of lateral heterogeneities, what is the retrieved dispersion curve representative of in case of 2D structures in the subsurface? Can we refer the dispersion curve to an "average" subsurface shear wave velocity profile or does it represent a particular portion of the investigated subsurface?

In the case of weakly laterally varying media, Boiero and Socco (2011) showed that, depending on the lateral variation pattern and wavenumber resolution of the measuring array, the dispersion curve, retrieved by applying wavefield transforms over the whole receiver spread, can be either representative of the average slowness along the propagation path or be definitely not representative of any portion of subsurface beneath the array. They also showed that in these cases the application of spatial windowing can make the dispersion curve representative of the local subsurface velocity beneath the window maximum. When strong and abrupt heterogeneities occur in the subsurface, they are likely to produce significant deviations of the SW path from the shortest path between source and receiver, with induced coupling between modal contribution (Strobbia and Foti, 2006). Lin and Lin (2007) have proven that artifacts can be introduced in 2D V_s imaging if the effect of lateral heterogeneity is not accounted for. In literature some strategies to apply SW analysis in case of lateral variations are available (Socco et al., 2010). A first strategy is to detect discontinuities in subsurface seismic parameters and to process separately seismic traces belonging to quasi-homogeneous subsurface portions. This can be achieved by several approaches (see for instance Nasseri-Moghaddam et al., 2005, Zerwer et al., 2005, Strobbia and Foti, 2006, Vignoli and Cassiani, 2009). Another strategy, of greater interest for this work, is based on the spatial windowing of the seismic traces: trace amplitudes are suitably weighted, to mitigate the effect of lateral variations and to focus the investigation within a certain spatial range. In this way the dispersion curve becomes a local property of the subsoil beneath the receivers whose traces are weighted more. Bohlen et al. (2004) proposed an approach based on a moving spatial window for processing and extracting dispersion curves which are then inverted to generate a 2D shear wave velocity pseudosection. They applied it to a marine data set acquired for exploration purposes and indeed,

methods based on a moving window may only be applied to very long survey lines, like those used in exploration seismic reflection. On the contrary, we propose a processing technique to retrieve 2D structures from SW acquired with a limited number of receivers, for engineering or geotechnical purposes (Bergamo et al., 2010). Our technique is based on a two-step process:

- extraction of several local dispersion curves along the survey line using a spatial windowing based on a Gaussian window with varying shape;
- inversion of the retrieved set of dispersion curves using a laterally constrained inversion (LCI) scheme based on a pseudo-2D model parameterization together with 1D forward data simulation. Auken and Christiansen (2004) first introduced LCI approach for the interpretation of resistivity data, and Wisén and Christiansen (2005) and Socco et al. (2009) successfully applied it to the inversion of SW data: LCI is a deterministic inversion in which each 1D model is linked to its neighbors with mutual constraints to provide a single pseudo-2D model.

We present the proposed method in the following section and then we apply it to synthetic and field data.

METHOD

We firstly outline the proposed technique and then we discuss the consequences of its application in terms of lateral resolution and wavenumber resolution of the retrieved dispersion curves.

The processing technique

In the case of both weak and sharp lateral variations below the survey line, the dispersion curve assumed as corresponding to a 1D subsurface profile might not be representative of the seismic characteristics of the subsurface: a strategy to mitigate this problem is to focus the dispersion curve estimation on the array centre to reduce the effects of the lateral variations and make the dispersion curve a local property of the subsoil beneath the array centre (Boiero and Socco, 2011). Bohlen et al. (2004) have suggested to window the seismogram in the spatial domain with a Gaussian window. We propose to substitute this symmetric window with the maximum in the centre of the receiver array, with several windows whose maxima span the array (Figure 1.1).

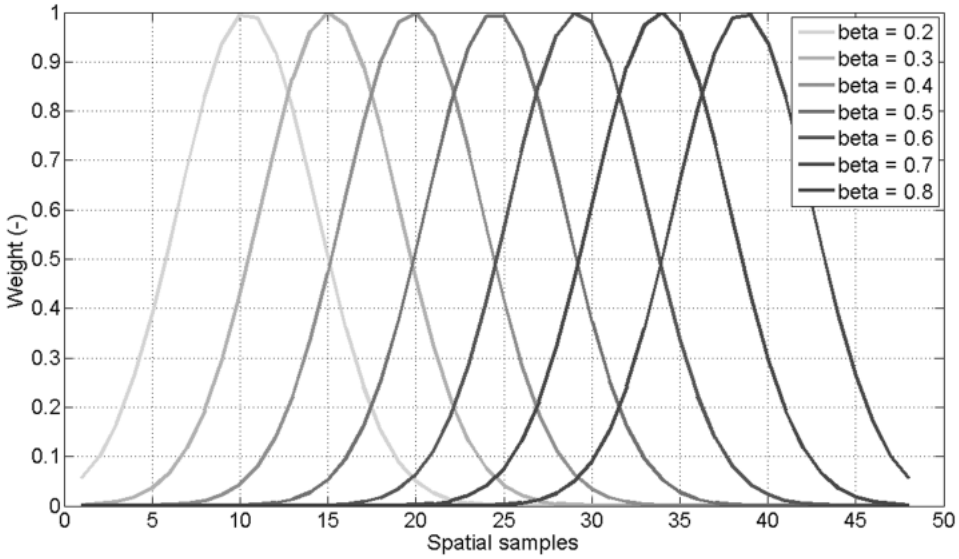

Figure *1.1 – Gaussian windows used for the spatial windowing of the seismogram. Parameter α is 6 for all windows, parameter β is different for each window.*

For every window we extract a dispersion curve from the seismogram thus retrieving a set of dispersion curves, each of them referring to a different subsurface portion. We use a Gaussian window defined as follow:

$$w_{k+1} = e^{-\frac{1}{2}\left(\alpha\frac{k-N\beta}{N/2}\right)^2} \quad k = 0,1,\ldots,N \tag{1}$$

where w is the weight that is assigned to the $k+1^{th}$ trace, N is the number of spatial samples minus one, β is a number ranging from 0 to 1 indicating the relative position of the maximum of the window with respect to the array length and $\alpha \geq 2$ is a parameter inversely proportional to the window standard deviation σ, as

$$\sigma = N/2\alpha \tag{2}$$

Note that parameters α and β define the shape of the window: α, in particular, is related to the width of the window (Figure 1.2), which controls the extent of the investigated portion of subsoil and, thus, the lateral resolution of the retrieved dispersion curves. The following section explains in detail how we need to choose parameter α to conceal the wavenumber resolution requirements of the related frequency-wavenumber (*f-k*) spectra and the desired lateral resolution of the dispersion curves.

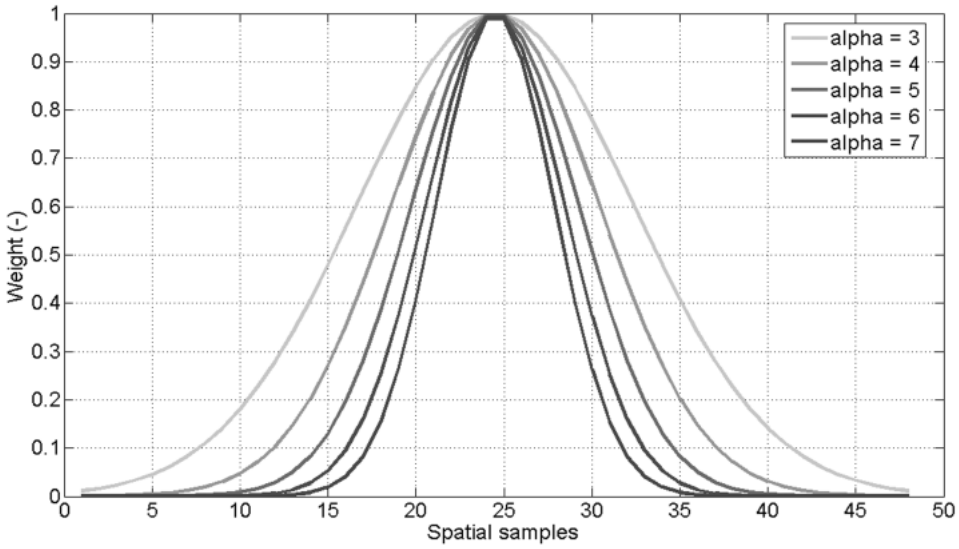

Figure 1.2 – Effect of parameter α on Gaussian windows shape. Parameter β is 0.5 for all windows, parameter α ranges from 3 to 7.

To summarize, we are able to extract several dispersion curves, each of them referred to a different subsurface portion, from the same seismogram by windowing it in space domain with a set Gaussian windows with constant α (i.e.: same Gaussian windows bell width) and increasing β values (i.e.: different positions for the windows maxima). We conventionally refer every dispersion curve to the position of the corresponding window maximum. Moreover, we do not take into consideration the Gaussian windows whose maximum is 2σ or less far from one of the ends of the receiver array to avoid the cutting of the window tails. If two or more shots are available for the same array position, we can stack the *f-k* spectra from different shots with the same spatial windowing, thus improving the signal to noise ratio (Grandjean and Bitri, 2006; Neducza, 2007): we then perform the picking of maxima on each stacked *f-k* spectra, obtaining higher quality dispersion curves.

We invert the set of dispersion curves obtained from the previously described procedure using a laterally constrained inversion (LCI) scheme based on a pseudo 2D model parameterization together with 1D forward data simulation (Auken and Christiansen, 2004, and Socco et al., 2009). The LCI is a deterministic inversion scheme inverting all the dispersion curves simultaneously, minimizing a common objective function: corresponding parameters from neighboring 1D models are linked by means of constraints that act as a regularization of the inversion process. The number of output 1D models is equal to the number of dispersion curves, yielding a 2D pseudosection of

the S-wave velocity in the subsurface. LCI has proven to be a valuable tool able to retrieve 2D effects and to reconcile lateral variability with global homogeneity (Boiero and Socco, 2010). Its application as inversion scheme for our technique is justified, despite the expected lateral variations, by the spatial proximity of the dispersion curves.

Resolution issues

The application of the spatial windowing is not without consequences on the lateral resolution of the retrieved dispersion curves and on the wavenumber resolution of the related *f-k* spectra. We define the lateral resolution of a dispersion curve as the width of the subsoil portion the dispersion curve can be considered representative of. We have conventionally set this width as 2σ, i.e. we assume that every dispersion curve mainly reflects the seismic properties of a subsurface portion centered at the Gaussian window maximum and σ wide on both sides (see Figure 1.3).

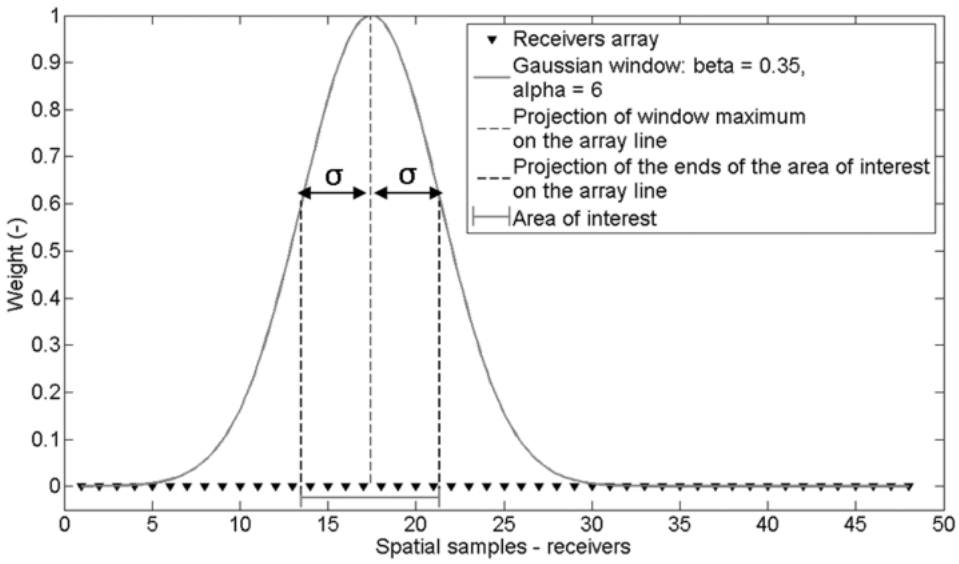

Figure 1.3 – Effect of Gaussian window shape on the lateral resolution of the corresponding dispersion curve. A Gaussian window with $\alpha = 6$ and $\beta = 0.35$ is represented: the thick dashed black lines mark the projection on the array line of the points at window maximum +/- σ which are the ends of the subsurface portion influencing the most the corresponding dispersion curve (in the figure legend, the width of this portion is referred to as "area of interest").

A large value of α produces a small value of σ (because of the relationship between σ and α expressed by equation 2) and improves the lateral resolution: vice versa, a small value of α produces a large value of σ and a poor lateral resolution. Unfortunately,

we cannot set at will the width of the Gaussian windows because the lateral resolution of the dispersion curves clashes with the wavenumber resolution of the *f-k* spectra. In order to define the wavenumber resolution, we have to recall that the SW method implies the analysis of the recorded seismic traces using a wavefield transform (e.g. *f-k* or ω-*p*) to retrieve the dispersion curves. In this paper we use and make reference to the *f-k* transform, but the following considerations, suitably modified, are valid for other wavefield transforms as well. The *f-k* spectrum we can compute from the recorded traces is indeed an estimate of the actual *f-k* spectrum of the vertical vibration velocity of the ground particles at the surface of the investigated site. The estimated spectrum, in fact, depends on the acquisition array geometry and on the used spectral estimator: these two factors are combined in the resolution function or Array Smoothing Function (ASF). Therefore, we have:

$$\hat{P}(f,k) = ASF * P(f,k) \tag{3}$$

where $\hat{P}(f,k)$ is the estimated *f-k* spectrum, $P(f,k)$ is the theoretical spectrum and *ASF* is the array smoothing function (Johnson and Dudgeon, 1993). When we use the Fourier transform, we can write the ASF as:

$$ASF(k) = \sum_{n=1}^{N} w_n \exp(ik \cdot x_n) \tag{4}$$

where w_n is the weight for the n^{th} sensor, which depends on the window coefficients, k is the wavenumber, x_n the position of the n^{th} receiver and N is the total number of receivers. The ASF amplitude represents the leak of energy: the main-lobe width (Figure 1.4) is determined by N, the spacing between neighboring receivers dx and the window coefficients w_n and it quantifies the wavenumber resolution of the estimated *f-k* spectrum.

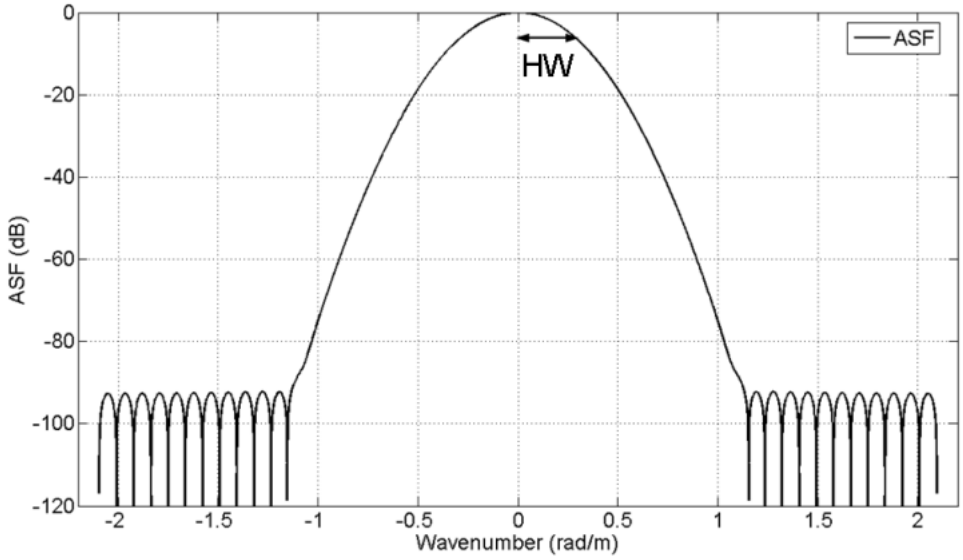

Figure 1.4 – Array Smoothing Function for a 48 receiver array with spacing 1.5 m spatially windowed with a Gaussian window defined by α = 6 and β = 0.5. The wavenumber of the ASF at -6 dB, called half width (HW), defines the array wavenumber resolution.

According to the Rayleigh resolution criterion, the half of the main lobe width at -6 dB (half width or HW in Figure 1.4) quantifies the array wavenumber resolution (Johnson and Dudgeon, 1993). HW defines both the minimum detectable wavenumber and the minimum wavenumber distance between neighboring events on the *f-k* plot (e.g. two different SW propagation modes) so that the two events can be distinguished. The ASF, equation 4, is function of w_n, the window coefficient attributed to the n^{th} trace, hence, the application of a spatial windowing to the seismogram has consequences on the ASF and, therefore, on the wavenumber resolution. In general, the wider the window, the narrower the ASF main lobe and therefore the smaller HW: hence it exists a drawback between lateral and spectral resolution.

Figure 1.5 represents the ASFs for a 48 receiver array with 1.5 m spacing.

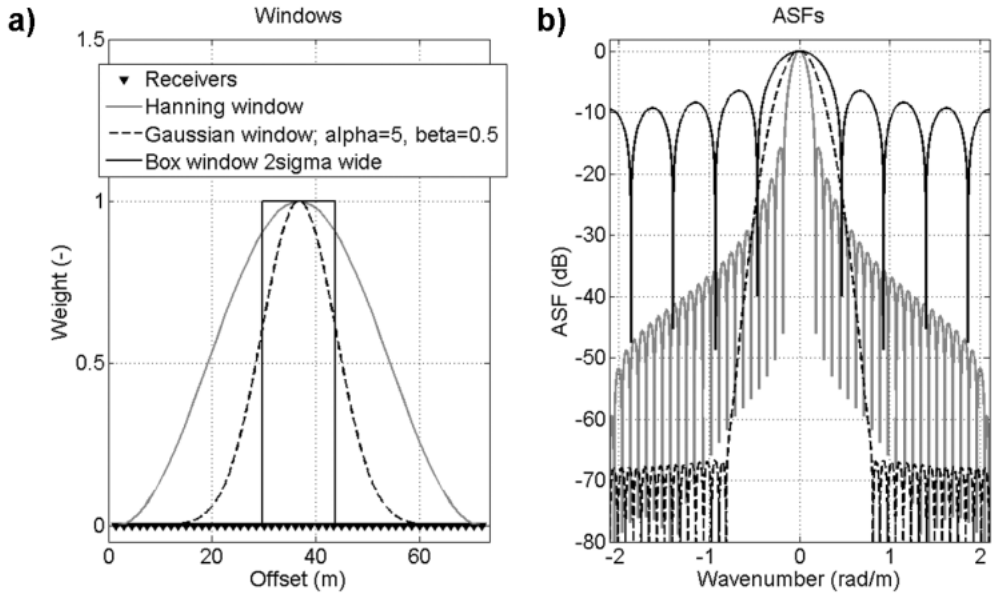

Figure 1.5 – a) 48 receiver array with 1.5 m spacing; traces are spatially windowed with a Hanning window (gray line), a Gaussian window (dashed black line) defined by α = 5 and β = 0.5, and a box window (black continuous line) 2σ wide. b) the ASFs for the three windows, displayed with the same line styles.

We spatially windowed the traces by a box window, a Hanning window and a Gaussian window with α = 5 and β = 0.5 (Figure 1.5a portrays the windows while Figure 1.5b depicts the corresponding ASFs). Several authors have already used the Hanning window for the mitigation of lateral variations effects on SW analysis and to attenuate "ghost" maxima on the *f-k* spectrum (Boiero, 2009), extracting a single dispersion curve from the seismogram: on the contrary, a sliding box window (which equals to dividing the seismogram into sub-seismograms) or the Gaussian windows described in the previous section provide a set of dispersion curves from the same seismogram. Figure 1.5 shows that the Gaussian window is a good compromise between the optimal wavenumber resolution of the Hanning window and the high lateral resolution of the box window: the HW for the Gaussian window is greater than the Hanning window one but smaller than the box. In other words, the use of a spatial windowing based on a set of Gaussian windows defined as proposed allows several local dispersion curves to be extracted from a single seismogram and, at the same time, it ensures a greater wavenumber resolution with respect to subdividing the seismogram into several portions. Care has to be taken when choosing the width of the Gaussian windows, i.e. for the choice of parameter α: the greater is α, the poorer the wavenumber resolution, the better the lateral resolution of the retrieved dispersion curves, and vice versa (Figure

1.6). The optimal α value should then guarantee a sufficient wavenumber resolution (i.e. we must warrant a suitable minimum k and we must be able to detect surface-wave propagation modes as separate events on the *f-k* plot) but it should also ensure dispersion curves as local as possible.

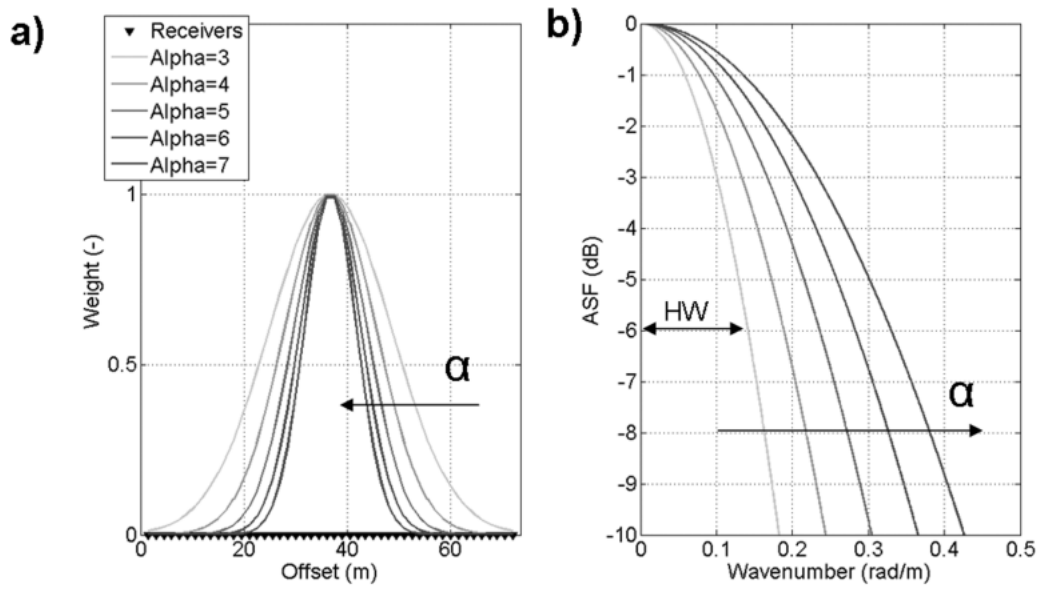

Figure 1.6 – a) 48 receiver array with 1.5 m spacing; traces are spatially windowed with Gaussian windows defined by increasing α values and β = 0.5; b) the ASFs for the windows, displayed with the same colors. Note that the wider the window, the greater HW.

According to the previous definition of lateral resolution (2σ) and spectral resolution (HW), we can compute, for a given receiver spread, the value of lateral and spectral resolution provided by a chosen value of α. The plot in Figure 1.7 represents the relationship among the value of parameter α, the lateral resolution of the respective dispersion curves, and the wavenumber resolution of the *f-k* spectra for several array configurations. If only the fundamental mode is present on the computed *f-k* spectrum, we can improve the lateral resolution as long as we ensure the necessary minimum wavenumber.

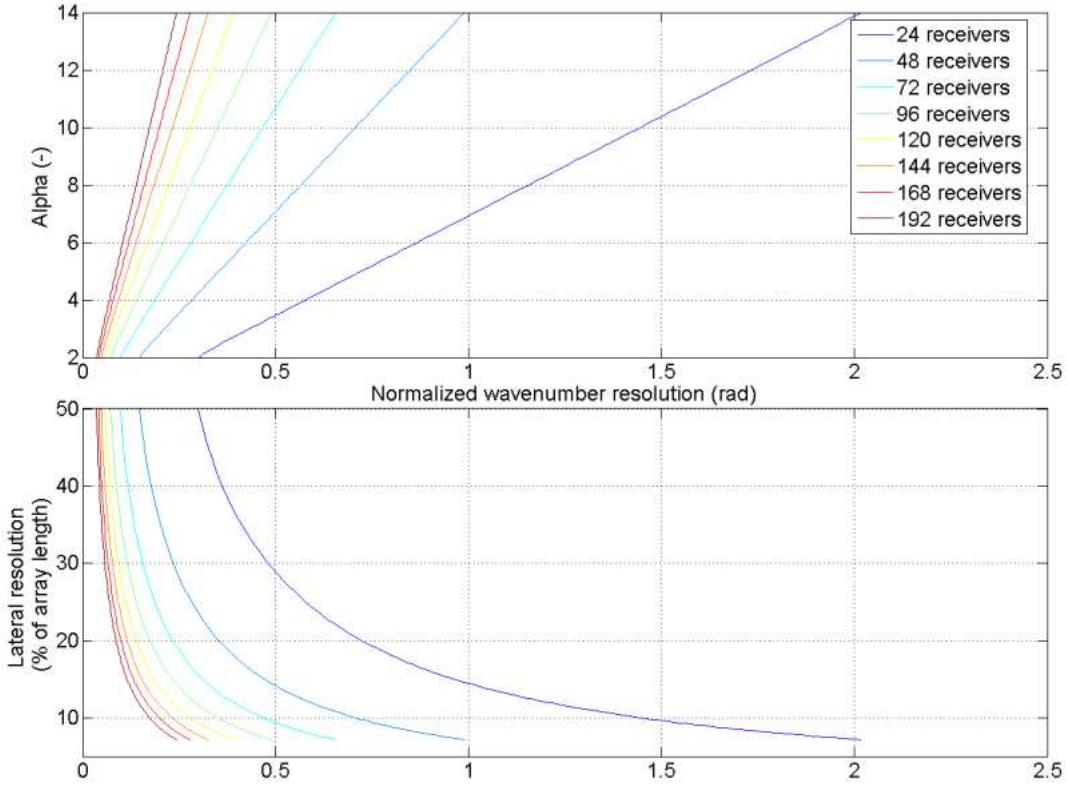

Figure 1.7 – The plot represents the relationship among the value of α, the lateral resolution of the respective dispersion curves and the wavenumber resolution of the f-k spectra for several array configurations. The wavenumber resolution is multiplied by the spacing between receivers, yielding the normalized wavenumber resolution; the lateral resolution is represented in terms of ratio between 2σ and the total array length.

If several dispersive events are displayed on the *f-k* spectrum, we can retrieve the wavenumber resolution that is required to distinguish them from the *f-k* plot obtained from the same seismogram without windowing. By entering the chart in Figure 1.7 with the required wavenumber resolution we can get the value for parameter α and the consequent lateral resolution of the dispersion curves. Once the lateral resolution is known, we can determine the spacing between neighboring dispersion curves (and therefore the appropriate β values): as we set the width of the area of influence of a dispersion curve to 2σ, the spacing between the Gaussian windows maxima should indicatively assume the same value. However, in case of particularly complex expected lateral heterogeneities, a finer dispersion curves extraction can be appropriate.

RESULTS

Synthetic examples

We assessed the feasibility of the proposed method for the processing of SW data on three synthetic data sets characterized by different kinds of lateral variations. The first synthetic model is made of two layers overlying a half-space (Figure 1.8). The thickness of the two layers linearly varies along the survey line, which is made up of 181 receivers with 1 m spacing.

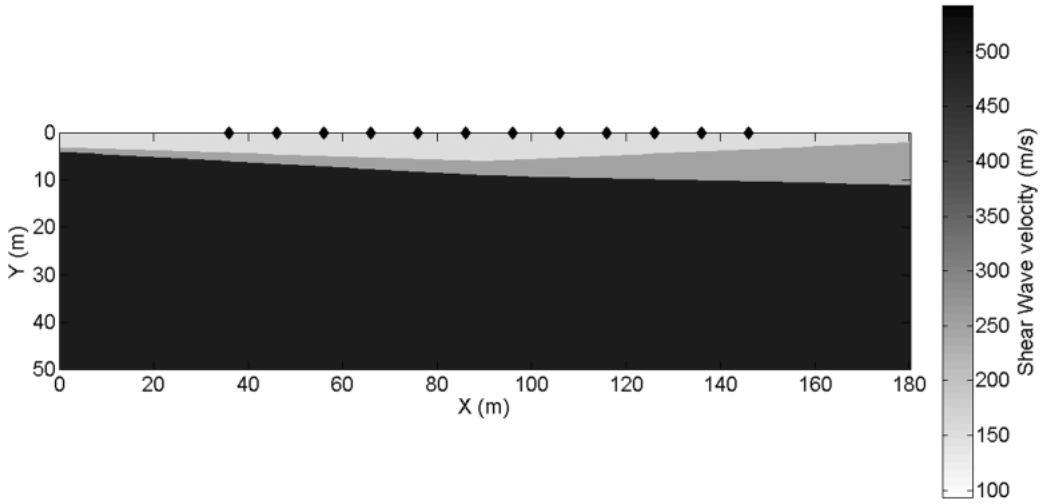

Figure 1.8 – First synthetic model geometry. The upper layer is characterized by a shear wave velocity of 150 m/s, whereas the second layer velocity is 250 m/s. The half-space has a velocity of 500 m/s. The rhombi on the top surface of the model mark the positions of the Gaussian windows maxima and, therefore, the locations of the retrieved dispersion curves.

We modeled the Rayleigh wave fundamental mode propagation by the following equation (Woodhouse, 1974; Boiero, 2009):

$$u(X,\omega) = \sum_{j=0}^{J} R_j(X,\omega) \exp\left\{-i\omega \int_{ray_j} dx\, p_j(x,\omega)\right\} S_j(\omega) \qquad (5)$$

where, $p_j(x,\omega)$ is the slowness distribution along the ray path X for the j^{th} mode while $S_j(\omega)$ represents the excitation imposed by the source, and $R_j(X,\omega)$ includes the terms dependent on receiver depth and the geometrical spreading of the surface waves. We

simulated two shots in (0,0) and (180,0), respectively. We applied the processing scheme based on Gaussian windows to the synthetic data to extract a set of 12 dispersion curves, evenly-spaced along the line. We set parameter α to 5: as we simulated only the fundamental mode propagation, no other dispersive events are present on the *f-k* plot and therefore the choice of the optimal α is driven only by the minimum *k* that we have to guarantee. The minimum wavenumber (k_{min}), in fact, is related to the maximum recordable wavelength (λ_{max}), as $k_{\min} = 2\pi/\lambda_{\max}$, and λ_{max} itself is linked to the investigation depth (z_{max})., being roughly between two and three times z_{max}. To guarantee an investigation depth able to ensure a good characterization of all the three layers ($z_{max} \approx 30$ m), we estimate a required minimum wavenumber equal to $k_{\min} = 2\pi/\lambda_{\max} = 2\pi/2.5z_{\max} = 8.4\ 10^{-2}$ rad/m. Hence, as presented in Figure 1.9, the appropriate α value is around 5: the guaranteed lateral resolution is 35 m, but we opted for a denser dispersion curve extraction (a curve every 10 m) to carefully follow the expected lateral variation.

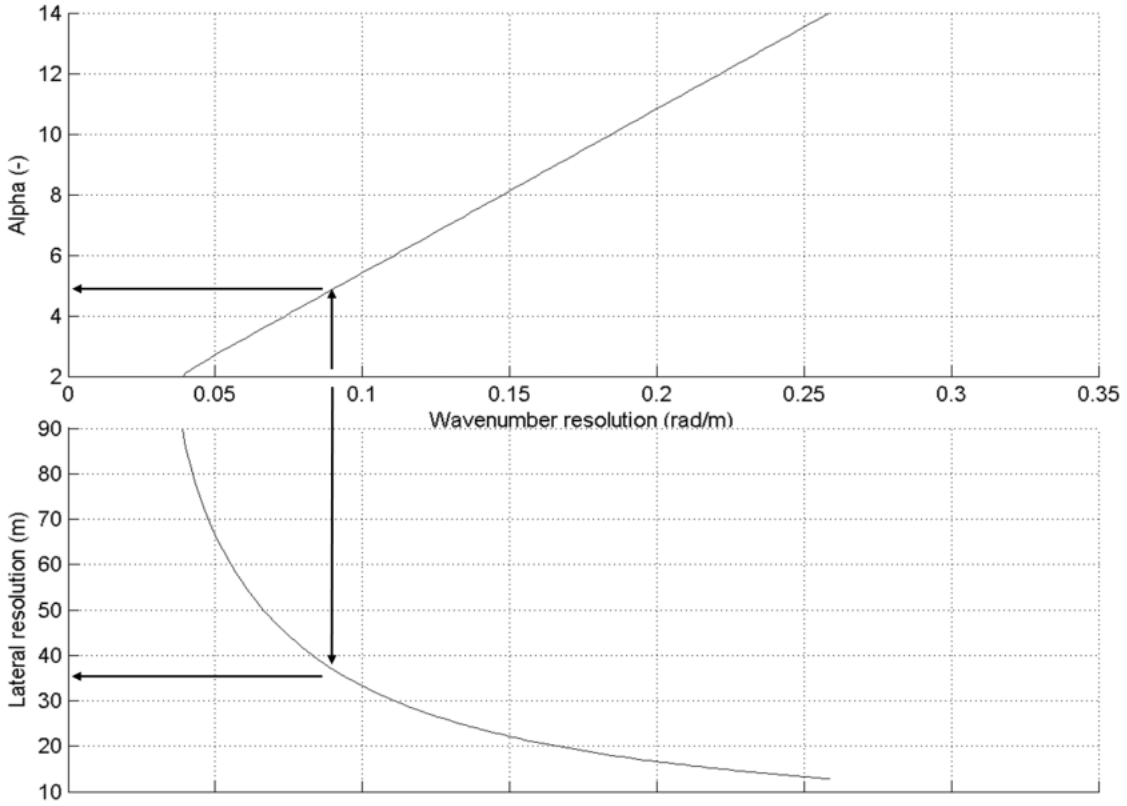

Figure 1.9 – Chart from Figure 1.7 accustomed for the first synthetic model (Figure 1.8) array configuration. By entering the plot with the required k resolution, we obtain an α value of 5 and a lateral resolution of 35 m.

As two shots were available, we stacked the *f-k* spectra from the two shots with the same spatial windowing, and we performed the picking of maxima on each stacked *f-k* spectrum.

Figure 1.10 represents the obtained dispersion curves both in terms of frequency versus phase velocity and pseudo-depth (wavelength/2.5) versus apparent S-wave velocity (1.1 times phase velocity): the latter representation is referred to as "approximate inversion" in engineering geophysics (O'Neill, 2004) and it is a rough indication of the lateral and vertical variation of shear wave velocity (V_s).

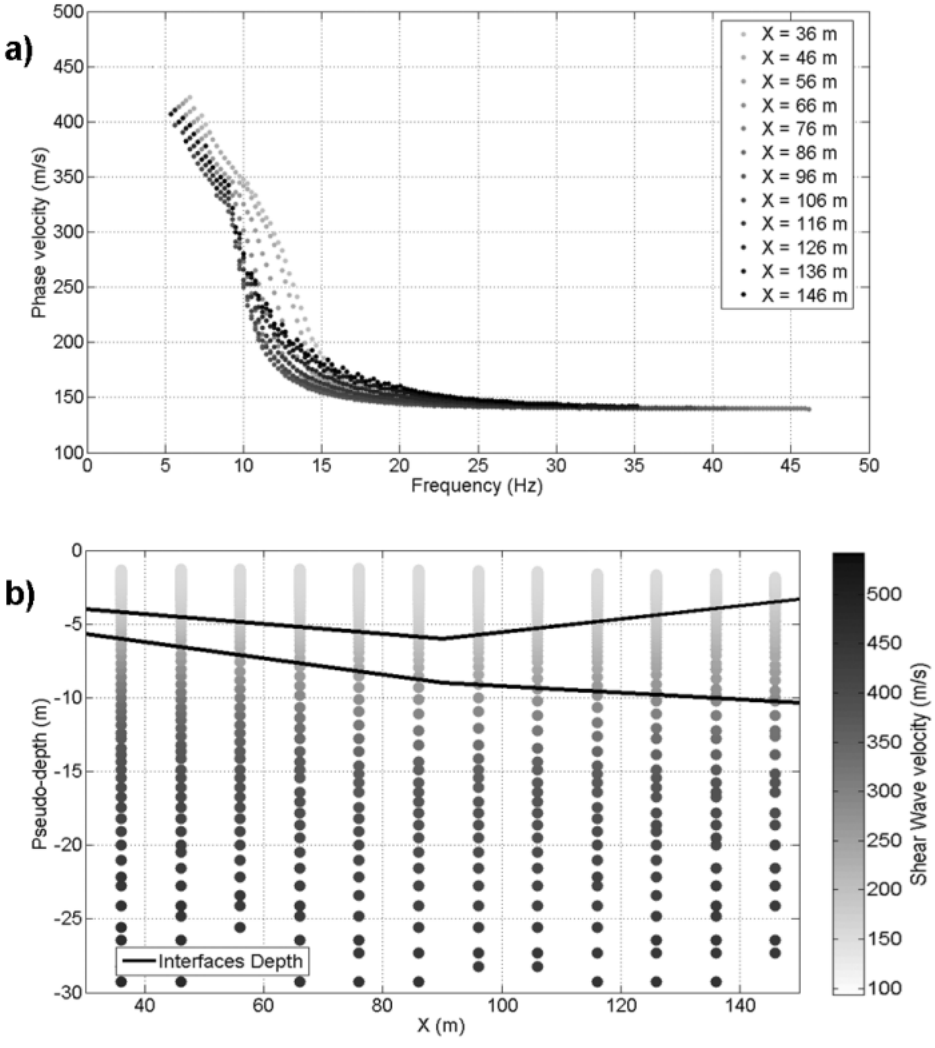

Figure 1.10 – Dispersion curves from the synthetic model in Figure 1.8. a) Dispersion curves represented in terms of phase velocity versus frequency: the dispersion curves color depends on the reference point position. b) Dispersion curves represented in terms of pseudo-depth (wavelength/2.5) versus apparent S-wave velocity (1.1 times phase velocity).

In Figure 1.10b the trend of the two interfaces is quite well marked by velocity discontinuities in the dispersion curves. We eventually inverted the dispersion curves using an LCI approach setting medium constraints among velocities and loose constraints among thicknesses. Figure 1.11 shows the inversion results, with the actual position of the interfaces depicted in black: we managed to retrieve the 2D structure of the model and the obtained velocity values have a maximum estimation relative error of 9%.

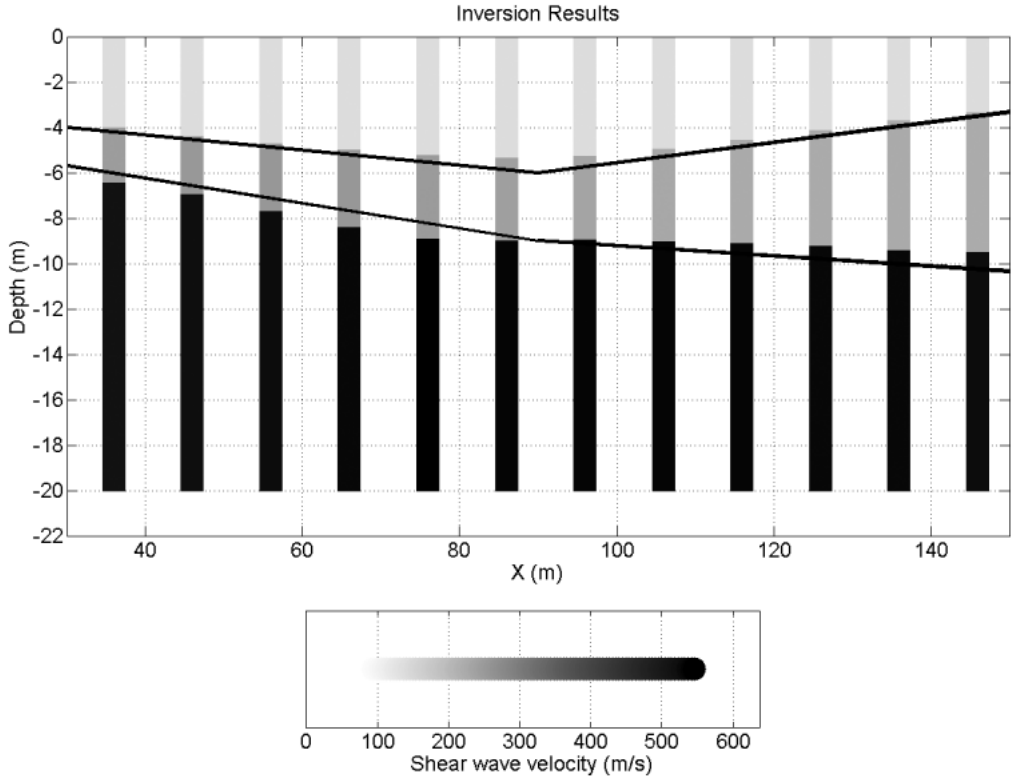

Figure 1.11 – Inversion results of the dispersion curves from the synthetic model of Figure 1.8. The black lines mark the actual positions of the interfaces.

We produced the second and the third synthetic data sets by using an available finite-element method (FEM) code for numerical simulations (COMSOL Multiphysics ®). The second synthetic model is a 2D linear, elastic isotropic model. Its geometry and V_s are represented in Figure 1.12: the model is made up of two layers and a half-space, but the second layer contains a lens whose mechanical properties are the same as the half-space. The model geometry is therefore not trivial, with abrupt lateral variations hard to be retrieved. We used a Ricker source centered at 10 Hz for the shots simulation: again, we simulated two shots, with the source position in (310,0) and

(490,0) respectively. We recorded the vertical vibration velocity at the surface in 181 positions between the two sources locations with 1 m spacing.

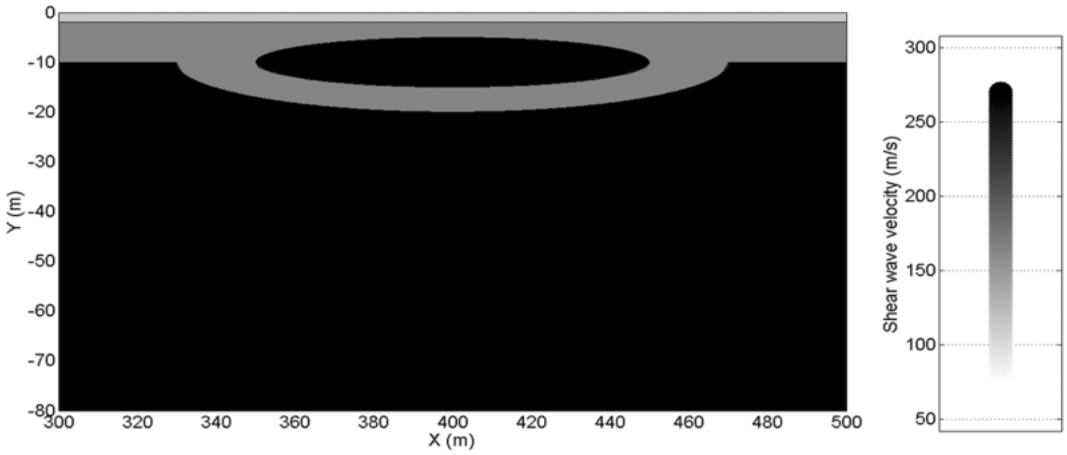

Figure 1.12 – Second synthetic model geometry. For graphical clarity reasons, in the current figure only the central portion of the model is displayed: the synthetic model extends from X = 0 to X = 800 m and from Y = 0 down to -220 m without any other vertical or lateral variations. The model is a 2D model carried out by using COMSOL Multiphysics ®. The upper layer S-wave velocity is 120 m/s, the second layer velocity is 170 m/s and the half-space V_s is 270 m/s. The lens has the same velocity as the half-space.

Table 1.1 displays other numerical simulation details.

Table 1.1 – Finite-element method simulation parameters for the second synthetic model.

Total number of FEM elements	142047 mesh elements
Degrees of freedom	5720004
Time step	10^{-3} s
Maximum simulation time	3.5 s

Again, we applied the processing scheme based on Gaussian windows to the synthetic data. First, we computed the *f-k* spectrum of the first simulated seismogram without any windowing to estimate the necessary wavenumber resolution. As

highlighted in Figure 1.13, the minimum k we need to compute and the distance between dispersive events (fundamental and first higher mode) is around 0.11 rad/m, so that the appropriate value for α is 6 (Figure 1.14).

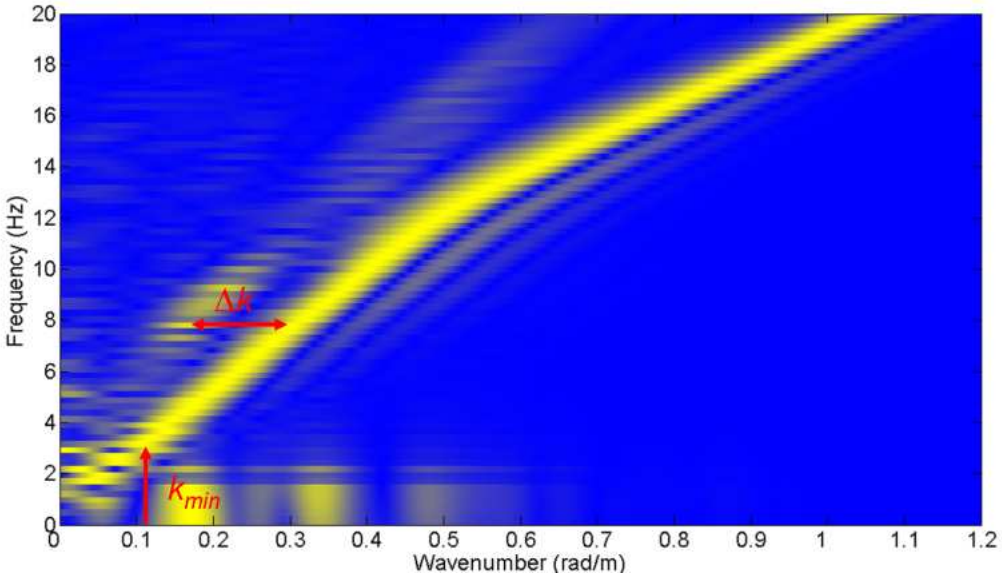

Figure 1.13 – Zoom of the f-k spectrum of the simulated shot in (310, 0) without spatial windowing. Red arrows mark the minimum k (k_{min}) that we need to compute and the wavenumber distance between two dispersive events that we have to guarantee (Δk).

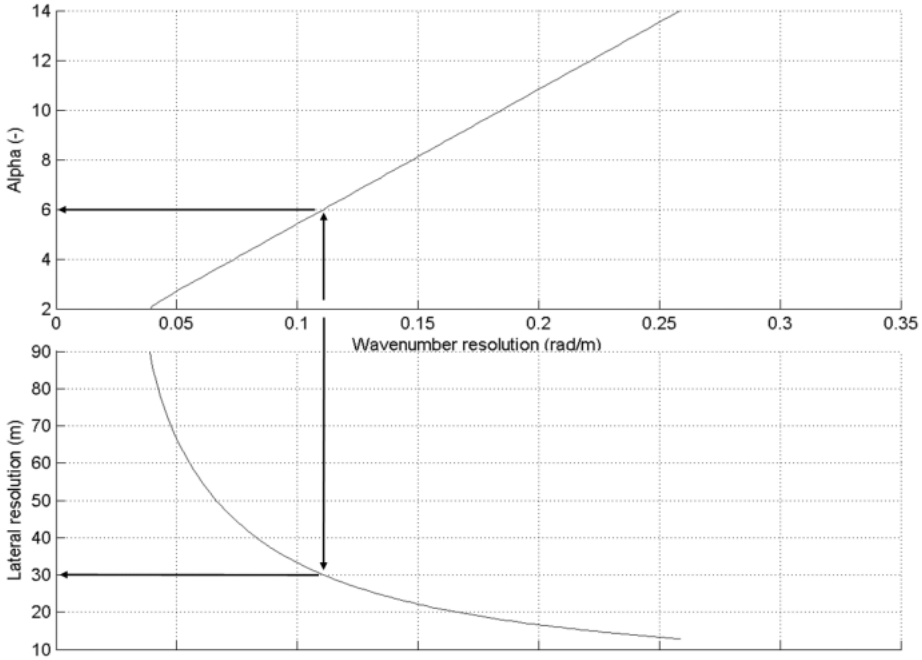

Figure 1.14 – Chart from Figure 1.7 accustomed for the second synthetic model (Figure 1.12) recording array configuration. By entering the plot with the required k resolution, we obtain an α value of 6 and a lateral resolution of 30 m.

The guaranteed lateral resolution is 30 m, but we extracted a dispersion curve every 5 m being the 2D structure of the model particularly challenging. We obtained 25 dispersion curves, evenly spaced along the survey line: these dispersion curves are depicted in Figure 1.15 in pseudo-depth (wavelength/2.5) versus apparent S-wave velocity (1.1 times phase velocity) and in frequency versus phase velocity.

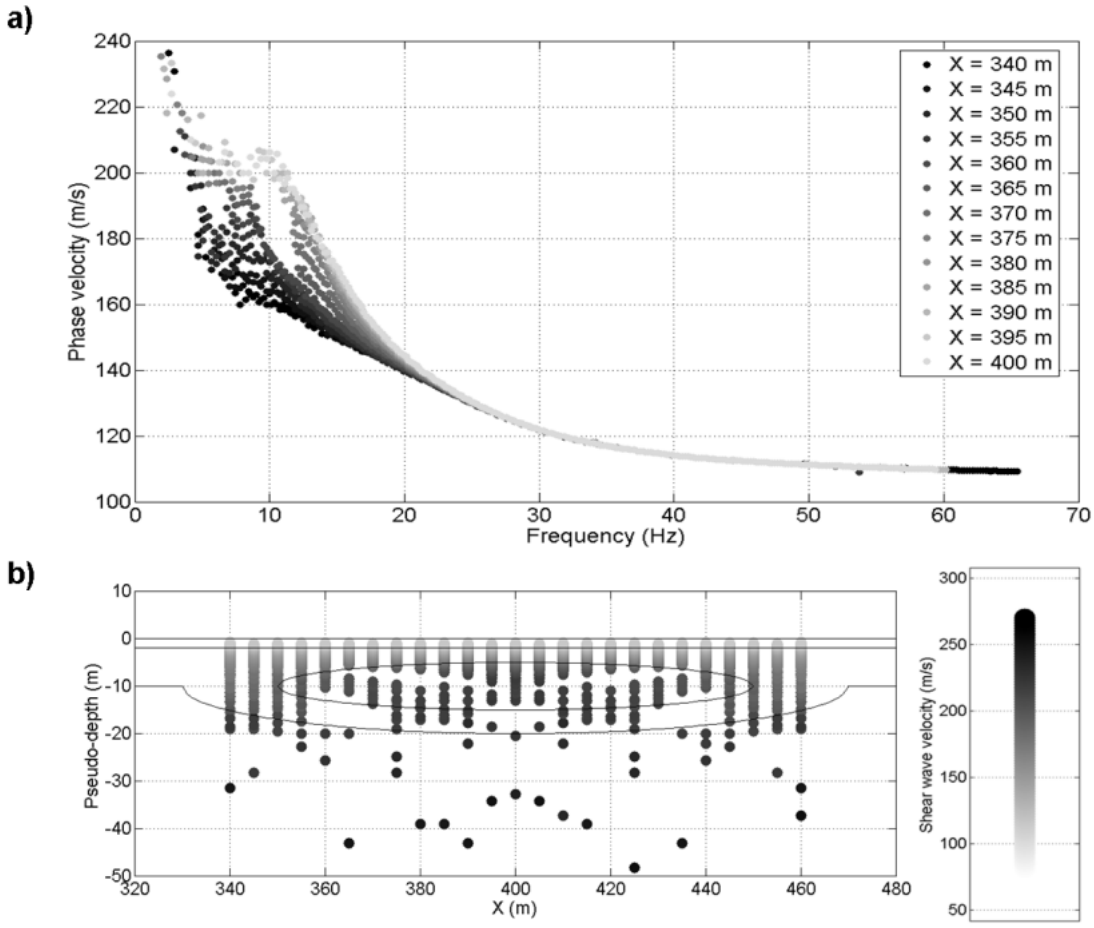

Figure 1.15 – Dispersion curves from the synthetic model in Figure 1.12. a) Dispersion curves relevant to the left hand side of the model (as the model is symmetric dispersion curves are symmetric as well) represented in terms of phase velocity versus frequency: the dispersion curves color depends on the reference point position. b) Dispersion curves represented in terms of pseudo-depth (wavelength/2.5) versus apparent S-wave velocity (1.1 times phase velocity).

In Figure 1.15a the dispersion curves interested by the presence of the lens are characterized by increasingly higher velocities in the 5-20 Hz frequency band as the lens thickness increases; in Figure 1.15b the same curves are characterized by higher velocities at pseudo-depths approximately equal to the lens position: such higher

velocities affect a wider range of pseudo-depths as the lens thickness increases. As for the LCI, we applied weak constraints for all thicknesses and velocities but for the half-space velocity, for which we imposed a medium constraint. In Figure 1.16 we show the LCI results: we managed to correctly retrieve the interface between first and second layer and the upper edge of the lens and even to satisfactorily reconstruct the overall trends of the lower edge of the lens and of the deepest interface.

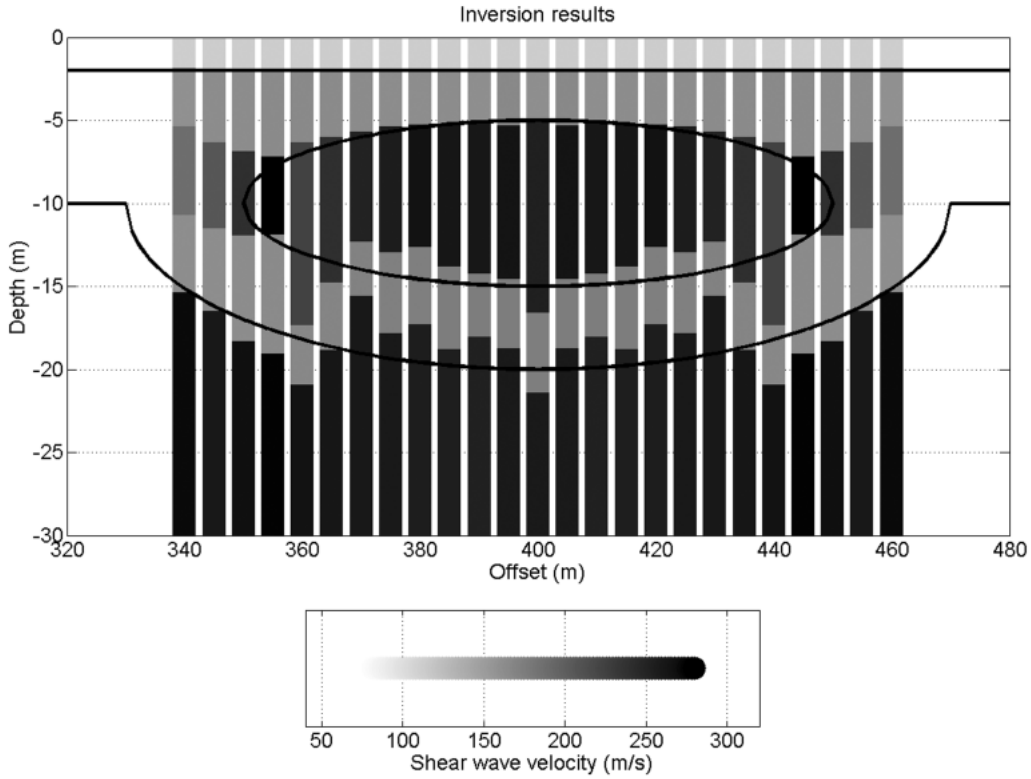

Figure 1.16 – Laterally constrained inversion results for the second synthetic model (Figure 1.12).

As far as the velocities are concerned, their estimation relative errors are below 15% with the exception of the V_s of the layers at the two edges of the lens: in this case, the smoothing effect induced by the lateral resolution of the Gaussian windows, whose width is controlled by the minimum necessary wavenumber resolution, does not allow the inversion to completely follow this abrupt lateral variation.

We produced the third synthetic data set by using COMSOL Multiphysics ® again. The synthetic model is a 2D linear, elastic isotropic model. Its geometry and V_s characteristics are displayed in Figure 1.17: an upper 2 m thick layer tops a second layer whose thickness abruptly decreases from 8 to 2 m at the centre of the model.

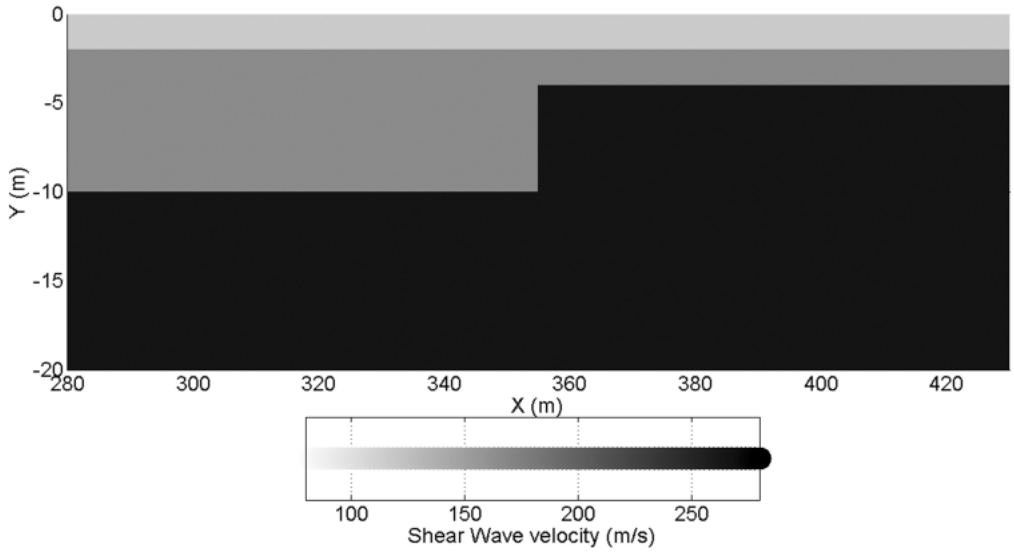

Figure 1.17 – Third synthetic model geometry. For graphical clarity reasons, only the central portion of the model is displayed: the synthetic model extends from X = 0 to X = 710 m and from Y = 0 down to -200 m without any other vertical or lateral variations. The model is a 2D model carried out by using COMSOL Multiphysics ®. The upper layer S-wave velocity is 120 m/s, the second layer velocity is 170 m/s and the half-space V_s is 270 m/s.

We created this model because we wanted to test our technique on such a strong and sharp lateral variation: besides, a similar model had already been used by Nagai et al. (2005) to test another lateral shear wave velocity imaging technique based on 1D SW inversion. We simulated two shots, with the source position in (280,0) and (430,0): our source signal was again a Ricker source centered at 10 Hz. For both shots, we recorded the vertical vibration velocity by means of 301 synthetic receivers located on the top surface of the model between the sources positions with 0.5 m spacing. The number of FEM elements, sampling rate and recording time are reported in Table 1.2.

Table 1.2 – Finite element method simulation parameters for the third synthetic model.

Total number of FEM elements	167500 mesh elements
Degrees of freedom	677300
Time step	$1.25\ 10^{-3}$ s
Maximum simulation time	3 s

Once again, we applied the processing scheme based on Gaussian windows to the synthetic data. As far as the choice of the optimal α is concerned, we computed the *f-k* spectrum of the simulated seismogram whose source is located at (430,0) without any windowing applied (Figure 1.18).

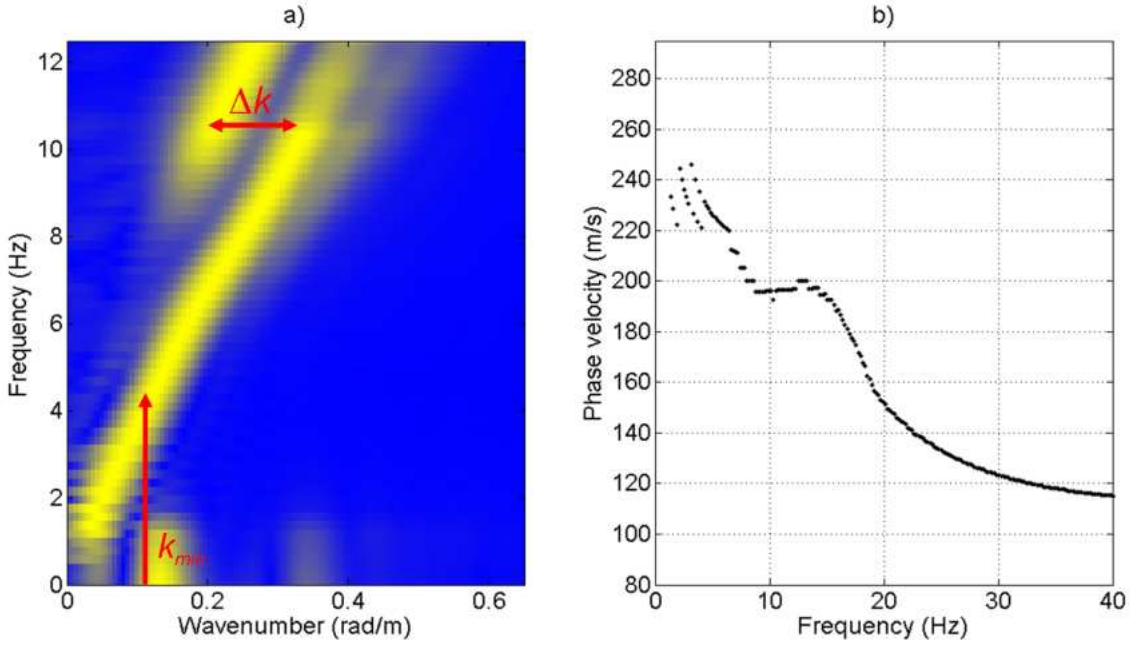

Figure 1.18 – a) Zoom of the f-k spectrum of the simulated shot with source in (430,0) without spatial windowing. Red arrows indicate the minimum k (k_{min}) we need to compute and the wavenumber distance between two dispersive events that we have to guarantee (Δk). b) Corresponding dispersion curve: the unreliability of the curve below 4.5 Hz justifies the choice of the minimum wavenumber k_{min}.

The minimum distance between dispersive events on the *f-k* plot that we must preserve is around 0.13 rad/m but the minimum *k* is around 0.04 rad/m: however, due to the frequency resolution, the dispersion curve is not reliable below 4.5 Hz (Figure 1.18b) which approximately corresponds to 0.13 rad/m on the *f-k* plot. Therefore, by entering this wavenumber resolution value in the chart (Figure 1.19), we set α to 6. The ensured lateral resolution is hence 25 m, but we opted for a finer dispersion curves extraction (one curve every 5 m, for a total number of 21 dispersion curves). The retrieved dispersion curves are represented in Figure 1.20 both in terms of pseudo-depth (wavelength/2.5) versus apparent S-wave velocity (1.1 times phase velocity) and in frequency versus phase velocity plot. Both plots in Figure 1.20 show the effectiveness

of the dispersion curves to describe the model beneath the Gaussian windows maxima and thus to reconstruct lateral variations.

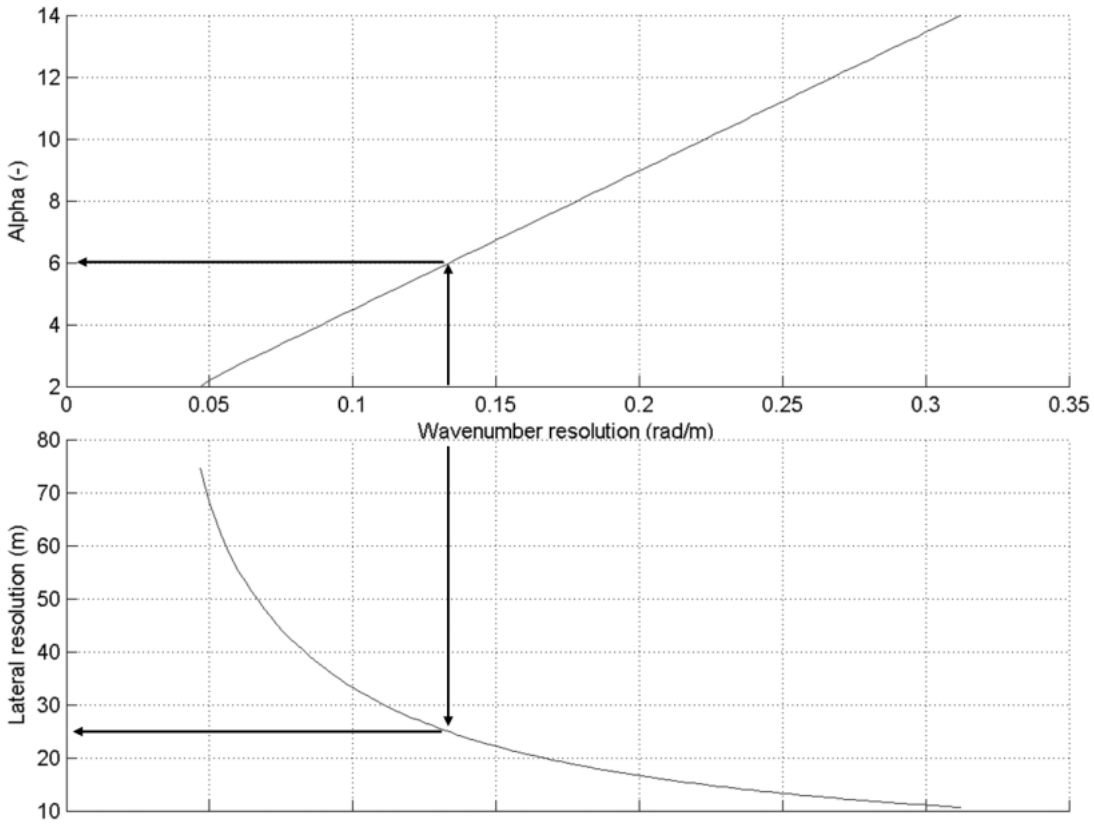

Figure 1.19 – Chart from Figure 1.7 accustomed for the third synthetic model recording array configuration. By entering the plot with the required k resolution, we obtain an α value of 6 and a lateral resolution of 25 m.

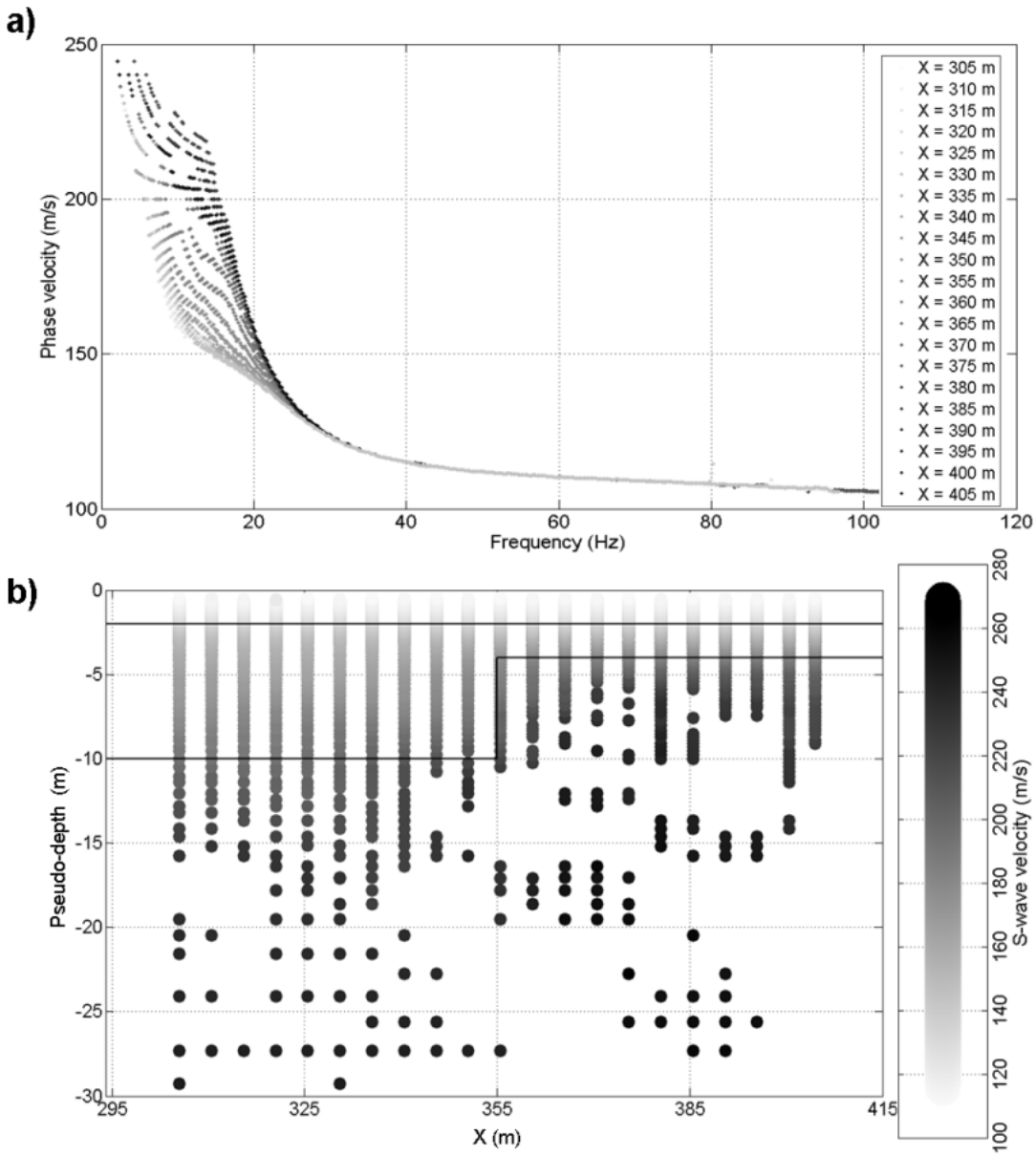

Figure 1.20 – Dispersion curves from the synthetic model in Figure 1.17. a) Dispersion curves represented in terms of phase velocity versus frequency: the dispersion curves color depends on the reference point position. b) Dispersion curves represented in terms of pseudo-depth (wavelength/2.5) versus apparent S-wave velocity (1.1 times phase velocity).

However, especially when looking at Figure 1.20a it appears clearly that the dispersion curves closer to the model discontinuity are influenced by both the subsurface portions left and right of the fault making the lateral variation to look smoother than it actually is. This is due to the width of the Gaussian windows bells: a greater value for α could attenuate such smoothing effect but the choice of the α value

was driven by wavenumber resolution requirements. As already stated in the "Method" section we need to find a balance between lateral and wavenumber resolutions.

We inverted the dispersion curves using the laterally constrained approach and imposing a medium constraints between the shear wave velocities of corresponding neighboring layers and no constraints on layer thicknesses. Figure 1.21 depicts the inversion results: we satisfactorily reconstructed both the interfaces depths and the V_s but the smoothing effect already noticed in the dispersion curves has obviously the same consequences on the inversion results. We could reconstruct the sharpness of the lateral discontinuity by suitably tuning the constraints (i.e. by "breaking" the constraints on the discontinuity) but this would require an a priori knowledge of the position of the lateral variation itself.

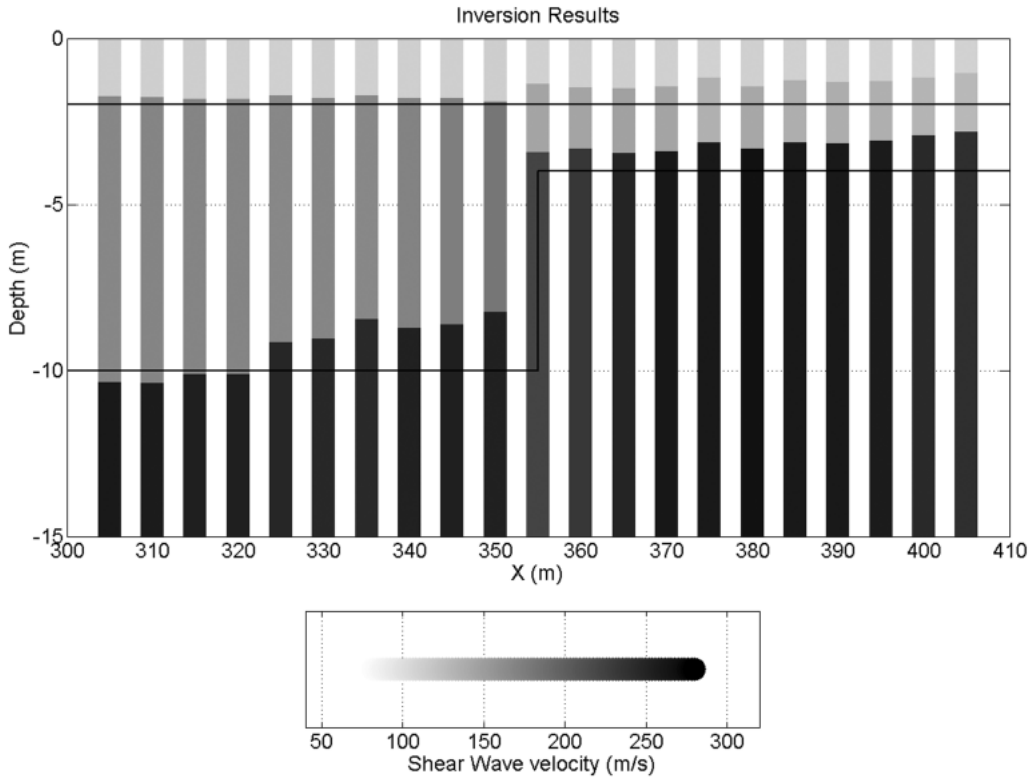

Figure 1.21 – Laterally constrained inversion results for the third synthetic model (Figure 1.17).

Field example

The real data set on which we tested the procedure was acquired in Tarcento, north-west Italy, during a seismic risk assessment campaign (Piatti et al., 2009). The recording

array was made up of 48 vertical 4.5 Hz geophones with 1.5 m spacing. The acquisition consisted in 20 shots performed with a hammer source, 10 of them with the source located 1.5 m before the first receiver and the other ones with the source located 1.5 m past the last receiver. The acquisition parameters in time domain are 2 s acquisition length and 0.5 ms sampling rate. We windowed all seismograms in the spatial domain using a set of Gaussian windows. For the estimation of the optimal α value we computed the *f-k* spectra of some shots without applying any windowing: we determined the required wavenumber resolution by inspecting these *f-k* plots. In Figure 1.22 the spectrum from a shot whose source is located 1.5 m before the first receiver is depicted: at low frequencies (<12 Hz) the spectrum is quite noisy, so that the minimum useful *k* is approximately 0.23 rad/m and the distance between neighboring dispersive events is greater than this value.

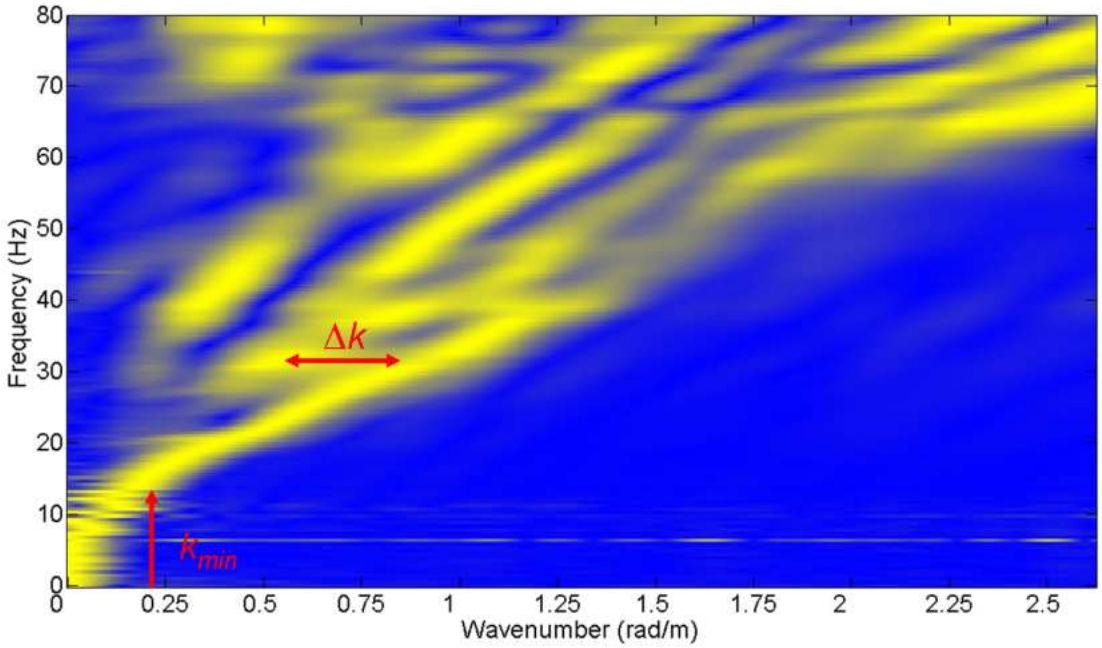

Figure 1.22 – Zoom of the f-k spectrum of one of the shots from the real data set without any spatial windowing. Red arrows mark the minimum k (k_{min}) we need to compute and the wavenumber distance between two dispersive events that we have to guarantee (Δk).

By entering 0.23 rad/m into the chart (Figure 1.23), the resulting α is 4.75: the consequent ensured lateral resolution is 15 m but once again we decided to get a finer coverage of the expected lateral variations in the subsoil (we extracted a dispersion curve every 4.5 m).

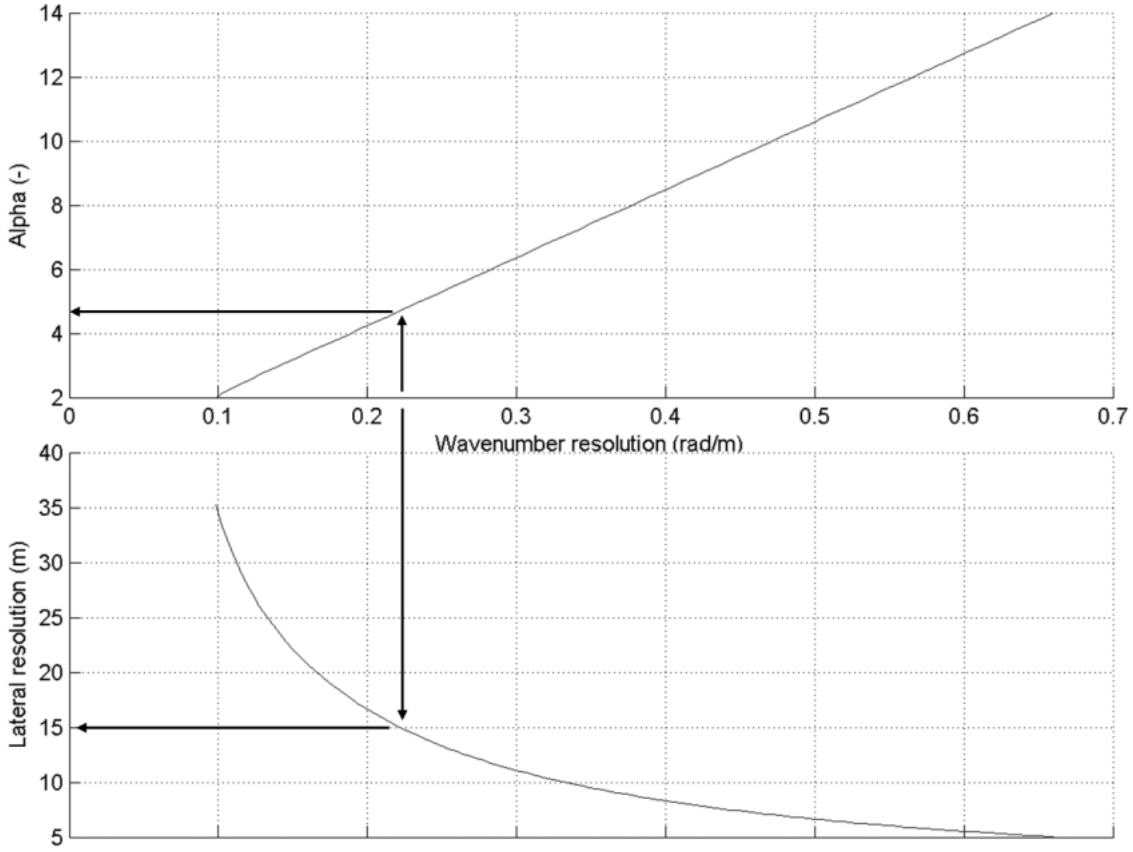

Figure 1.23 - Chart from Figure 1.7 accustomed for the real case array configuration. By entering the plot with the required k resolution, we obtain an α value of 4.75 and a lateral resolution of 15 m.

We stacked the *f-k* spectra from different shots with the same spatial windowing, and we performed the picking of maxima on each stacked *f-k* spectrum, obtaining a set of 10 dispersion curves evenly-spaced along the survey line (Figure 1.24). As for the lateral constrained inversion, according to the a priori geological information available for the site, we imposed weak constraints for the layers thicknesses and we chose moderate constraints for their V_s. Inversion results are displayed in Figure 1.25 together with the P-wave tomography results for the same site: both of them point out a shallower interface at 2-4 m depth gently sloping to the left and a deeper interface at 8-12 m depth leaning to the right.

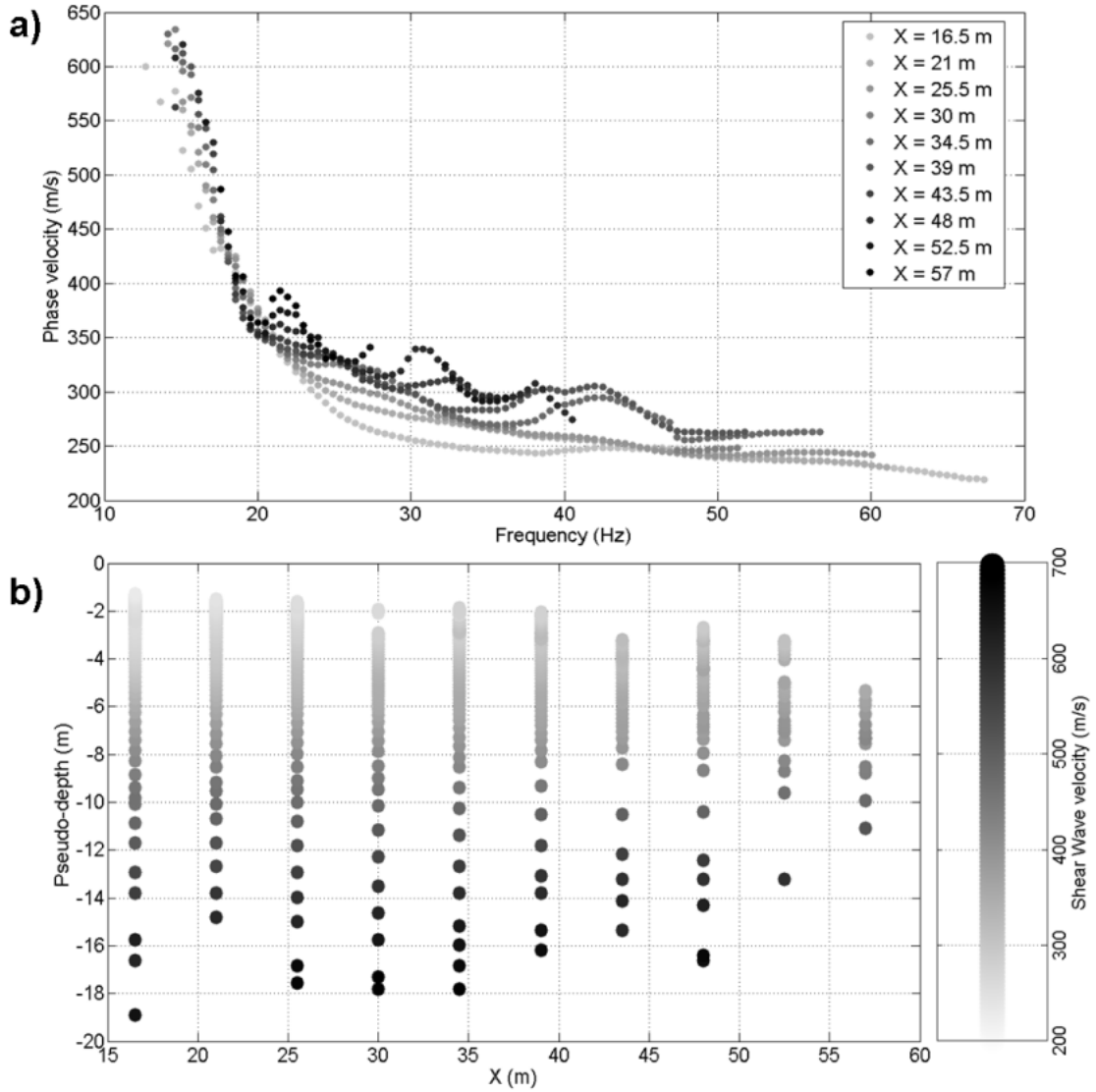

Figure 1.24 – Real data set dispersion curves. a) Dispersion curves are represented in terms of frequency versus phase velocity, and the color depends on the position of the Gaussian windows maxima. b) The same dispersion curves represented in terms of pseudo-depth (wavelength/2.5) versus apparent S-wave velocity (1.1 times phase velocity).

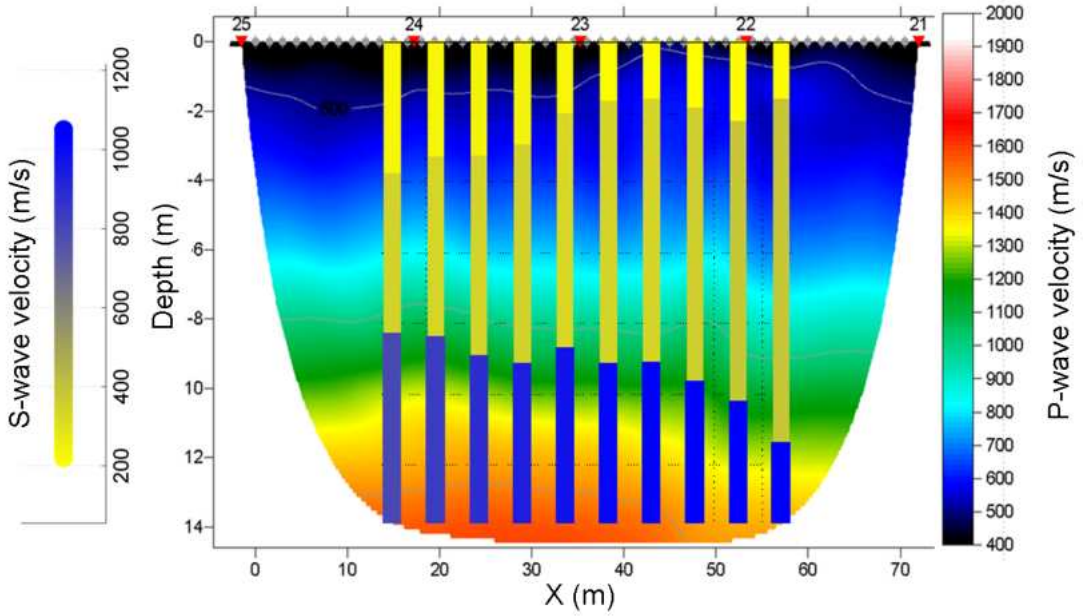

Figure 1.25 – Real data SW inversion results (vertical bars) and P-waves tomography results (background).

DISCUSSION

Both synthetic and real data sets presented in the previous section show the application of the proposed procedure in different conditions with quite satisfactory results: by suitably windowing the record of a single receiver spread it is possible to reconstruct a 2D pseudosection of the subsurface even in case of abrupt lateral variations. However, the key point that clearly emerges from the examples is the balance that we need to find between the lateral resolution of the dispersion curves and the wavenumber resolution of the related *f-k* spectra. Indeed, the more local the dispersion curves (i.e. the greater their lateral resolution), the more accurately we can reconstruct lateral variations, especially in case of strong and/or sudden lateral discontinuities (see for example the lens ends of the second synthetic model in Figure 1.12 or the "fault" of the last synthetic model in Figure 1.17). However, we cannot narrow at will the Gaussian windows for the spatial windowing: the wavenumber resolution of the *f-k* spectra gets poorer so that the minimum *k* of the spectrum increases and we cannot distinguish the surface wave dispersion modes anymore and therefore we obtain an apparent dispersion curve (Socco and Strobbia, 2004). As a consequence, we can improve the lateral resolution of the dispersion curves provided that we guarantee a

sufficient wavenumber resolution. To meet the necessity to balance lateral and spectral resolution we provide a chart (Figure 1.7) representing the relationship among parameter α (and therefore the Gaussian windows width) with the consequent value of area of influence of the extracted dispersion curves and of the ensured wavenumber resolution. By using the chart it is possible to handle such balance, so that i) the problem can be addressed from different points of views (e.g. retrieving lateral resolution from the necessary *k* resolution and vice versa) and ii) it is possible to know what information gets lost in case one of the two resolutions is favored. We applied the chart in all presented cases to get the optimal spatial windowing, to ensure the best possible lateral resolution without renouncing to the minimum necessary spectral resolution. The obtained results are good, we managed to correctly retrieve 2D structures: however, some smoothing of sudden lateral variations has to be accounted for (see how the "fault" in Figure 1.21 or the lens ends in Figure 1.16 are reconstructed) because we cannot narrow Gaussian windows beyond a certain threshold without the loss of some information or accuracy. Eventually, both in real and synthetic cases we applied a very fine dispersion curves extraction, which is appropriate to thoroughly follow 2D effects in the subsurface.

CONCLUSION

We propose a processing technique to retrieve 2D structures from SW acquired with a limited number of receivers: the goal is to get a set of local dispersion curves out of a single seismogram. Our technique is based on a two step process: firstly, we extract a set of local dispersion curves along the receiver spread using a spatial windowing based on Gaussian windows with different maximum position; secondly, we invert the retrieved dispersion curves using a laterally constrained inversion (LCI) scheme yielding a 2D pseudosection of the S-wave velocity. We studied the consequences of the spatial windowing both on the lateral resolution of the dispersion curves and on the wavenumber resolution of the relevant *f-k* spectra: we pointed out the clash between the two resolutions (the more one is fostered, the more the other worsens and vice versa) and the necessity to find a compromise to ensure a correct and accurate description of the subsoil lateral variations. We therefore provided a chart quantitatively representing the relationship existing among the Gaussian windows width, the lateral resolution and the wavenumber resolution they ensure. We tested our technique on four data sets, three synthetic and one real: as far as the synthetic data sets are concerned, the relevant

models are characterized by increasingly complex lateral heterogeneities. We managed to successfully retrieve such 2D structures at the end of the laterally constrained inversion, the last step of our procedure: however, when lateral variations were particularly sharp, they tended to look smoother in the final V_s pseudosection. This was due to the necessity to guarantee a minimum wavenumber resolution, which imposed the choice of Gaussian windows slightly wider than what was necessary to correctly follow such abrupt lateral variations. Once we proved the reliability of our technique on synthetic data, we applied it to a real case: its inversion results are in good agreement with the results of the P-wave tomography performed on the same site, which suggests that we correctly and successfully applied our procedure.

A further development of the present work would be to set up a procedure to properly tune the constraints for the LCI to attenuate what is the main drawback of the proposed procedure, i.e. the "smoothing" effect that is caused by the insufficient lateral resolution ensured by the Gaussian windows. In fact, LCI constraints should be "broken" or weakened by the lateral discontinuity and strengthened where we expect a lesser variability by exploiting, for instance, available a priori information or SW analysis approaches which do not require a dispersion curve extraction.

REFERENCES

Auken, E. and A.V. Christiansen, 2004, Layered and laterally constrained 2D inversion of resistivity data: Geophysics, **69**, 752-761.

Bergamo, P., D. Boiero and L.V. Socco, 2010, Retrieving 2D structures form surface wave data by means of a space varying spatial windowing: 16th EAGE Near Surface meeting, Expanded Abstracts, A33.

Bohlen, T., S. Kugler, G. Klein and F. Theilen, 2004, 1.5D inversion of lateral variation of Scholte wave dispersion: Geophysics, **69**, 330-344.

Boiero, D., 2009, Surface wave analysis for building shear wave velocity models: PhD thesis, Politecnico di Torino.

Boiero, D. and L.V. Socco, 2010, Retrieving lateral variations from surface wave dispersion curves: Geophysical Prospecting, **58**, 977-996.

Boiero, D., L.V. Socco, 2011, The meaning of surface wave dispersion curves in weakly laterally varying structures: Near Surface Geophysics, **9**, 561-570.

Grandjean, G. and A. Bitri, 2006, 2M-SASW: multifold multichannel seismic inversion of local dispersion of Rayleigh waves in laterally heterogeneous subsurfaces: application to the Super-Sauze earthflow, France: Near Surface Geophysics, **4**, 367-375.

Johnson, D. H. and D. E. Dudgeon, 1993, Array Signal Processing: PTR Prentice Hall.

Lin, C. and C. Lin, 2007, Effect of lateral heterogeneity on surface wave testing: numerical simulations and a countermeasure: Soil Dynamics and Earthquake Engineering, **27**, 541-552.

Nagai, K., A. O'Neill, Y. Sanada and Y. Ahida, 2005, Genetic algorithm inversion of Rayleigh wave dispersion from CMPCC gathers over a shallow fault model: Journal of Environmental and Engineering Geophysics, **10**, 275-286.

Nasseri-Moghaddam, A., G. Cascante and J. Hutchinson, 2005, A new quantitative procedure to determine the location and embedment depth of a void using surface waves: Journal of Environmental and Engineering Geophysics, **10**, 51-64.

Neducza, B., 2007, Stacking of surface waves: Geophysics, **72**, no. 2, V51-V58.

O'Neill, A., 2004, Shear velocity model appraisal in shallow surface wave inversion, *in* Viana da Fonseca, A. and P.W Mayne, eds., Geotechnical and Geophysical site characterization: Millpress, 539-546.

Piatti, C., D. Boiero, S. Foti and L.V. Socco, 2009, Integrazione di dati sismici, geologici e geognostici per la costruzione del modello di velocità delle onde di taglio della conca di Tarcento (Friuli). 28th GNGTS, Proceedings of 28th GNGTS, 709-710.

Socco, L.V., D. Boiero, S. Foti and R. Wisén, 2009, Laterally constrained inversion of ground roll from seismic reflection records: Geophysics, **74**, no. 6, G35-G45.

Socco, L.V., S. Foti and D. Boiero, 2010, Surface-wave analysis for building near surface velocity models – Established approaches and new perspectives: Geophysics, **75**, no. 5, 75A83-75A102.

Socco, L.V. and C. Strobbia, 2004, Surface-wave method for near-surface characterization: a tutorial: Near Surface Geophysics, **2**, 165-185.

Strobbia, C. and S. Foti, 2006, Multi-offset phase analysis of surface wave data (MOPA): Journal of Applied Geophysics, **59**, 300-313.

Vignoli, G. and G. Cassiani, 2009, Identification of lateral discontinuities via multi-offset phase analysis of surface wave data: Geophysical Prospecting, **58**, 389-413.

Wisén, R. and A.V. Christiansen, 2005, Laterally and mutually constrained inversion of surface wave seismic data and resistivity data: Journal of Environmental & Engineering Geophysics, **10**, 251-262.

Woodhouse, J. H., 1974, Surface waves in a laterally varying layered structure: Geophysical Journal of the Royal Astronomical Society, **37**, 461-490.

Zerwer, A., M. A. Polak and J. C. Santamarina, 2005, Detection of surface breaking cracks in concrete members using Rayleigh waves: Journal of Environmental and Engineering Geophysics, **10**, 295-306.

2- LASER-DOPPLER SEISMIC EXPERIMENTS ON A SMALL SCALE PHYSICAL MODEL

In this chapter I present an application of the processing technique that is described in Chapter 1. The technique is here addressed to process a dataset derived from a small-scale laboratory seismic survey performed on a physical model. The physical model is characterized by a 2D geometry, so that the use of the technique introduced in Chapter 1 is necessary in order to correctly interpret the data. In the previous chapter the method, based on a spatial windowing of seismic traces, was successfully applied to both synthetic and field data: however, such small-scale laboratory experiments offer the possibility to overcome the limitations of the test on both field and synthetic acquisitions, since they provide real data (similar to those obtained from a field campaign) which are however extracted from a model whose geometry and mechanical properties are known (as in the case of numerical simulations).

ABSTRACT

Laboratory experiments using laser-based ultrasonic techniques are frequently proposed to study theoretical and methodological aspects of seismic methods, more particularly when experimental validations of processing or inversion techniques are required. Lasers are mainly used to simulate typical field seismic surveys, at the laboratory scale. Most of the time, homogeneous and consolidated materials such as metals and thermoplastics are used to build small-scale physical models of the Earth. Both their geometry and mechanical properties can be perfectly controlled, which makes it possible to address with real data, the efficiency, the robustness or the limitations of studied methods. The use of granular materials is suggested here to enable the physical modelling of seismic methods in more complex and porous media, constituted by lateral heterogeneities, property contrasts and velocity gradients. We were able to construct a physical model with two layers presenting distinct in-depth velocity gradients, separated by a sloping interface. We used this physical model to address the efficiency of an innovative surface-wave processing technique developed to retrieve two-dimensional (2D) structures from a limited number of receivers, using a spatial windowing based on a set of Gaussian windows with different shape. A step by step inversion procedure yielded accurate and meaningful results so that the 2D

structure of the physical model was satisfactorily reconstructed, although strong a priori knowledge was required. Interestingly, the gravity-induced velocity gradients within each layer were accurately retrieved as well, confirming current theoretical and experimental studies regarding guided surface acoustic modes in unconsolidated granular media.

INTRODUCTION

Non-contacting ultrasonic techniques, such as mechanical-wave generation using high frequency laser sources and particle motion measurement using laser-Doppler interferometers, recently appeared to represent powerful tools to address the physics of various processes in geosciences. In geophysics, their non-contacting character provides flexibility that, if combined with high-density sampling abilities, gives the opportunity to simulate typical seismic records in the laboratory. This approach proved to be efficient in the physical modelling of seismic-wave propagation at various scales, thus providing a wide range of applications in civil engineering (Bodet et al., 2005, 2009), exploration seismic (Campman et al., 2005) or seismology (van Wijk et al., 2004). Bodet et al. (2010) recently addressed the ability of laser-Doppler experiments in the systematic characterization of granular materials involved in geological analogue modelling. A methodology has been validated on an unconsolidated granular laboratory medium, perfectly characterized in terms of elastic parameters by Jacob et al. (2008). A mechanical source and a laser-Doppler vibrometer were used to record small-scale seismic lines at the surface of the granular medium. Pressure-wave first arrival times and P-SV waves dispersion were then inverted for one-dimensional (1D) Pressure- and Shear-wave propagation velocity profiles with depth. Inferred velocity structures appeared to match previously thoroughly estimated properties of the probed medium, thus validating this approach (Bodet et al., 2010). The present work involves similar experiments, performed in order address their ability in the imaging of laterally varying granular structures in the context both geological analogue and seismic modelling. The experimental set-up described above was reproduced with a two-layer model presenting a sloping interface.

PHYSICAL MODEL PREPARATION

Granular materials (such as natural sand, granular silica or glass beads) offer an evident flexibility in terms of physical models construction and choice of parameters. Their mechanical properties are the subject of active investigations in various application fields (Valverde and Castellanos, 2006; Hentschel and Page, 2007) and they are widely used for both geological and physical modelling purpose. However, these materials remain delicate to manipulate as soon as the experiments involve great quantities but still require the medium homogeneity to be controlled. In this study, the medium preparation basically reproduced the technique previously proposed by Jacob et al. (2008) and Bodet et al. (2010) and originally designed to set-up an unconsolidated granular packed structure under gravity. This technique has been recently thoroughly addressed in terms of reproducibility of the medium preparation using micrometric glass beads (Bodet et al., 2011). Similar glass beads were chosen here to build a two-layer physical model presenting both in-depth property gradients and a sloping interface, as shown on Figure 2.1a.

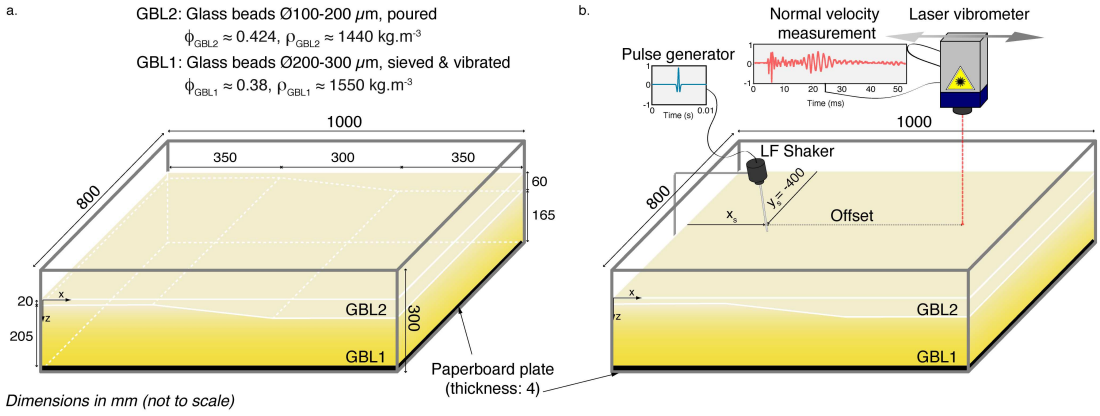

Figure 2.1 – Laser-Doppler experiments: preparation of the medium and experimental set-up. (a) The medium consisted of two glass beads layers (GBL1 and GBL2) prepared in a wooden box and presenting a sloping interface. φ_{GBL} and ρ_{GBL} are the layers bulk porosities and densities respectively. (b) laser-Doppler vibrometer used to record seismograms of particle vertical velocity at the surface of the medium excited by a mechanical source at position (x_s ,y_s). Following a step by step procedure, the laser scanned the surface and, thanks to an oscilloscope, particle normal velocities were recorded at each offset along a linear section (line), the source remaining still.

The glass beads (GB) presented two ranges of diameter: 200-300 μm (GB1) and 100-200 μm (GB2). These GB were sieved or poured into a 1000×800×300 mm box, presented on Figure 2.1a. Compared to the experiments previously cited, Bodet et al. (2010) chose the box dimensions large enough to limit wave-reflections from sidewalls and consequently avoid boundary effects. However, due to obvious practical limitations in terms of material quantities and model weight, the height of the box remained too small to avoid bottom reflections. The bottom of the box moreover consisted of a micrometric metallic sieve glued on a perforated plate that was originally built to inject over-pressured air into the granular material and to study the influence of pore overpressure on seismic-wave propagation at very low confining pressures (Bodet et al., 2011). Strong bottom reflections were thus expected due to high impedance contrast between the granular material and the metallic sieve. In order to mitigate such bottom reflections and their possible influence on the data, several countermeasures were proposed by Bodet et al. (2011), among which the simple setting up of a 4 mm thick paper-board plate onto the sieve (depicted by the thick black line on Figure 2.1).

The bottom layer of the physical model (GBL1 on Figure 2.1a) was built by sieving GB1 through a 400-micron sieve. This layer was compacted every centimetre by means of a flattening tool and vibrations applied to the box. Its final thickness was 205 mm. The bulk porosity (φ_{GBL1}) and density (ρ_{GBL1}) of the medium were estimated by means of laboratory measurements as equal to 0.38 and 1550 kg m^{-3} respectively. A sloping surface was then thoroughly dug by one centimetre steps between the positions x=350 mm and x=650 mm, as presented on Figure 2.1a. The slope was approximately 7.6°. The sloping interface was graded flat by stamping the surface with a flattening tool, as recommended by Buddensiek (2009). The top layer (GBL2 on Figure 2.1a) was finally achieved by thoroughly pouring GB2 onto GBL1. Its final thickness varied from 20 to 60 mm. We did not compact this layer in order to ensure a porosity contrast with GBL2. The bulk porosity (φ_{GBL2}) and density (ρ_{GBL1}) of GBL2 were estimated by means of laboratory measurements as equal to 0.42 and 1440 kg.m^{-3} respectively.

The physical model presents a total thickness of 225 mm and can be considered as a sequence, in the x-direction, of three different geometries: a 2-layer model with an upper layer thickness of 20 mm between the positions x=0 mm and x=350 mm; a 2-layer model with an upper layer thickness varying from 20 to 60 mm between the positions x=350 mm and x=650 mm; a 2-layer model with an upper layer thickness of 60 mm between the positions x=650 mm and x=1000 mm. The contrast between the two

layers is ensured via the estimated porosities which compare well with previous studies (Sherlock, 1999; Sherlock and Evans, 2001; Graveleau, 2008; Buddensiek, 2009). The porosity of glass beads in GBL1 appears close to the random close packing limit, while it tends to the random loose packing limit in GBL2 (Valverde and Castellanos, 2006). The additional complexity and interest of this physical model is that each layer presents a gravity-induced stiffness gradient that will be described in the following.

EXPERIMENTAL SETUP AND DATA ACQUISITION

As previously proposed for the physical modelling of wave propagation at the laboratory scale (van Wijk et al., 2004; Campman et al., 2005; Bodet et al., 2005, 2009), laser-Doppler acquisitions were performed here to simulate a seismic survey at the surface of the physical model. The experimental set-up, adapted to granular materials by Jacob et al. (2008) and Bodet et al. (2010), basically involved a laser-Doppler vibrometer to record seismograms of particle normal velocity at the surface of the medium which was excited by a mechanical source at position (x_s ,y_s), as presented on Figure 2.1b.

The source was a 3 mm diameter metallic stick attached to a low-frequency (LF) shaker and buried in the granular material with an angle of 20° from the normal to the free surface. The force source signal was sent from a pulse generator to the LF-shaker, exciting the stick. A detailed view of the source set-up and its characteristics are given on Figure 2.2.

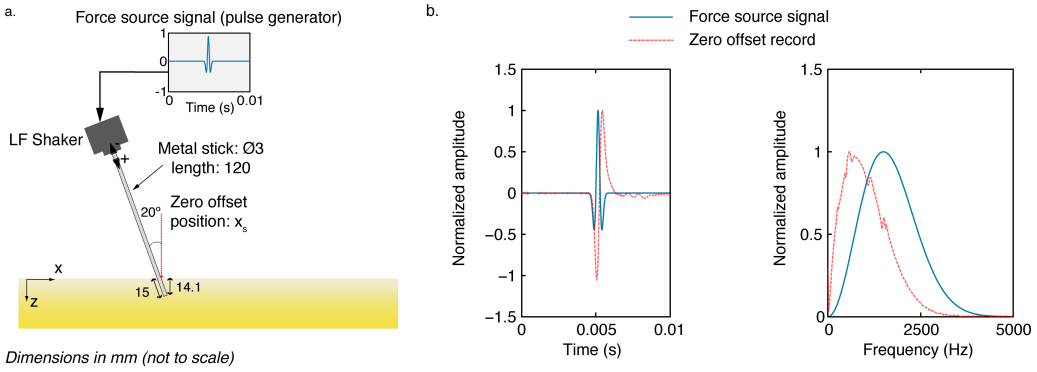

Figure 2.2 – Source set-up and characteristics. (a) The force source signal was sent from a pulse generator to a low frequency (LF) shaker exciting a metallic stick buried in the granular material. (b) The force source signal (blue line) was a Ricker pulse with frequency spectrum centred on 1.5 kHz. Before each seismogram acquisition, the laser beam was set at the zero offset position to record the stick normal velocity (red dashed lines).

The force source signal (blue line on Figure 2.2) was a Ricker pulse with frequency spectrum centred on 1.5 kHz. Before each seismogram acquisition, the laser beam was set at the zero offset position (x_s on Figures 1a and 2a) to record the stick normal velocity (red dashed lines on Figure 2.2b). The zero offset position was actually chosen where the stick enters the medium.

To record a seismogram, the source remained still and the laser-Doppler vibrometer scanned by constant steps (1, 2 or 3 mm) the surface of the granular medium. Using an oscilloscope, up to 300 traces were recorded in linear single-channel walkway mode, parallel to the long edges of the box (see Table 2.1 for details about the acquisition geometries). Each trace was stacked 50 times and the time sampling rate was 100 kHz over 5002 samples. Each seismogram was 300 mm long. As shown on Figure 2.3a a first seismogram of particle vertical velocity was recorded at the surface of GBL1 before the preparation of the sloping interface.

Table 2.1 – acquisition parameters of collected seismograms (illustrated on Figure 2.3)

Line	Source position x_s (mm)	Spacing between traces (mm)	Total number of traces	Source–first receiver distance (mm)	Source–last receiver distance (mm)	Sampling rate (kHz)	Time samples
1	350	3	100	3	300	100	5002
2	50	2	150	2	300	100	5002
3	370	1	300	1	300	100	5002
4	950	2	150	2	300	100	5002
5	650	1	300	1	300	100	5002

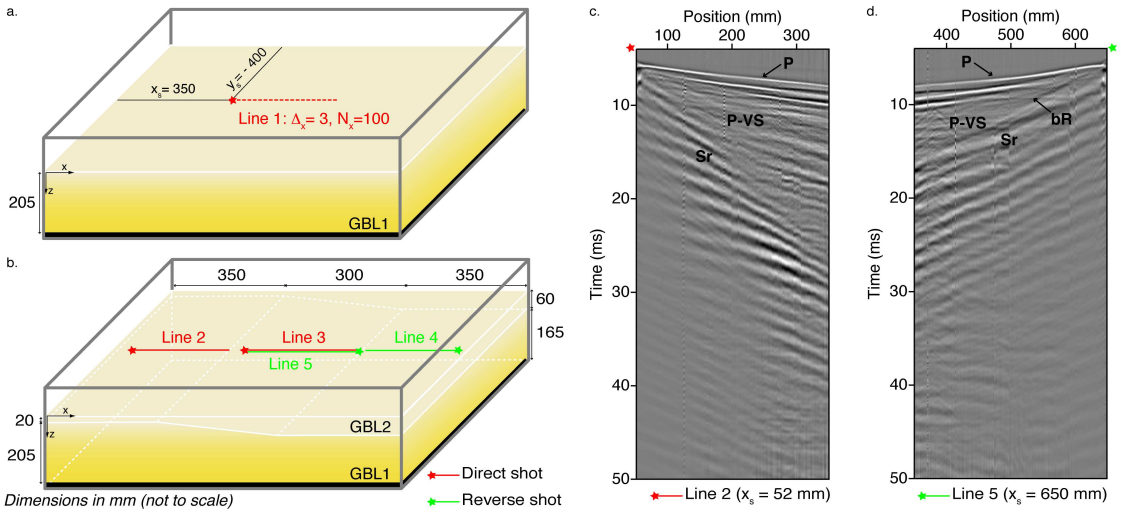

Figure 2.3 – Laser-Doppler experiments: data acquisition. (a) A seismogram (Line 1) was recorded at the surface of GBL1 before the preparation of the sloping interface (100 traces with 3 mm spacing). (b) Four seismograms were recorded on the two-layer physical model. The lines are red when the laser scanned lines along the positive x-direction (direct shot) and green along the negative x-direction (reverse shot), the stars giving sources position. The recorded lines were 300 mm long with a space-sampling interval of 2 mm above the flat interface part of the model (Lines 2 and 4) and of 1 mm above the slope (Lines 3 and 5). (c, d) Two example seismograms recorded along Line 2 (c) and Line 5 (d) show that, despite strong amplitudes associated to the source ringing (Sr), the recorded wavefields clearly present coherent events such as P- and P-SV wave trains. Along the Line 5, it is possible to guess bottom-reflected arrivals (bR).

This seismogram should allow a good characterisation of the bottom layer. Once the final model was prepared, four seismograms were recorded at its surface (on Figure 2.3b). Only one shot was recorded above each horizontally layered (1D) part of the model (Line 2 and Line 4 on Figure 2.3b). However, the 2D central part was probed using both direct and reverse shooting (Line 3 and Line 5 on Figure 2.3b) in order to provide an optimal data-set to be processed using the technique proposed by Bergamo et al., (2010). The recorded lines were 300 mm long with a space sampling interval of 2 mm above the flat-interface parts of the model (Lines 2 and 4) and of 1 mm above the sloping interface (Lines 3 and 5). As examples, the seismograms recorded along Line 2 and Line 5 are presented on Figure 2.3c and Figure 2.3d respectively.

The recorded wavefields clearly present coherent events such as P- and surface wave trains (P and P-SV on Figures 3c and 3d). Along the Line 5, it is possible to guess bottom-reflected arrivals (bR on figure 2.3d). The seismograms are however corrupted by strong amplitudes typically related to the source ringing (Sr on Figures 3c and 3d). These experimental artefacts will be mitigated by deconvolution with the source signal, recorded at the zero offset position (Figure 2.2b). The P-SV events identified on every seismogram can be quantitatively interpreted using typical seismic surface-wave processing techniques, as proposed by Bodet et al. (2010). An important improvement of the methodology proposed here consists in applying the technique previously developed by Bergamo et al. (2010) to retrieve the lateral variation of shear-wave velocities in the physical model.

SURFACE WAVE DISPERSION EXTRACTION

A - Pre-processing of data

Once traces were collected, a pre-processing stage was necessary before the dispersion curves extraction. First of all, a high-pass filter at 100 Hz was applied in order to suppress ambient noise that might have corrupted the acquisitions. Secondly, raw seismograms (Figure 2.4) appeared affected by evident source ringing as noticed in the previous section (Figure 2.5). Moreover, during one of the acquisitions (line 3) an electrical shutdown occurred: as we started again to acquire, it was not possible to set the laser in the exact position where it was before the interruption, so that the traces acquired after the shutdown appear to be slightly misplaced in the final raw seismogram (see Figure 2.6a). The strategies we adopted for these two problems were the traces

deconvolution with the source signal for the ringing suppression and an estimate of the actual position of the misplaced traces by means of cross-correlation.

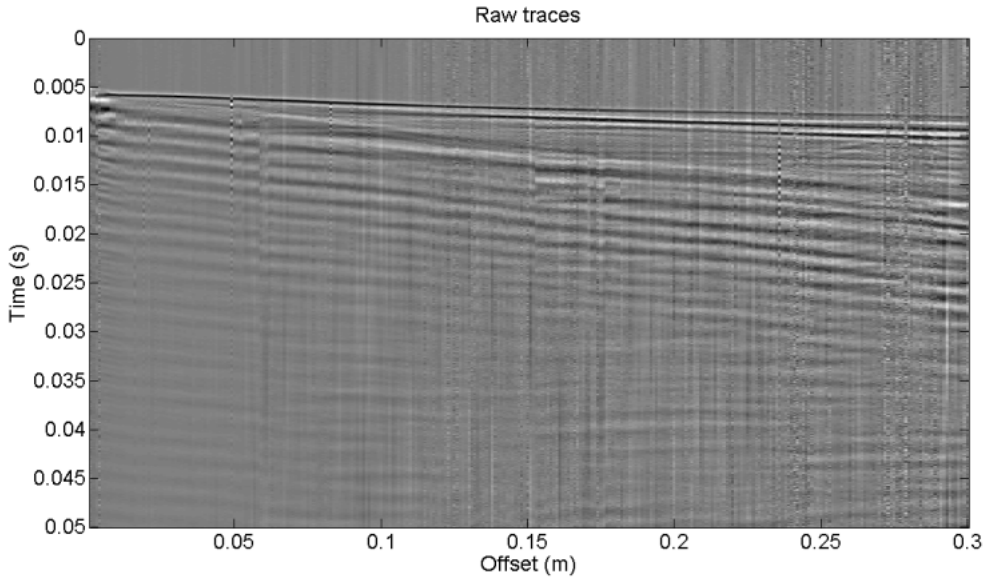

Figure 2.4 – Line 5: raw seismogram.

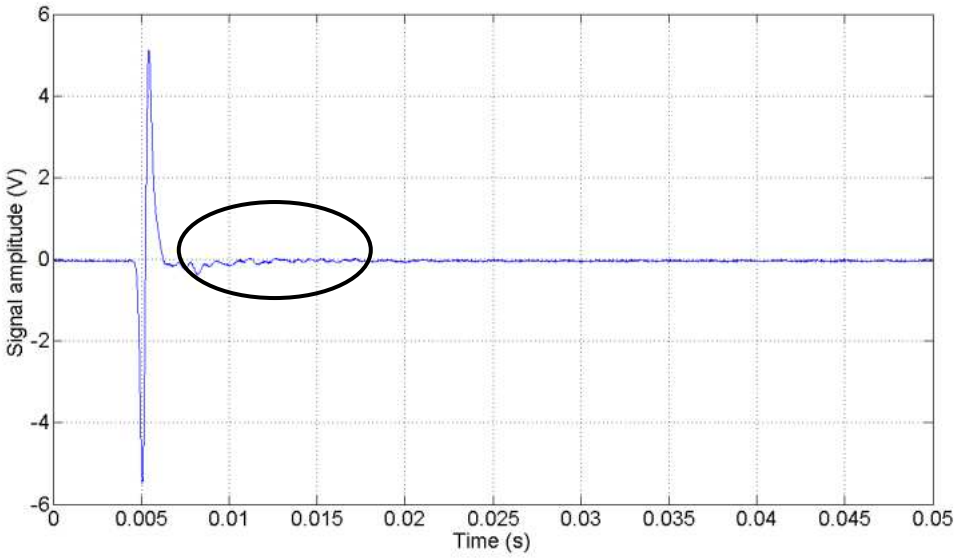

Figure 2.5 – Source signal from line 5. Source ringing is clearly evident in the trace portion in the circle.

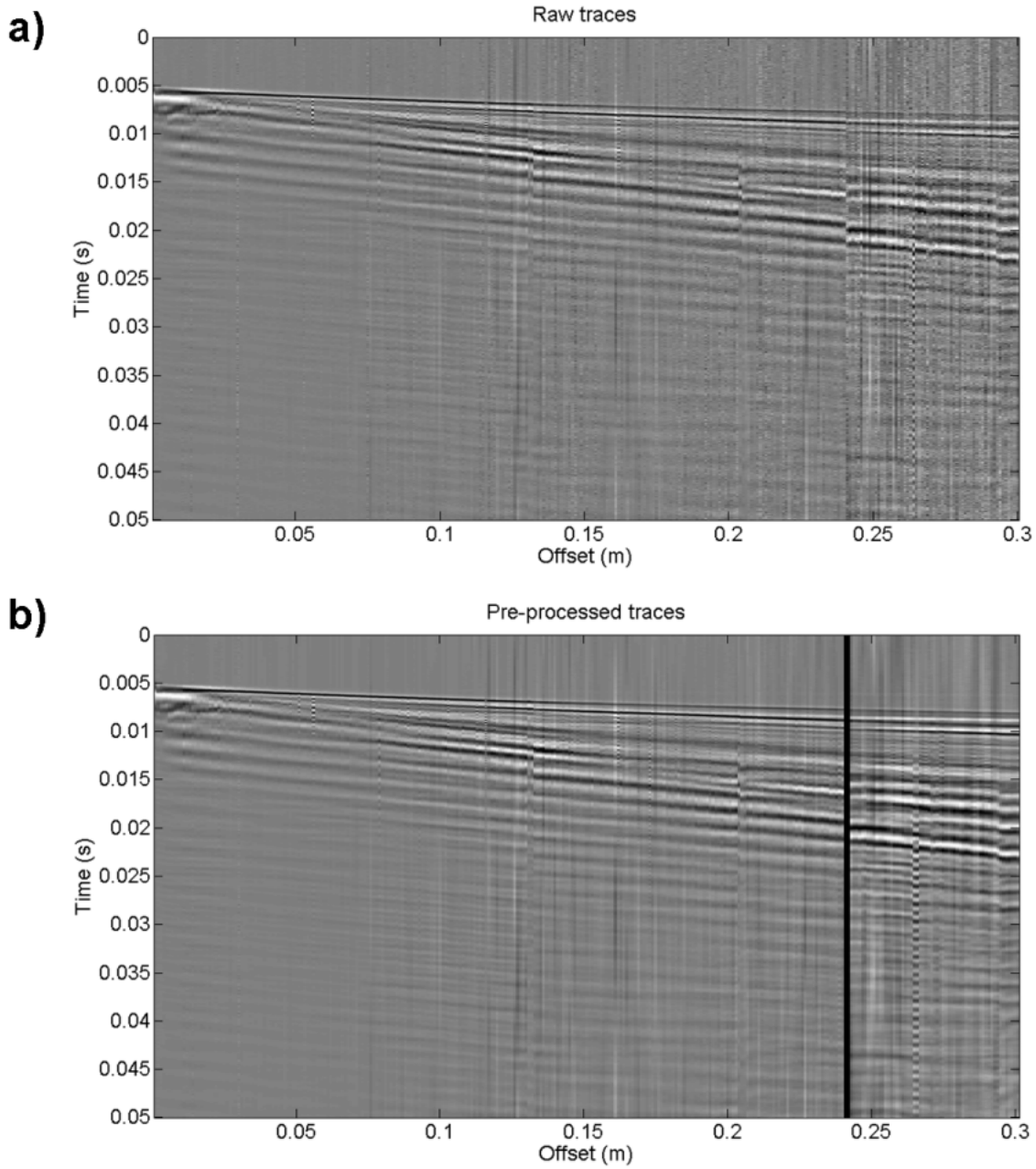

Figure 2.6 – Line 3 raw traces (a) and after the gap recovery (b).

To mitigate the ringing in the seismograms, raw traces were deconvolved with the source signal (i.e. the signal that was recorded by setting the laser beam on the stick just before it plunges into the glass beads bed, see Figures 2.2 and 2.5). The result is presented in Figure 2.7, displaying the traces of Figure 2.4 after deconvolution: ringing is attenuated and data quality has improved. Figure 2.6a shows the raw traces from Line 3 whose recording was interrupted by a power shutdown. At around 0.24 m offset there is a clear discontinuity in the seismogram: such oddity is due to the fact that the traces recorded after the shutdown (which are beyond 0.24 m offset) are displayed at an offset

that is slightly smaller than the actual one. In order to retrieve the actual position of these traces we crosscorrelated the P-wave arrival parts of neighbouring traces to estimate the time lapse occurring between them.

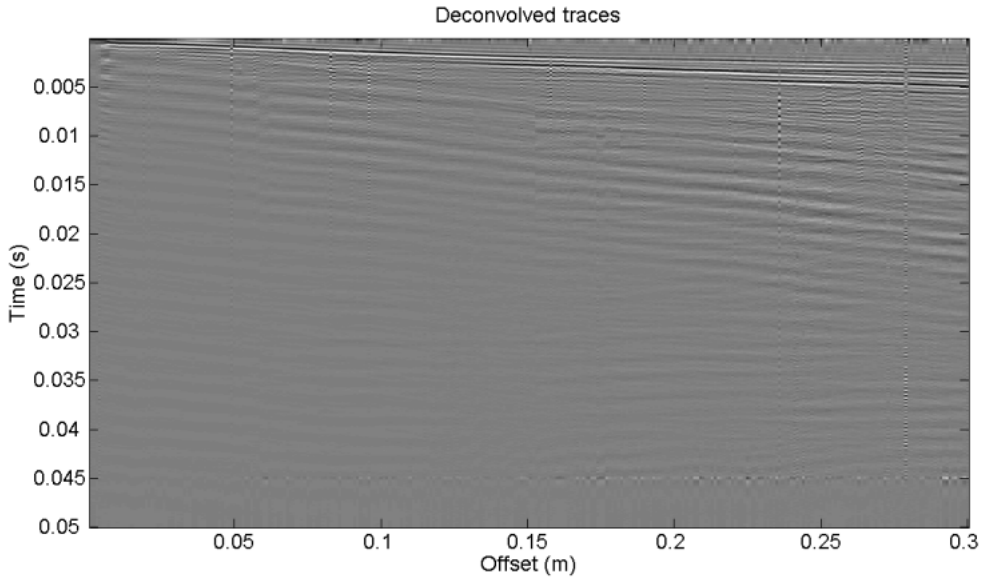

Figure 2.7 – Line 5 traces after deconvolution

Therefore, a comparison between the average time lapse before the gap and the time lapse at the discontinuity allowed estimating the shift in space that was required to move the traces of the seismogram at a proper offset. The gap was then filled with blank traces (see Figure 2.6b for the final result).

B - Dispersion curves extraction

First of all, we extracted a dispersion curve from every shot by applying an *f-k* transform to the seismograms and then picking the energy maxima on the spectra (Figure 2.8): these dispersion curves are displayed in Figure 2.9.

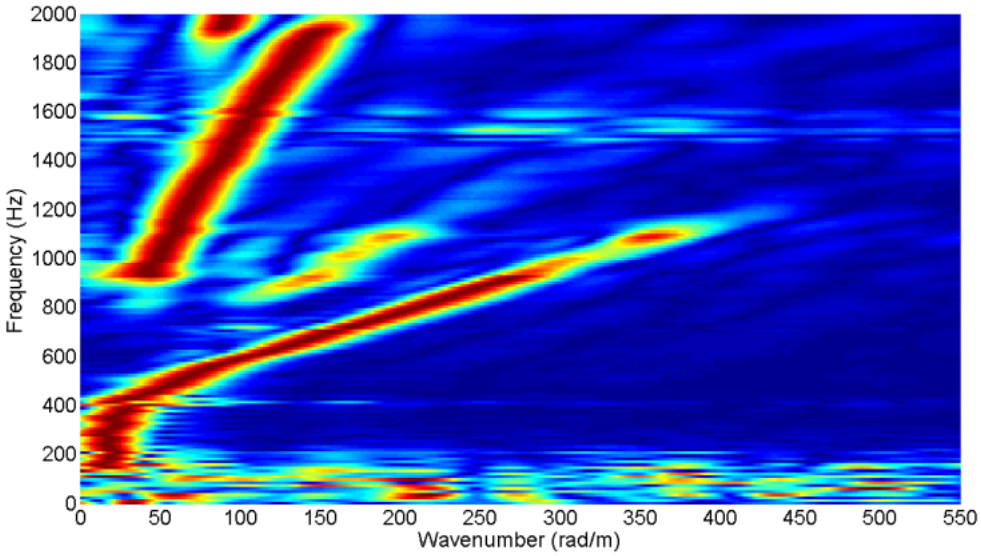

Figure 2.8 – Normalized f-k spectrum from line 2 seismogram.

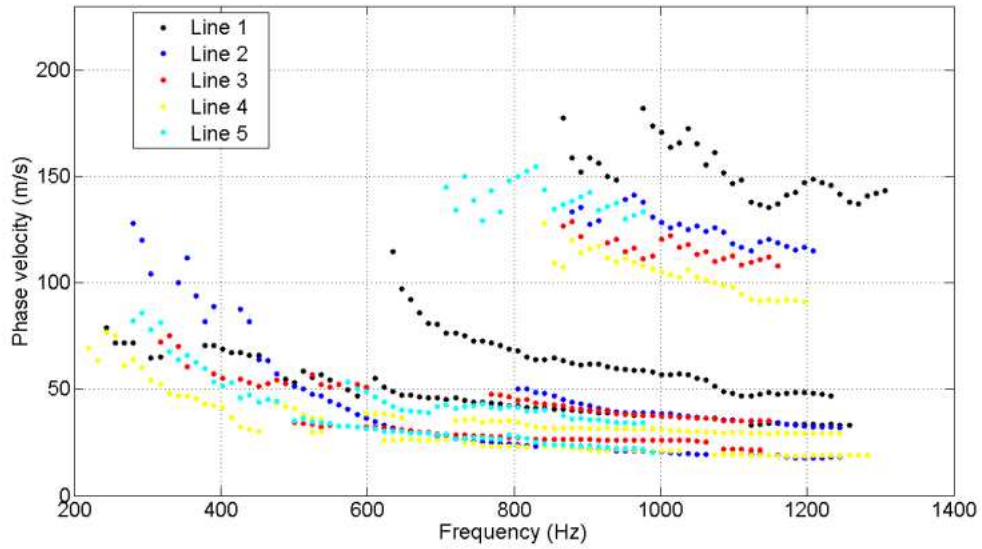

Figure 2.9 – Dispersion curves from the five survey lines

All curves are characterized by the presence of three surface-wave propagation modes: not surprisingly, the dispersion curve from Line 1 is characterized by higher phase velocity values, as the lower layer is stiffer than the upper one. As for the other four dispersion curves (Lines 2-5), fundamental mode phase velocities are quite similar from 600 Hz on: at lower frequencies the dispersion curves are affected by the lower layer and show a rapid increase of the velocity. In particular, the frequency at which this increase takes place depends on the interface depth and therefore is roughly the same (about 500 Hz) for the two dispersion curves relevant to the dipping interface part of the model and it is smaller (around 400 Hz) for the dispersion curve retrieved from the

portion of the model where the interface is deeper (60 mm). Moreover, to get a better description of the lateral variation of the physical model, we applied to the central shots (Lines 3 and 5) an algorithm developed by Bergamo et al. (2010) based on a spatial windowing of the traces to extract a set of dispersion curves from a single shot. This method applies to the seismogram a spatial windowing which is based on Gaussian windows whose maxima span the survey line thus assigning from time to time a different weight to the same trace in order to retrieve a set of dispersion curves each of them referring to a different subsurface portion. These dispersion curves are reported on Figure 2.10, where are related to different positions of the Gaussian window maxima along the receiver spread.

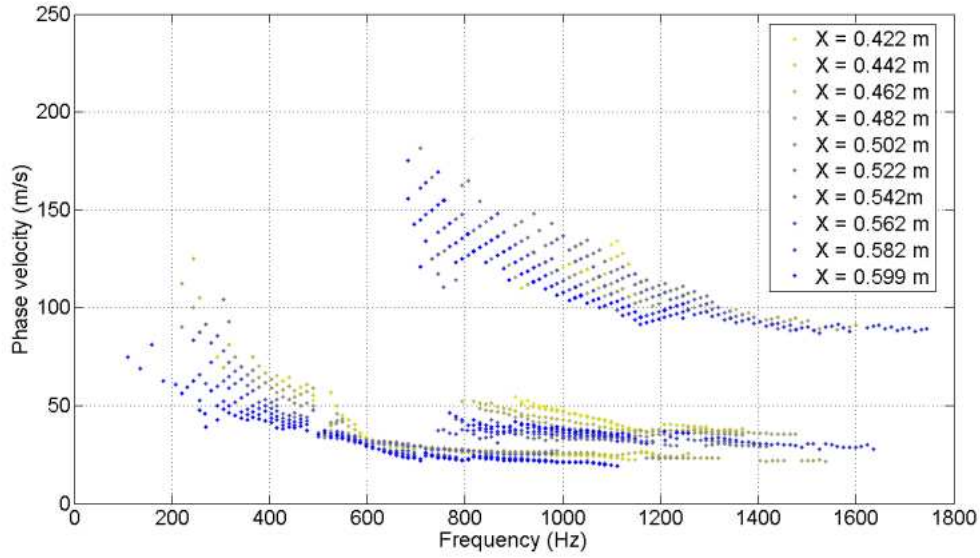

Figure 2.10 - Dispersion curves retrieved from lines 3 and 5 seismograms by applying a space-varying spatial windowing

Again, three propagation modes are identified: as seen in Figure 2.9 the velocity of the fundamental modes starts to differ at 600 Hz (the deeper the interface, the lower the phase velocities and vice versa). This effect can be clearly seen in Figure 2.11, where the ten dispersion curves referring to the sloping interface portion of the model and the two curves relevant to the 1D portions are represented in terms of pseudo-depth (wavelength/2.5) versus pseudo-V_s (phase velocities times 1.1).

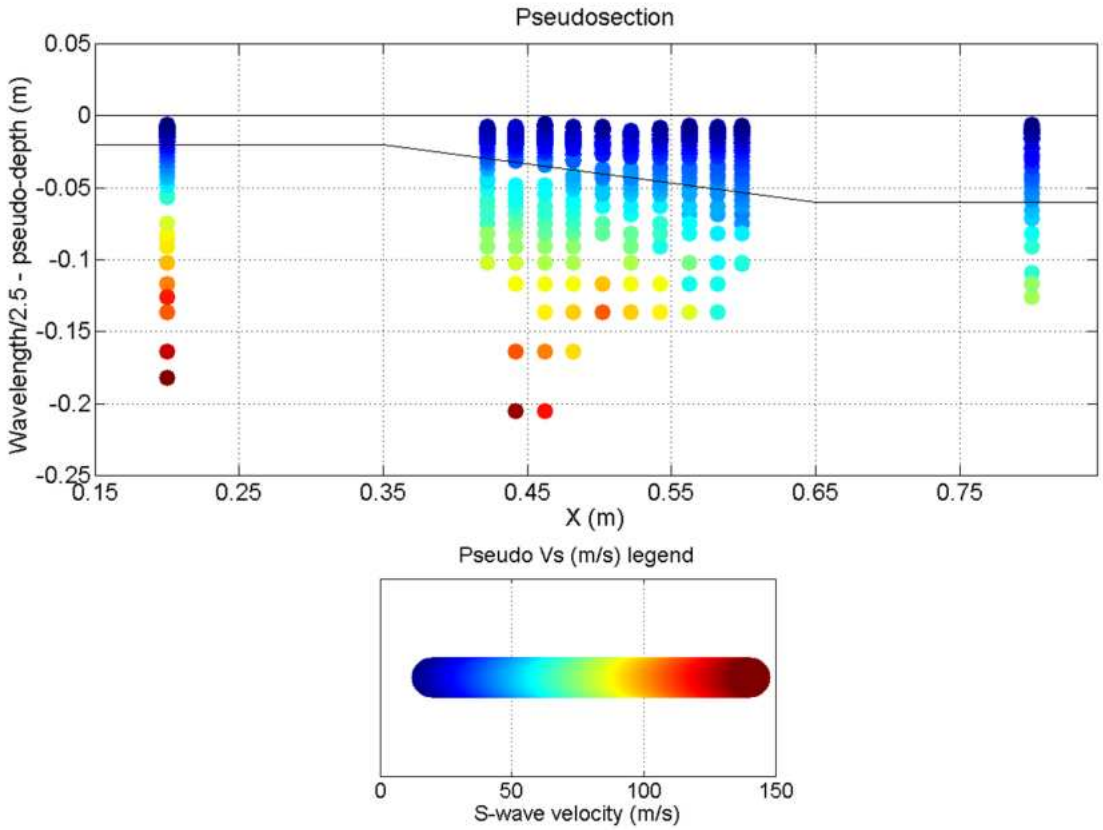

Figure 2.11 – Dispersion curves fundamental modes represented in terms of pseudo-depth (wavelength/2.5) versus pseudo-V_s (phase velocity times 1.1).

DISPERSION CURVES INVERSION

The last stage of the process involved the dispersion curves inversion. As already successfully done by Jacob et al. (2008) and Bodet et al. (2010) we adopted the relationship introduced by Gassmann (1951) where P- and S-wave velocity are considered as power-law dependent on overburden pressure:

$$V_{P,S} = \gamma_{P,S}(\rho g z)^{\alpha_{P,S}} \qquad (1)$$

where g is the gravity acceleration, z is the depth, ρ is the bulk density, $\gamma_{P,S}$ is a depth-independent coefficient mainly depending on the elastic properties of the grains and $\alpha_{P,S}$ is the power-law exponent. We therefore assumed that in the two-layer physical model the S-wave velocities follow a power-law trend which is controlled by five parameters: the two couples of α_S and γ_S for the upper and lower layer, and the interface depth. Within each layer, the bulk density can be assumed constant with depth even if it may slightly vary in the vicinity of the free surface, at pressures less than 75 Pa, as previously noted by Jacob et al. (2008). However, the contribution of such density

variation to velocity change with depth is indeed negligible (Gusev et al., 2006). The whole inversion process was subdivided into three successive steps:

a) estimating parameters α_S and γ_S for GBL2;

b) estimating parameters α_S and γ_S for GBL1;

c) estimating the interface depth.

In the following paragraphs, the three inversion steps are extensively described.

A - Retrieving parameters α_S and γ_S for the lower layer

As described in the experimental set-up and data acquisition section, a first seismogram was acquired on top of GBL1 before digging the slope and adding the glass beads for GBL2 (Line 1, Figure 2.3a). Therefore, the acquired data could be used for the estimation of α_S and γ_S for GBL1. A dispersion curve was extracted by picking the energy maxima on the *f-k* spectrum derived from the seismogram (see black dotted curve on Figure 2.9).

Prior to the model construction, we performed a series of numerical FEM (finite element method) simulations for the calibration of the physical model: these simulations showed that, in case of a single layer model, the dispersion curve fundamental mode represented in terms of pseudo-depth (wavelength/2.5) versus pseudo-V_s (phase velocity times 1.1) follows with a good level of approximation the S-wave vertical velocity distribution described by equation 1 (see Figure 2.12a). This agreement does not hold true in case of a two or more layer model (Figure 2.12c). Most probably, the relatively great acoustic impedance contrast between the glass beads layers causes a mode jump in the experimental dispersion curve at low frequencies (Figure 2.12d), so that the curve represented as pseudo-depth versus pseudo-V_S does not follow the trend expected by equation 1 for pseudo-depths greater than the interface depth (Figure 2.12c). In order to optimize the agreement between the dispersion curves represented in pseudo-V_S versus pseudo-depth and the actual trend of V_S with depth we performed a parametric analysis to determine the optimal value for the ratio between wavelengths and pseudo-depths. We ran a FEM analysis simulating the propagation of body and surface waves through a horizontally homogeneous medium with mechanical properties similar to the ones of the physical model media and whose vertical profile of V_s with depth is described by equation 1, assuming γ_S = 5.25, α_S = 0.33 and ρ = 1580 kg/m^3. From the synthetic seismogram (Figure 2.13a), by applying the surface wave method, we extracted a dispersion curve (Figure 2.13b).

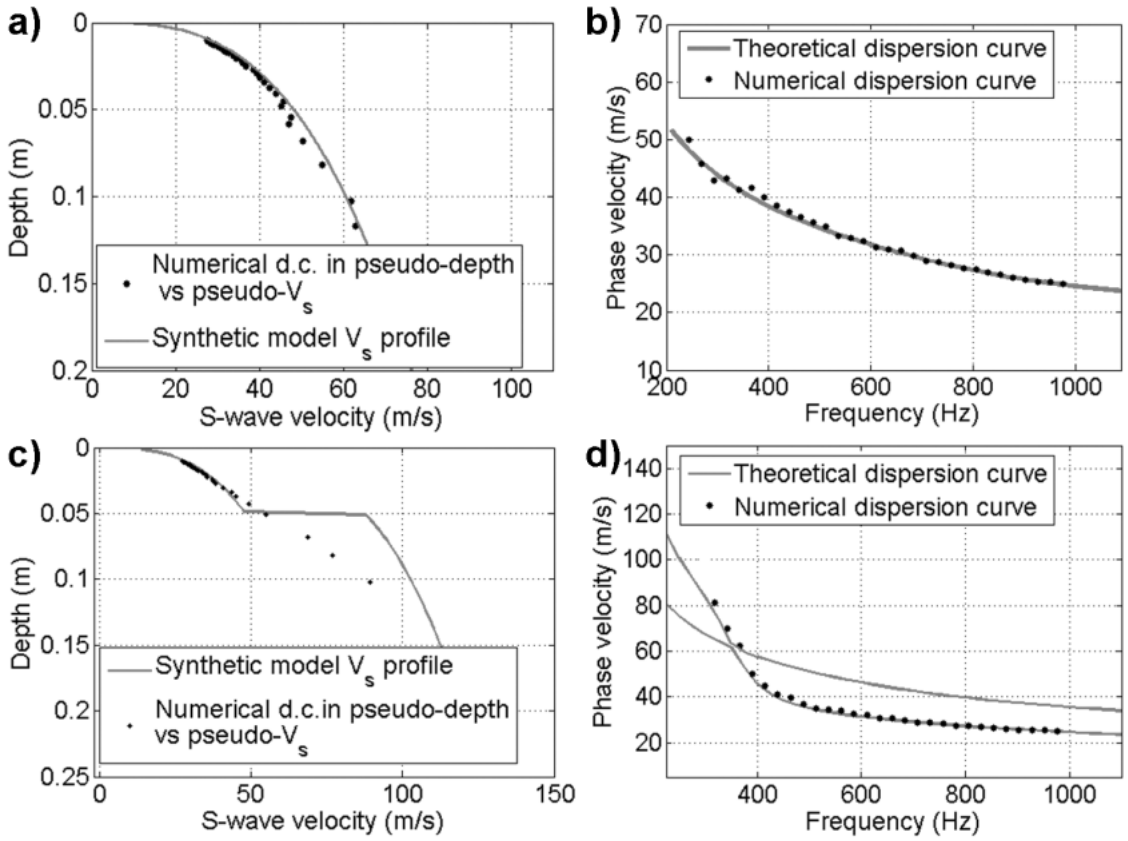

Figure 2.12 – a) Comparison between the power law V_S profile of the one-layer synthetic model (gray line) and the dispersion curve (black dots) extracted from the shot that was numerically simulated on the synthetic model. The dispersion curve is here represented in terms of pseudo-depth (wavelengths/2.5) versus pseudo-V_S (phase velocities times 1.1). b) Theoretical dispersion curve (gray line) for the V_S profile of the synthetic model of (a) and extracted dispersion curve (black dots: same as in (a), but represented in frequencies vs phase velocities). c) Comparison between the power law V_S profile of the two-layer synthetic model (gray line) and the dispersion curve (black dots) extracted from the shot that was numerically simulated on the synthetic model itself. The dispersion curve is represented in terms of pseudo-depth (wavelengths/2.5) versus pseudo-V_S (phase velocities times 1.1) d) Theoretical dispersion curve (gray line) for the V_S profile of the synthetic model of (c) and extracted dispersion curve (black dots: same as in (c), but represented in frequencies vs phase velocities).

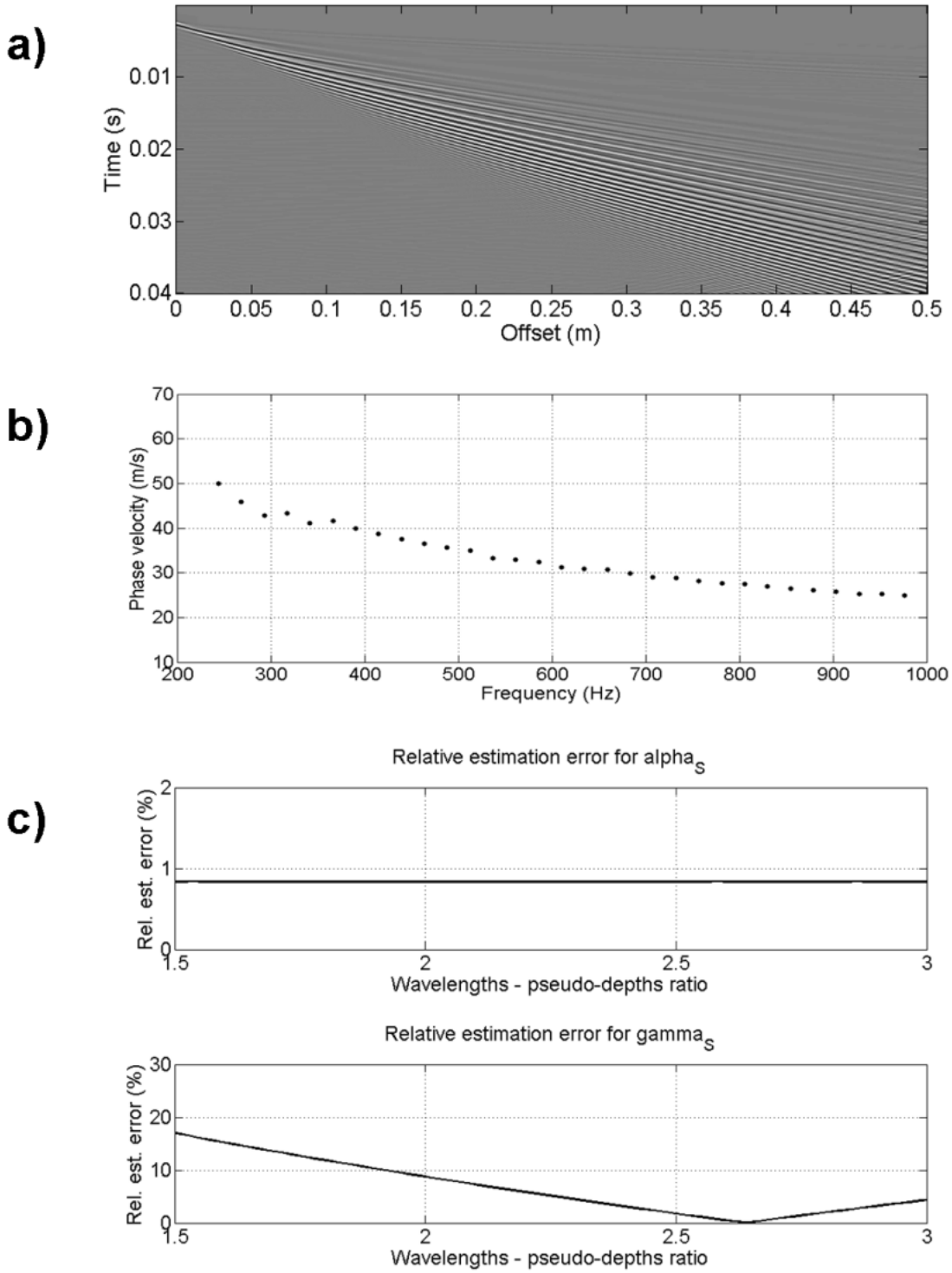

Figure 2.13 – a) Synthetic seismogram from FEM simulation; b) extracted dispersion curve; c) relative error in the estimation of α_S and γ_S as a function of the assumed ratio between wavelengths and pseudo-depths.

This dispersion curve was then translated to the pseudo-V_S – pseudo-depth plane assuming 1.1 as the ratio between pseudo-V_S and the Rayleigh wave phase velocities (Abbiss, 1981) and by successively adopting a different value for the ratio between wavelengths and pseudo-depths, chosen within the range 1.5 – 3. For every value of ratio between wavelengths and pseudo-depths, γ_S and α_S were estimated by linearizing equation 1 and applying a least square approach:

$$\begin{bmatrix} \log(\gamma_S) \\ \alpha_S \end{bmatrix} = \left(\mathbf{G}^{\mathrm{T}}\mathbf{G}\right)^{-1}\mathbf{G}^{\mathrm{T}}\log(\mathbf{v_S}) \tag{2}$$

where $\mathbf{v_S}$ is the vector of pseudo-V_S of the extracted dispersion curve and

$$\mathbf{G} = \begin{bmatrix} 1 & \log(\rho g z_1) \\ \dots & \dots \\ 1 & \log(\rho g z_{n-1}) \\ 1 & \log(\rho g z_n) \end{bmatrix} \tag{3}$$

with g the gravity acceleration, ρ the bulk density and $z_1 \dots z_n$ the pseudo-depths of the extracted dispersion curve.

As shown in Figure 2.13c, the estimation of α_S is not influenced by the value of the dividend translating the wavelengths into pseudo-depths, while the lowest estimation error for γ_s is obtained for the dividend equal to 2.62. Hereafter, we will use this value to express the ratio between wavelengths and pseudo-depths.

Being the physical model before the addition of GBL2 a single layer model, we used the dispersion curve from Line 1 (Figure 2.9) reproduced in terms of pseudo-depth versus pseudo-*Vs* for the estimation of parameters α_S and γ_S controlling the S-wave vertical velocity distribution in GBL1. We adopted a grid search approach (on the fundamental mode only): its results are reported in Figure 2.14, where the misfit evaluated for every possible couple of α_S and γ_S is displayed on a logarithmic scale (Figure 2.14a). The couple yielding the minimum misfit value is $\alpha_S = 0.345$ and $\gamma_S = 6.5$: Figure 2.14b reports the good agreement between the experimental points and the power-law S-wave velocity trend determined by these values of α_S and γ_S. On Figure 2.14a, many (α_S, γ_S) couples exhibit low misfit values around the minimum. But even if the corresponding power-laws only theoretically cross at one depth below zero, they remain very close to each other in terms of velocity profiles. This consequently generates equivalent misfit values according to the dispersion estimations errors.

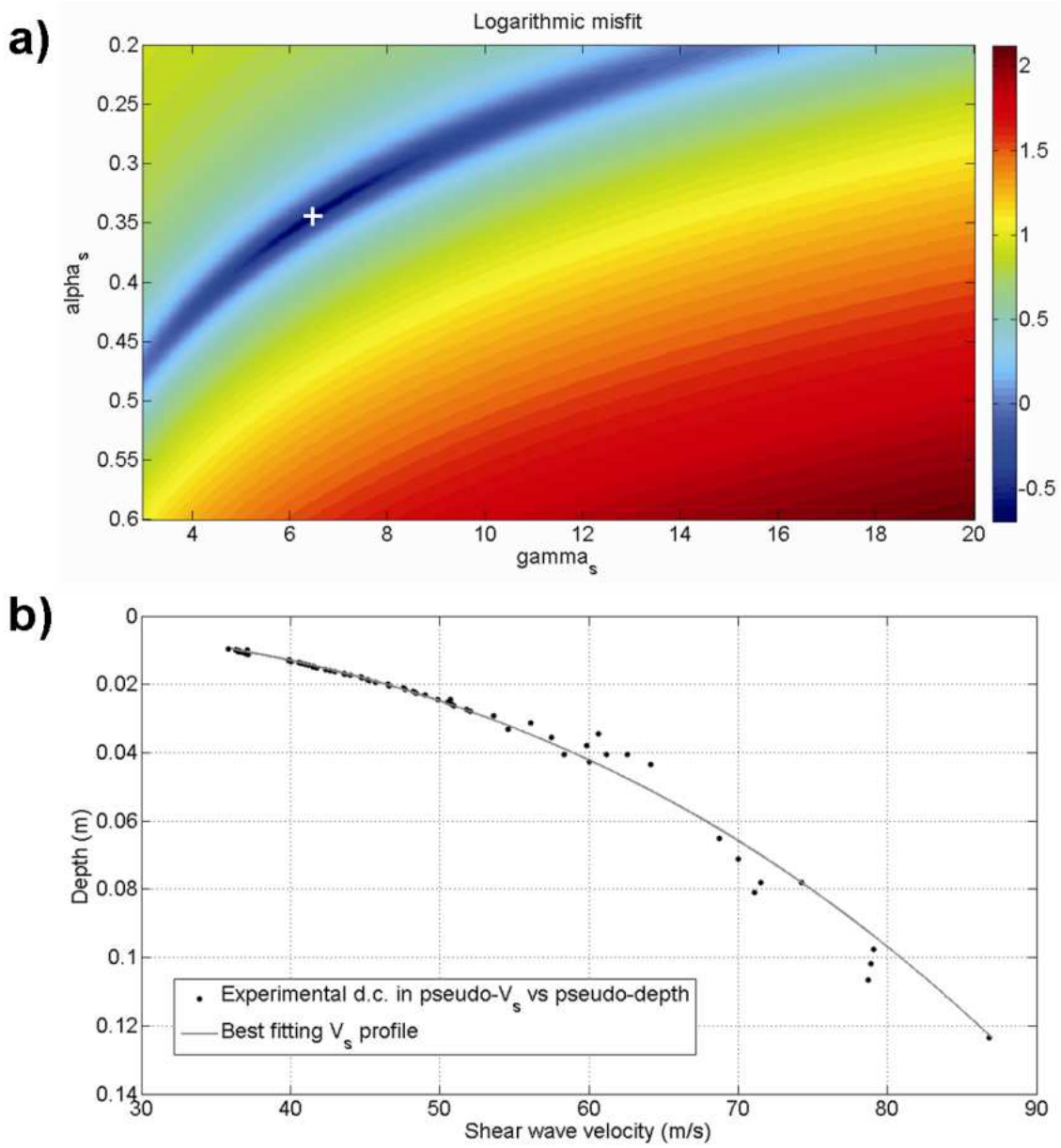

Figure 2.14 – a) Misfit surface in the α_S - γ_S domain for the inversion of the dispersion curve from Line 1: the white cross marks the position of the minimum misfit point; b) comparison between the experimental dispersion curve represented in terms of pseudo-depth versus pseudo-V_S and the best fitting V_S profile.

B - Retrieving parameters α_S and γ_S for the upper layer

The second step of the inversion process involved the estimation of the couple of α_S and γ_S controlling the power-law behaviour of the S-wave velocity in GBL2. Differently from what had been done for GBL1, values for α_S and γ_S were determined for every dispersion curve extracted from the seismograms acquired on the top of the upper layer (Figure 2.10). The lower layer, as described in the experimental set-up section, was arranged into the box with special cares (i.e. glass beads were sieved and compacted every centimetre) and, at the end of the deposition process, a greater compaction was achieved by vibrating the wooden box. Therefore, such compaction is quite likely to ensure material homogeneity and constant values of α_S and γ_S, on the contrary, the upper layer glass beads were simply poured, so that slight heterogeneities and different S-wave velocity behaviours (and therefore α_S and γ_S values) are expected over the model.

As already shown in the previous paragraph, in case of a multi-layer granular model, the experimental dispersion curve fundamental mode represented in terms of pseudo-depth versus pseudo-V_S follows the exponential trend described by equation 1 until the upper interface depth (Figure 2.12c). The basic idea was then to use the experimental fundamental modes points with pseudo-depths smaller than the interface depth to estimate α_S and γ_S for the upper layer similarly to what had already been done for the lower layer. However, the interface depth is not precisely known, as first layer smaller glass beads might have leaked down among larger lower layer glass beads (thus turning the interface into a transition zone): moreover, interface depth is also one of the parameters to be retrieved through inversion.

Therefore, the following approach was adopted for each dispersion curve:

- dispersion curve Rayleigh wave fundamental mode is represented in terms of pseudo-depth versus pseudo-V_S (Figure 2.15a);
- the experimental points are sorted with increasing values of pseudo-depth (z);
- a "for" loop over the n points of the experimental curve is implemented. For every i^{th} iteration (with i ranging from 2 to n) only the first i points are considered (i.e. the points up to the i^{th} z value): parameters α_{Si} and γ_{Si} are computed with a least squares approach (see equations 2 and 3), minimizing the misfit m_i between $\mathbf{v}_{\mathbf{S,theor}} = \gamma_{Si}(\rho g \mathbf{z}(1:i))^{\alpha_{Si}}$ and the experimental pseudo-V_S values $\mathbf{v}_{\mathbf{S,exp}}(1:i)$. At the end of every iteration, α_{Si}, γ_{Si} and the relevant misfit m_i are represented at depth z_i (see Figs 2.15b, 2.15c and 2.15d);

- eventually, the couple of α_S and γ_S describing the V_S behaviour of GBL2 is chosen. Up to a certain depth, in fact, the misfit is low and almost constant: beyond a certain depth threshold, it suddenly increases, because equation 1 is no more able to model the behaviour of S-wave velocity with depth because of the influence of the deeper layer (see Figure 2.15b). Therefore, we chose the α_S and γ_S values at the ones relevant to the greatest depth that still provides low misfit. Moreover, it has been noticed that, not surprisingly, this depth threshold roughly coincides with the expected interface between GBL2 and GBL1.

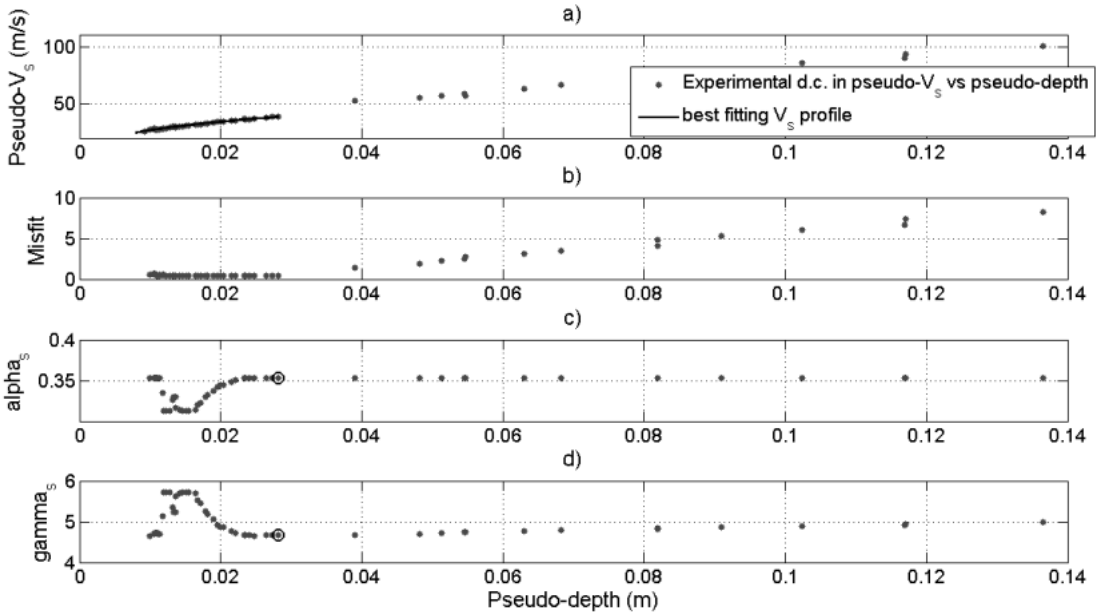

Figure 2.15 – Retrieving parameters α_S and γ_S for GBL2 for the dispersion curve at x=0.462 m. a) Experimental dispersion curve represented in pseudo-V_s versus pseudo-depth (black dots) compared with the best fitting V_s profile (gray line) obtained from the chosen value of α_S and γ_S and computed for the pseudo-depths of the experimental points considered for α_S and γ_S estimation. b) trend of misfit as a function of pseudo-depth, i.e. as a function of the set of points considered for α_S and γ_S estimation. c) Estimated values of α_S versus pseudo-depth. The black circle marks the chosen value for α_S. d) Estimated values of γ_S versus pseudo-depth. The black circle marks the chosen value for γ_S.

Figure 2.16 represents the couples of α_S and γ_S for GBL2 that were retrieved from all dispersion curves. α_S and γ_S values are located at the corresponding dispersion curve position. The estimated α_S and γ_S values (lying within 0.31-0.35 and 4.3-6 respectively)

do not have a large variability and they are in agreement with the results previously achieved by Jacob *et al.* (2008) and Bodet *et al.* (2010, 2011) on similar physical models. The (α_S, γ_S) couples should in fact be constant along the line, this layer being assumed laterally homogeneous. Here again, their slight variability remain satisfying since they lead to close V_S values. Significantly, the power-law parameters retrieved for the upper layer are generally lower than the ones estimated for the lower layer (α_{SGBL1} = 0.345 and γ_{SGBL1} = 6.5) and, in any case, they yield slower S-wave velocity profiles. In particular, α_{SGBL1} roughly coincides with the upper limit of the values for α_{SGBL2} and γ_{SGBL1} is greater than any value retrieved for γ_{SGBL2}: moreover, relatively high values of α_{SGBL2} are associated to relatively low values for γ_{SGBL2} and vice versa, so that all retrieved couples of α_{SGBL2} and γ_{SGBL2} ensure lower V_S values with respect to the ones determined by α_{SGBL1} and γ_{SGBL1}. The lower layer, in fact, was vibrated in order to get a good compaction degree, and greater compaction implies a stiffer medium and therefore higher S-wave velocities.

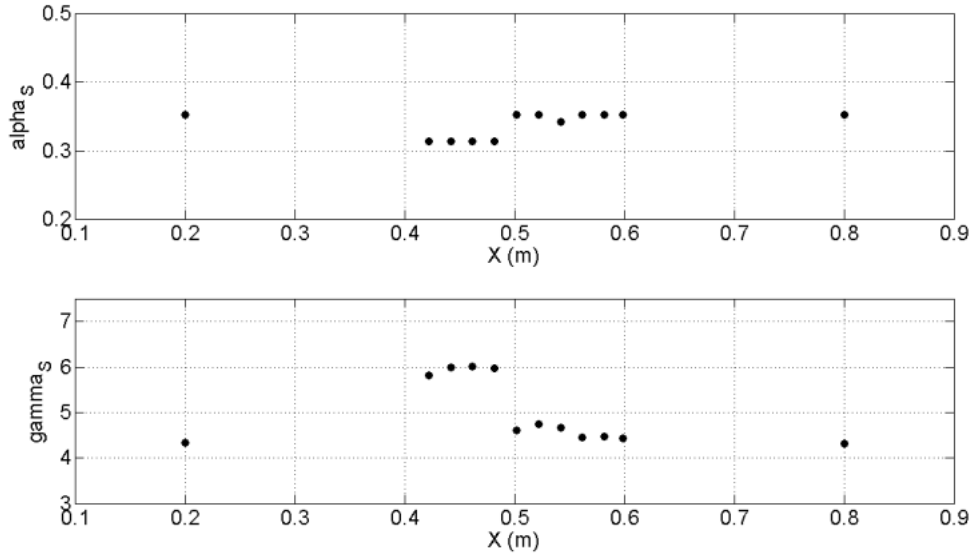

Figure 2.16 – Estimated values of α_S and γ_S for GBL2.

C – Interface depth estimation

Finally the interface depth was estimated for all available dispersion curves. A grid search approach was chosen, made up of the following steps and individually applied to each dispersion curve:

- the interface depth is moved by 1 mm steps within the range 3-90 mm;
- the S-wave velocity profile determined by parameters α_S and γ_S for the upper and lower layer and by the current interface depth is discretized into 1 mm thick layers, so that a theoretical dispersion curve can be computed through the Haskell and Thomson approach (Thomson, 1950; Haskell, 1953 and 1964);
- the misfit is evaluated by comparing the experimental dispersion curve with the theoretical fundamental mode and first two higher modes, to fully exploit the information contained in the experimental data;
- the results are plotted according to the misfit and the interface depth yielding the minimum misfit is chosen.

Figure 2.17a represents the experimental dispersion curve located at x = 0.462 m (Figures 2.10 and 2.11) compared with the theoretical dispersion curves corresponding to the 10 best fitting interface depths while the corresponding V_s profiles are depicted in Figure 2.17b: note that the estimated interface depths are quite close to 0.035 m, which is the expected value for that location.

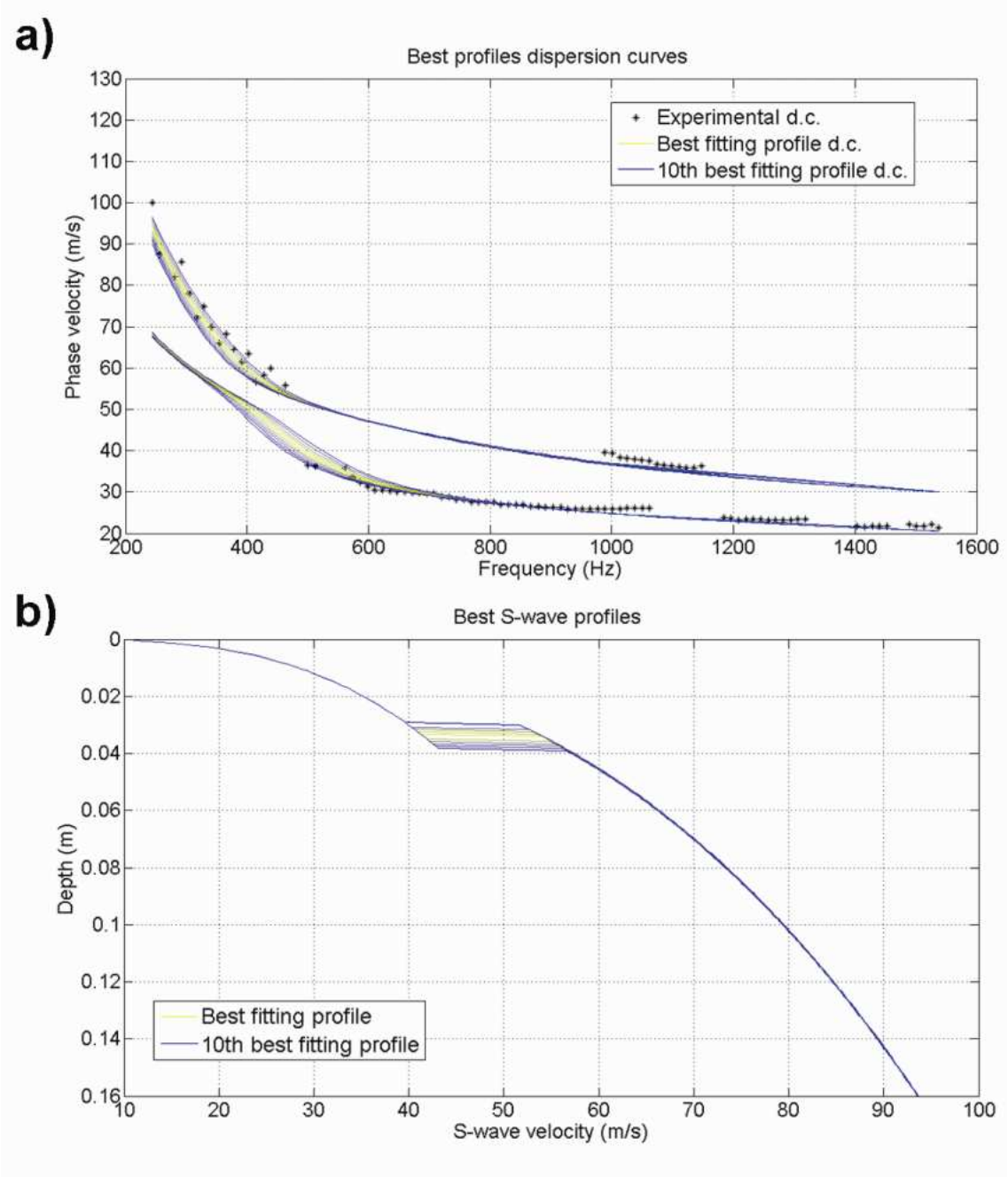

Figure 2.17 – a) Comparison between the experimental dispersion curve at x = 0.462 m and the theoretical dispersion curves corresponding to the best 10 fitting V_s profiles (colour scale ranges from yellow = best profile to blue = 10th best profile). b) best fitting V_s profiles.

Figure 2.18 portrays the 1D V_S profiles that were obtained by combining the values of α_S and γ_S for the two layers and of the interface depths that were retrieved for every inverted dispersion curves: as far as the interface depth estimation is concerned, the agreement with the expected values is good, as the maximum discrepancy between estimated and expected interface does not exceed 1 cm. Indeed, the global result is

satisfactory, as the lateral variation is correctly retrieved and the S-wave velocity behaviour is coherent among all profiles.

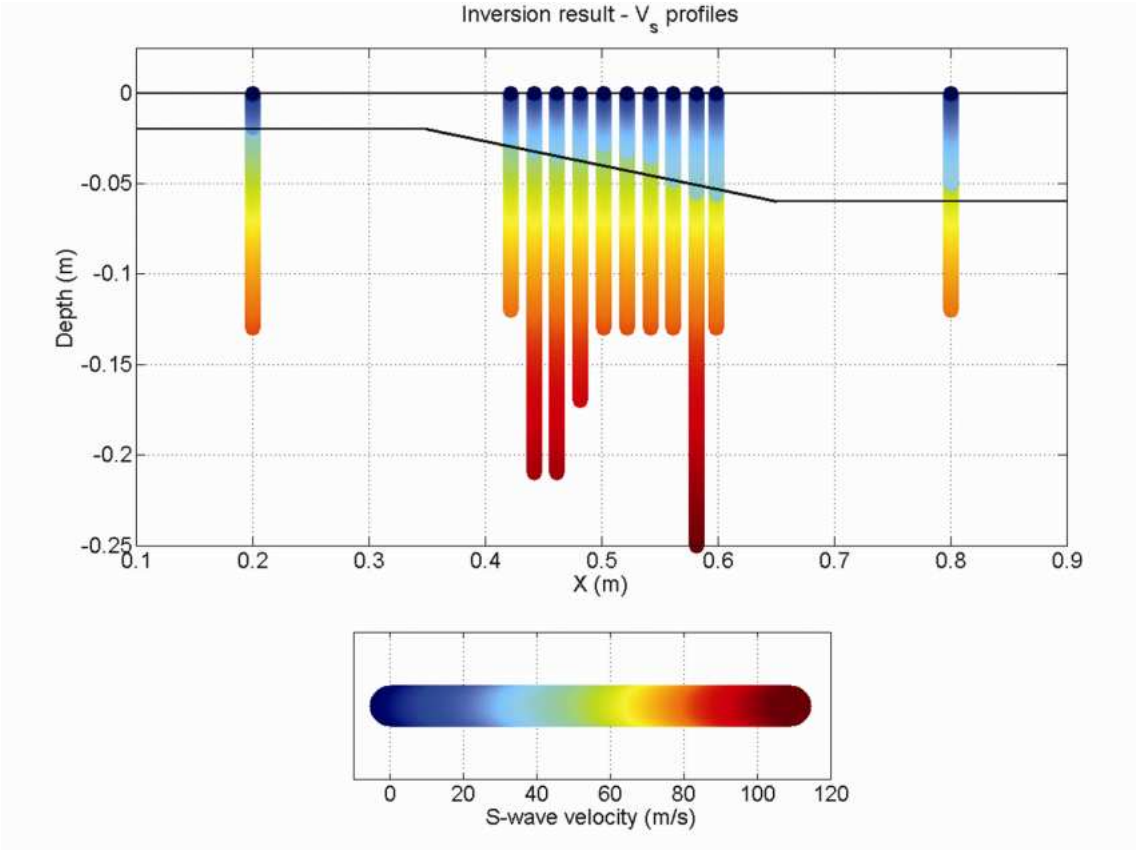

Figure 2.18 – Inversion results. 1D V_s profiles obtained by combining the estimated values of α_S and γ_S for the two layers and the interface depth. V_s profiles are located at the maximum of the Gaussian window used to extract the corresponding dispersion curves

CONCLUSION

Previous studies by Jacob et al., 2008 and by Bodet et al., 2010, 2011 have proven the possibility to retrieve the elastic parameters of granular media through seismic acquisitions performed on physical models with a laser scanner measuring the vertical vibration velocity of the grains on the free surface of the model. These experiments involved single layer models, basically made up of uncompacted grains with a relatively uniform diameter size, depicting a gravity induced stiffness gradient. The main task of our work was to test the feasibility of building granular physical models with a more complex geometry (i.e. constituted by materials with different elastic behaviours and with 2D structures) and to retrieve their characteristics by analyzing the propagation of the surface wave recorded with small-scale "laser-Doppler surveys". The creation of two granular media with different elastic behaviours was achieved through the deposition technique. Once we had evidence of the possibility to create granular materials with different degrees of stiffness, we were able to construct a physical model with two layers whose reciprocal interface is characterized by a uniform slope in the central part of the model itself. By following the purpose of our work, several small-scale seismic acquisitions were performed on the free surface of the model, in order to get a dataset exhaustively depicting surface wave propagation in the model. The last stage of the process involved the extraction of surface wave dispersion curves from the recorded seismograms and their inversion. In particular, in order to get a more accurate description of the 2D portion of the model, an algorithm by Bergamo et al. (2010) based on a spatial windowing of the traces to get several local curves from the same seismogram was applied. As far as the dispersion curves inversion is concerned, we adopted the relationship introduced by Gassmann (1951) where S-wave velocity is considered as power-law dependent on pressure. The unknowns to be retrieved were power-law exponents controlling the V_s behaviour for each layer and the interface depth. Unknown parameters were not estimated by a single inversion process but by means of a step by step inversion procedure, isolating from time to time a parameter or a couple of parameters to be retrieved. Such procedure, although biased by the a priori knowledge of the geometry model, yielded accurate and meaningful results: the 2D structure of the analogue model was satisfactorily reconstructed, and the estimated values of the power-law exponents roughly match the results of previous works by other authors and are coherent with the granular materials deposition process. A further step of the research work would be to attempt an inversion process inverting for all

parameters at the same time, in order to evaluate the possible presence of equivalence phenomena and to test the effectiveness and reliability of a more "blind" inversion procedure.

REFERENCES

Abbis, C. P., 1981. Shear wave measurements of the elasticity of the ground. *Geotechnique*, 31, 91–104.

Bergamo P., Boiero D., Socco L.V. 2010. Retrieving 2D structures from surface wave data by Means of a space-varying spatial windowing. In: EAGE Near Surface 2010, 6-8 September 2010, Zurich, Switzerland.

Bodet, L., Abraham, O., Clorennec, D., 2009. Near-offsets effects on Rayleigh-wave dispersion measurements: Physical modelling. J. Appl. Geophys. 68 (1), pp. 95–103.

Bodet, L., Dhemaied, A., Mourgues, R., Tournat, V., Rejiba, F., 2011. Laser-Doppler acoustic probing of granular media with in-depth property gradient and varying pore pressures. In: International Congress on Ultrasonics (ICU), University of Gdansk, Poland, September 5-8, 2011.

Bodet, L., Jacob, X., Tournat, V., Mourgues, R., Gusev, V., 2010. Elasticity profile of an unconsolidated granular medium inferred from guided waves: Toward acoustic monitoring of analogue models. Tectonophysics 476, pp. 99–104.

Bodet, L., van Wijk, K., Bitri, A., Abraham, O., Côte, P., Grandjean, G., Leparoux, D., 2005. Surface-wave inversion limitations from laser-Doppler physical modeling. J. Env. and Eng. Geophys. 10 (2), pp. 151–162.

Buddensiek, M.-L., 2009. Seismic imaging of sandbox models. Ph.D. thesis, Freien Universitat Berlin.

Campman, X. H., van Wijk, K., Scales, J. A., Herman, G. C., 2005. Imaging and suppressing near-receiver scattered surface waves. Geophysics 70 (2), pp. V21–V29.

Gassmann, F., 1951. Elastic waves through a packing of spheres. Geophysics 16, pp. 673-685.

Graveleau, F., 2008. Interactions tectonique, érosion, sédimentation dans les avant-pays de chaînes : Modélisation analogique et étude des piémonts de l'Est du Tian Shan (Asie centrale). Ph.D. thesis, Université Montpellier II.

Gusev, V., Aleshin, V., Tournat, V., 2006. Acoustic waves in an elastic channel near the free surface of granular media. Phys. Rev. Lett. 96 (214301).

Haskell, N., 1953. The dispersion of surface waves on multilayered media. Bulletin of the Seismological Society of America 43, pp. 17-34.

Haskell, N., 1964. Radiation pattern of surface waves from point sources in a multilayered medium. Bulletin of the Seismological Society of America 54, pp. 377-393.

Hentschel, M. L., Page, N. W., 2007. Elastic properties of powders during compaction. Part 1: Pseudo-isotropic moduli. J. Mater. Sci. 42, pp. 1261–1268.

Jacob, X., Aleshin, V., Tournat, V., Leclaire, P., Lauriks, W., Gusev V. E., 2008. Acoustic probing of the jamming transition in an unconsolidated granular medium. Phys. Rev. Lett. 100, 158003.

Sherlock, D. H., 1999. Seismic imaging of sandbox models. Ph.D. thesis, Curtin University of Technology.

Sherlock, D. H., Evans, B. J., 2001. The development of seismic reflection sandbox modelling. AAPG Bulletin 85, pp. 1645–1659.

Thomson, W.T., 1950. Transmission of elastic waves through a stratified solid medium. Journal of Applied Physics 21, pp. 89-93.

Valverde, J. M., Castellanos, A., 2006. Random loose packing of cohesive granular materials. Europhysics Letters 75 (6), pp. 985–991.

van Wijk, K., Komatitsch, D., Scales, J. A., Tromp, J., 2004. Analysis of strong scattering at the micro-scale, J. Acoust. Soc. Am 115 (3), pp. 1006–1011.

3 – EXPLOITING SCALE PROPERTIES TO RETRIEVE CONSISTENT INITIAL MODELS FOR SURFACE WAVE INVERSION AND TO ESTIMATE SUBSOIL SPATIAL VARIABILITY

In the present chapter I introduce another processing tool I developed to make the surface wave method more reliable in the reconstruction of smooth lateral variations in the subsurface. The algorithm I implemented exploits the scale properties of surface wave: given two dispersion curves, by comparing their "shapes" it is possible to retrieve the ratios between analogous parameters of the two corresponding S-wave velocity profiles, without the need to solve a formal inverse problem. This algorithm is exploited for two different applications: the first one aims at building reliable initial models for the deterministic inversion of a set of dispersion curves, by spreading available local a priori information to all locations where experimental dispersion curves are present. In its second application, the algorithm is used to perform a preliminary assessment of the spatial variability of S-wave velocity model parameters via the comparison of the available experimental dispersion curves.

ABSTRACT

Deterministic inversion of surface wave data suffers from solution non uniqueness and is hence biased by the choice of the initial model. A priori geological information (from log surveys, down-hole tests) can be used to produce a reliable initial model for the inversion of the experimental dispersion curves: this local information, however, is rarely available along all the survey line the dispersion curves are extracted from. We therefore implemented a method to extend a priori local information to the location of the experimental dispersion curves consistently with the available surface wave data. This allows a proper initial model to be generated to make the inversion process more reliable. This method depends on an algorithm which is turn based on a sensitivity analysis and on the application of scale properties of surface waves: given two dispersion curves, by comparing their "shapes" the algorithm estimates the scaling factors between analogous parameters of the two corresponding S-wave velocity profiles, without the need to solve a formal inverse problem. We also addressed the same algorithm to a second application, that is the estimation of the lateral variability of

V_s model parameters based on the analysis of surface wave dispersion data, so that it is possible to preliminary estimate the general trend of V_s model parameters to be later used as a-priori information in the inversion. Once we had stated these novel methodologies, we applied them to two synthetic datasets, derived from models characterized by the presence of 2D structures. We were able to reconstruct such lateral variations by extending a known local V_s profile to the whole subsurface of both models: we also correctly estimated the overall trend of the corresponding V_s model parameters. Eventually, we processed a real dataset: again, we managed to spread the local information provided by two down-hole tests over the seismic line the dispersion curves were extracted from and we also estimated the spatial variability of the pseudo-2D section model parameters. In both cases, the results we got are in good agreement with other geophysical analyses performed on the same site and confirm the applicability and reliability of our methods.

INTRODUCTION

Surface wave (SW) analysis is nowadays regarded as a powerful tool for the estimation of vertical 1D S-wave profile in the subsurface. SW analysis involves the extraction of an experimental dispersion curve from active or passive seismic measurements and its inversion to estimate the vertical profile of S-wave velocity (V_s) distribution. Nevertheless, the main drawback of SW method is that the inversion suffers from solution non-uniqueness (Tarantola 2005 and Foti et al. 2009): in other words, several theoretical dispersion curves relevant to as many V_s profiles fit equally well the experimental curve. Literature offers some strategies to handle this issue. If a global search inversion algorithm is chosen, it is possible to single out which subsoil models have a similar level of consistency with the data. However, global search methods (GSMs) have greater computational costs when compared to deterministic inversion methods (Socco et al. 2010). To reduce such costs, some optimization methods have been developed, such as simulated annealing (based on the work by Metropolis et al. 1953), genetic algorithms, or the application of scale properties of surface wave (Socco and Boiero 2008). If a deterministic inversion algorithm is preferred, great care must be paid in selecting the model parameterization and the initial model, as the non-uniqueness of the solution makes the inversion result very sensitive to them, and they can drive the inversion towards local minima if they have not been

properly chosen (Sambridge, 2001; Luke et al., 2003; Wathelet, 2005). The effects of this criticism can be mitigated by exploiting a priori information from borehole logs and/or other geophysical data available for the investigated site. Moreover, constrained or joint inversion algorithms, by combining different kinds of geophysical data or integrating the inversion of neighbouring datasets, can improve the consistency of the inversion result and the reliability of its physical meaning (see for instance Wisén and Christiansen 2005, for a joint inversion of surface wave and resistivity data, and Forbriger 2003 for a joint analysis of refraction and surface wave data). Although the improvement induced by joint and constrained inversion algorithms has been shown by several papers, the common practice in surface wave analysis is that when other data are available at the site they are simply used for a posteriori comparison of the results. In geotechnical engineering, in particular, when borehole tests are available, they are frequently combined with surface-wave seismic surveys: in fact, downhole or crosshole tests results are generally viewed as more reliable when compared to surface-wave analysis based V_s profiles and usually, the agreement between the two results is used to prove the reliability of the latter (Malovichko et al. 2005). Therefore, a priori information is not fully exploited in a rigorous and quantitative way.

The present work faces the issue of the solution non-uniqueness of surface wave data by proposing a procedure (Boiero et al. 2009) able to quantitatively integrate a priori local information into the inversion of surface wave dispersion curves gathered in neighbouring sites by extracting available punctual data from log surveys and adapting them according to the observed surface wave dispersive behaviour. This goal is achieved by applying an approach based on a sensitivity analysis followed by the exploitation of the scale properties of surface waves. Scale properties of surface wave have been introduced by Socco and Strobbia (2004), applied to Monte Carlo inversion by Socco and Boiero (2008) and inserted in the perspective of full-waveform inversion by Maraschini et al. (2011). They are based on the non-dimensionalization of the related forward modelling, so that if seismic parameters of two different models differ only for scale factors, the two corresponding dispersion curves can be derived one from the other by applying a proper scaling. As already proposed by Socco and Boiero (2008), in the procedure presented in this paper we exploit surface waves scale properties to derive the scale factors between seismic parameters of different models from the comparison of the shape of the corresponding dispersion curves. In our case, however, every seismic parameter can scale separately from the other ones, so that a sensitivity analysis is

necessary to separate the contribution of every single model parameter on the dispersion curves scaling.

We used a similar approach, based on the same principles (sensitivity analysis, exploitation of scale properties of surface waves), to face another issue related to the application of the surface wave method, that is the reconstruction of 2D structures in the subsurface. The surface wave (SW) method is in fact characterized by a monodimensional approach and might therefore prove unsuitable when applied in 2D environments (Semblat et al. 2005). Some recent papers propose strategies to reconstruct lateral variations from surface wave dispersion analysis: they are mainly based on a moving spatial window to extract a set of neighbouring local dispersion curves, which are later separately inverted (see Tian et al., 2003; Bohlen et al., 2004; Neducza 2007). Grandjean and Bitri (2006) and Socco et al. (2009) exploit the data redundancy proper of reflection seismic recordings by stacking in the *f-k* domain different records referenced to the same spatial location: again, the dataset to be inverted is an ensemble of dispersion curves located along the acquisition line. In this work, we introduce a method to estimate the lateral variability of model parameters of a 2D pseudosection of S-wave velocity in the subsoil based on the analysis of surface wave dispersion data. The method exploits the same approach presented above, which allows computing the scaling factors between corresponding parameters of two V_s models via the comparison of the two related dispersion curves and the application of scale properties of surface waves (Socco and Boiero, 2008). The retrieved information on the spatial variability of model parameters can be effectively used to single out areas with greater or lower lateral variability, for a proper choice of the inversion algorithm (constrained or unconstrained). In particular, if a laterally constrained algorithm (LCI; Auken and Christiansen, 2004) is preferred, the estimated lateral variability can be effectively exploited for a data-consistent tuning of the lateral constraints.

The two novel methodologies (building a consistent initial model and estimating the spatial variability of model parameters) and the algorithm both are based on are thoroughly described in the following section: we then present their application to two synthetic datasets and, finally, to a real case.

METHODS

In this section, we first illustrate the algorithm the two procedures presented in this work are based on and later we will show how it can be applied for the build-up of a consistent initial model based on a-priori local information and for the estimation of the expected lateral variability of V_s model parameters.

Comparison between two dispersion curves

The key point of our work is a method to retrieve the ratios between corresponding parameters of two 1D V_s profiles by comparing the two corresponding dispersion curves: therefore, if one of the two V_s profiles is known, the other one can be estimated (Figure 3.1).

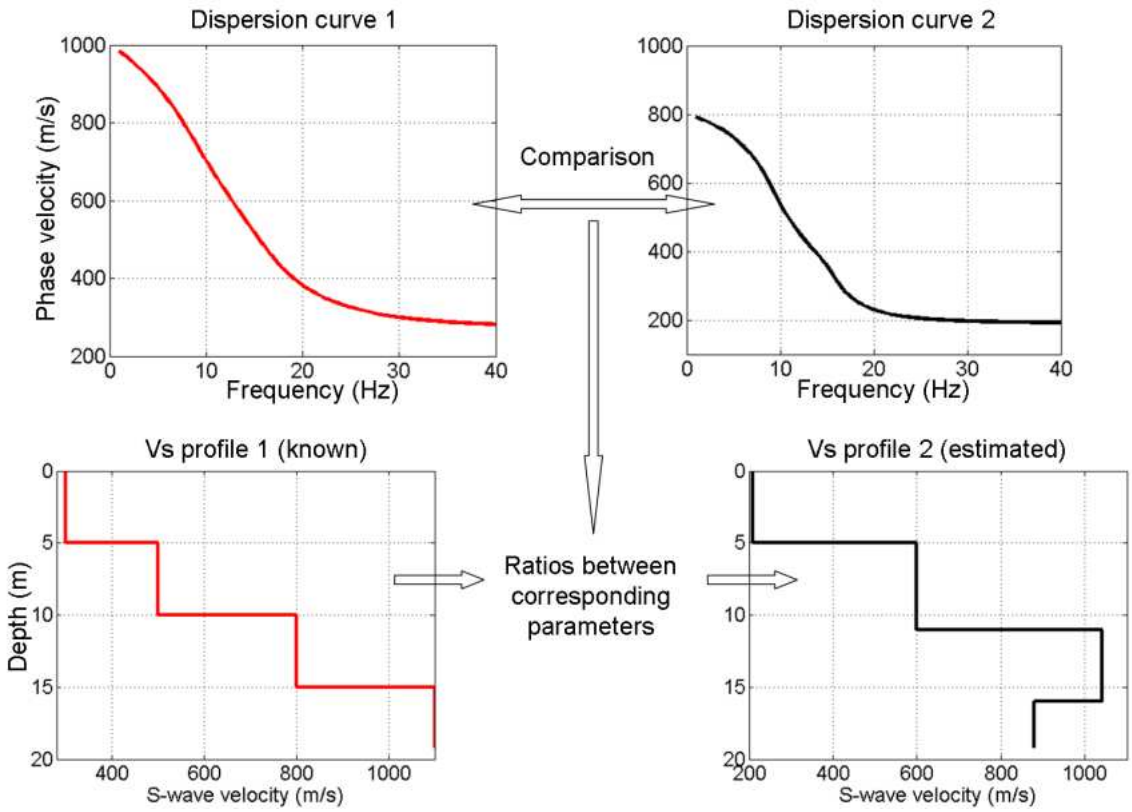

Figure 3.1 – Sketch of the comparison between two dispersion curves: V_s profile 1 is known, the corresponding dispersion curve (dispersion curve 1) and the dispersion curve related to the unknown V_s profile 2 are available. The ratios between analogous parameters of the V_s profiles are obtained from the comparison of the two dispersion curves so that V_s profile 2 can be estimated.

Such comparison method requires that the two 1D subsoil profiles refer to horizontally layered media that have the same number of layers. Moreover, we assume the densities and the Poisson's ratios of corresponding layers of the two subsoil profiles to be equal, i.e. they don't scale, as they have a limited influence on the dispersion of surface waves (Nazarian, 1984). The model parameters whose scaling factors are estimated are therefore the layers thicknesses and S-wave velocities.

The comparison method is based on a sensitivity analysis and on the application of the scale properties.

A general description of scale properties of seismic waveform has been presented by Maraschini et al. 2011. Scale properties of surface wave dispersion curves were enunciated in the work by Socco and Strobbia (2004) and formally demonstrated and applied by Socco and Boiero (2008). They can be summarized in the statement that "the phase velocities and the frequencies of the dispersion curve scale simply if all the layer velocities are scaled; the frequencies of the dispersion curve scale if all the layer thicknesses are scaled" (Socco and Strobbia, 2004). In other words, given a layered subsoil model $\mathbf{M}(\mathbf{h},\mathbf{v_s},\boldsymbol{\nu},\boldsymbol{\rho})$ where $\mathbf{h}$, $\mathbf{v_s}$, $\boldsymbol{\nu}$ and $\boldsymbol{\rho}$ represent the vectors of the layers thicknesses, S-wave velocities, Poisson's ratios and densities respectively, and given its corresponding dispersion curve whose points coordinates in the frequency-phase velocity space are described by the frequencies vector $\mathbf{f}$ and by the phase velocities vector $\mathbf{v}$, the dispersion curve related to the scaled model $\mathbf{M}'(\beta\cdot\mathbf{h},\gamma\cdot\mathbf{v_s},\boldsymbol{\nu},\boldsymbol{\rho})$, where β and γ are the scaling factors for thicknesses and S-wave velocities, can be derived from model $\mathbf{M}$ dispersion curve, as

$$\mathbf{v}' = \gamma\cdot\mathbf{v}\,;\ \mathbf{f}' = \frac{\gamma}{\beta}\cdot\mathbf{f} \qquad (1)$$

where $\mathbf{v}'$ and $\mathbf{f}'$ are the vectors of phase velocities and frequencies of the dispersion curve related to model $\mathbf{M}'$. Consequently, if dispersion curves are represented on a bi-logarithmic axis plot, the application of the scaling factors of model parameters implies a rigid translation of the modal curves (Figure 3.2). Equation 1 for the dispersion curves represented in frequency-wavenumber domain becomes:

$$\mathbf{f}' = \frac{\gamma}{\beta}\cdot\mathbf{f};\mathbf{k}' = {}^{1}\!/_{\beta}\,\mathbf{k} \qquad (2)$$

where $\mathbf{k}$ and $\mathbf{k}'$ represent the vectors of the wavenumbers of the points of the dispersions curves related to model $\mathbf{M}$ and $\mathbf{M}'$ respectively.

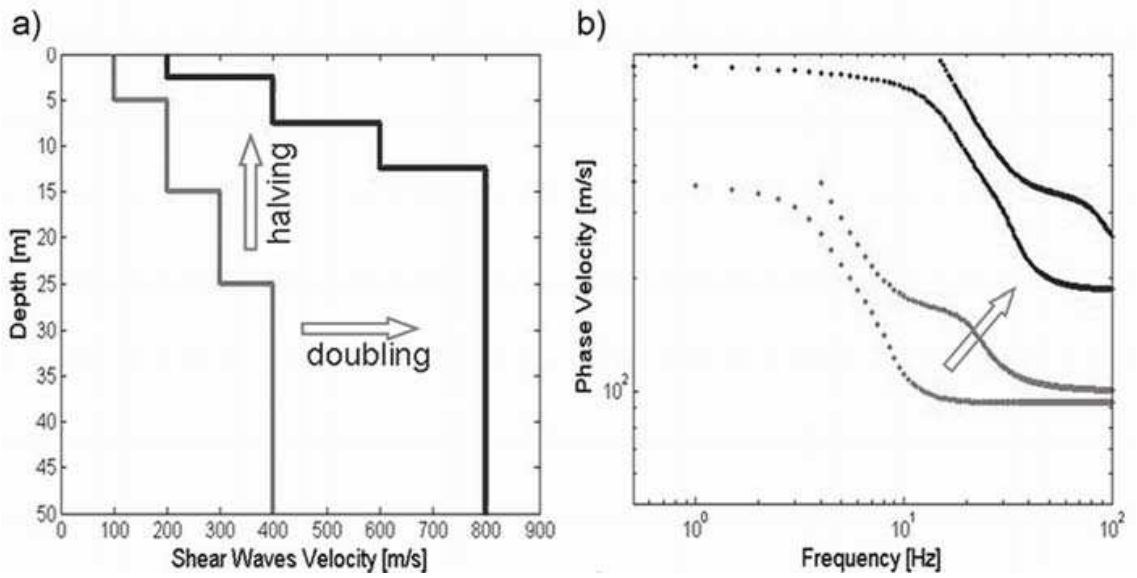

Figure 3.2 – Example of scaling properties of modal curves: in a bi-logarithmic axis plot (b), the scaling of frequencies and velocities according to the scaling of model parameters (a) produces a rigid translation of the modal curves (from Socco and Boiero 2008).

In our case we have to extend this concept to the case in which different model parameters are scaled differently and our aim is to estimate the scale factor for each model parameter. To do this, prior to the application of scale properties, we perform a sensitivity analysis, in order to estimate the contribution of every single model parameter to the overall scaling of the dispersion curve.

Sensitivity analysis

The task of the sensitivity analysis is to understand how much the dispersion curve points are sensitive to each parameter of the layered V_s profile, i.e. how much their phase velocity and frequency values change if one model parameter (either a layer thickness or a S-wave velocity) is perturbed. Here's the list of the steps explaining how the sensitivity analysis needs to be computed to be consistent with the application of the scale properties:

- a for loop is run over the V_s model parameters (layers thicknesses and S-wave velocities): at every iteration, the j^{th} parameter p_j is chosen;
- parameter p_j is successively increased and then decreased by a relative quantity α:

$$p_j^+ = (1+\alpha)p_j ; p_j^- = (1-\alpha)p_j \quad (3)$$

where p_j^+ and p_j^- correspond to parameter p_j increased and decreased and α is the perturbation relative quantity (we have generally set $\alpha = 0.05$);

- consequently, two V_s profiles (V_{sj}^+ and V_{sj}^-) are created, similar to the original V_s model but where the value of p_j is substituted by p_j^+ and p_j^- respectively;
- theoretical dispersion curves dc_j^+ and dc_j^- corresponding to V_s models V_{sj}^+ and V_{sj}^- are computed by applying a Haskell and Thomson forward modelling (Haskell 1953, Thomson 1950): in both cases the fundamental mode only is computed;

  if parameter p_j is a layer thickness, its sensitivity $\mathbf{s}_j$ is estimated by evaluating how the frequencies of the theoretical dispersion curves scale, phase velocities being equal (Figure 3.3), because a scaling of the thicknesses produces a scaling of the frequencies only (equation 1). Sensitivity is computed by applying the following equations:

$$\mathbf{s}_j^+ = \log\left(\mathbf{f}_j^+ / \mathbf{f}\right) \Big/ \log\left(p_j^+ / p_j\right); \mathbf{s}_j^- = \log\left(\mathbf{f}_j^- / \mathbf{f}\right) \Big/ \log\left(p_j^- / p_j\right)$$
$$\mathbf{s}_j = \left(\mathbf{s}_j^+ + \mathbf{s}_j^-\right)/2 \qquad (4)$$

where $\mathbf{s}_j^+$ and $\mathbf{s}_j^-$ are the vectors storing the scaling of the frequencies with respect to an increase and to a decrease of parameter p_j, $\mathbf{f}$ are the frequencies of the points of dispersion curves dc_j^+ and dc_j^- at the same phase velocities of $\mathbf{f}$. On the other hand, if parameter p_j is a layer S-wave velocity, the original dispersion curve, dc_j^+ and dc_j^- are turned from phase-velocity versus frequency domain into frequency-wavenumber domain because a scaling of the velocities produces a scaling of frequencies alone in *f-k* domain (equation 2). The sensitivity is then computed by evaluating how the frequencies of the theoretical dispersion curves scale, wavenumbers being equal (Figure 3.4). Again, equations 4 are used for the computation of the sensitivity, but now $\mathbf{f}$ represents the frequencies of the points of the original dispersion curves and $\mathbf{f}_j^+$ and $\mathbf{f}_j^-$ are the frequencies of the points of dispersion curves dc_j^+ and dc_j^- at the same wavenumbers of $\mathbf{f}$.

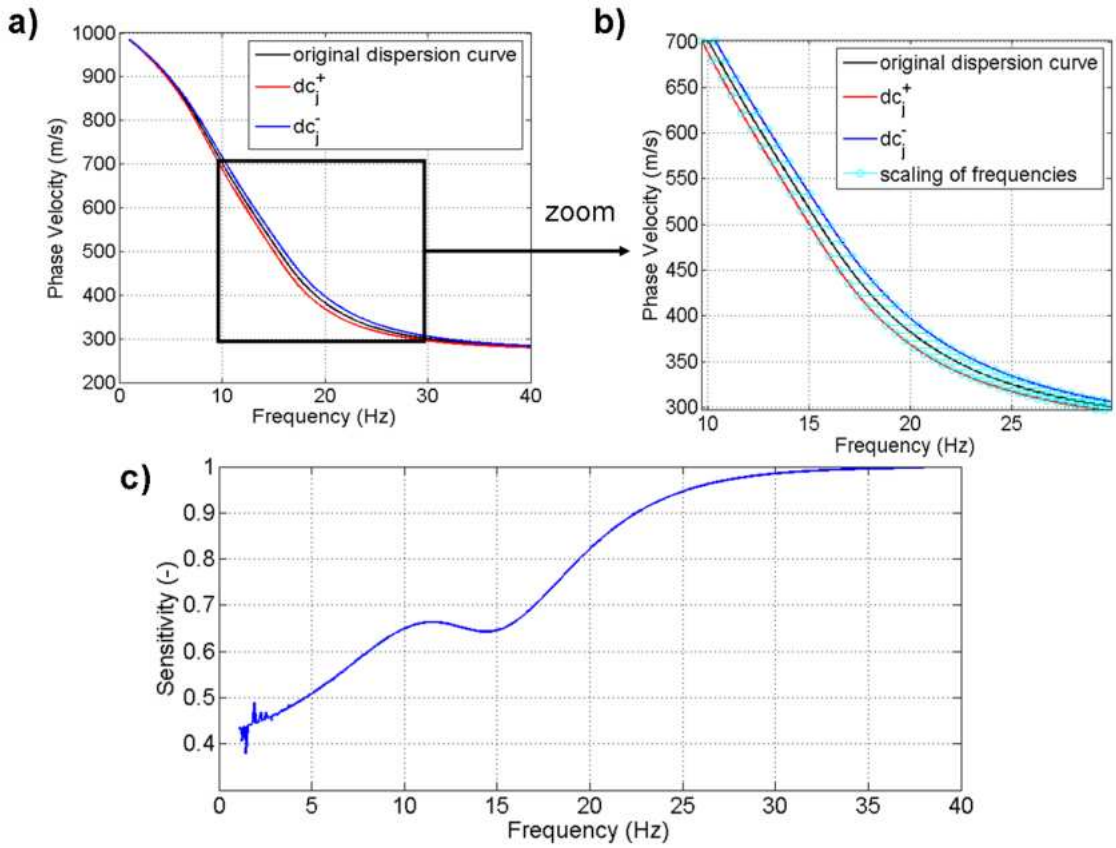

Figure 3.3 – Example of computation of the sensitivities: sensitivity for the 1st layer thickness of V_s profile 1 from Figure 1. a) original dispersion curve (black line) and dispersion curves corresponding to the two V_s profiles where the 1st layer thickness has been increased and decreased (dc_j^+ and dc_j^-, blue line and red line); b) zoom of the previous plot highlighting the scaling of frequencies; c) sensitivity for the 1st layer thickness.

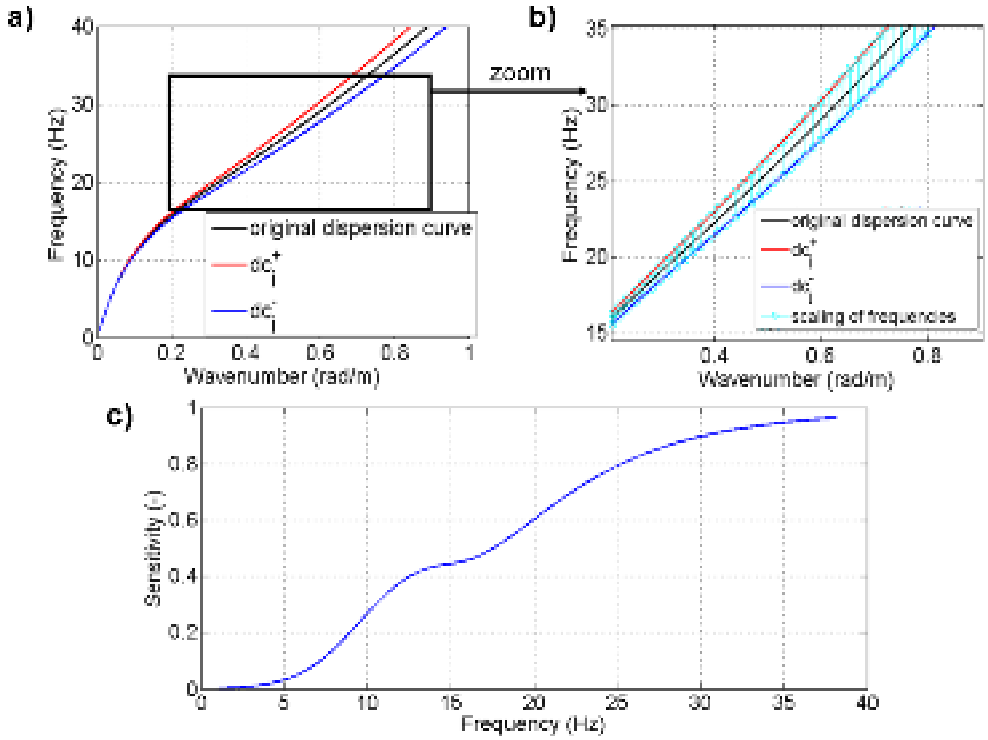

Figure 3.4 – Example of computation of the sensitivities: sensitivity for the 1st layer S-wave velocity of V_s profile 1 from Figure 3.1. a) original dispersion curve (black line) and dispersion curves corresponding to the two V_s profiles where the 1st layer velocity has been increased and decreased (dc_j^+ and dc_j^-, blue line and red line); b) zoom of the previous plot highlighting the scaling of frequencies; c) sensitivity for the 1st layer S-wave velocity.

Figure 3.5 represents the sensitivities computed for the parameters of *Vs* model 1 represented in Figure 3.1: not surprisingly, parameters of shallower layers have a greater influence at high frequencies, while parameters of deeper layers have higher sensitivity values at low frequencies.

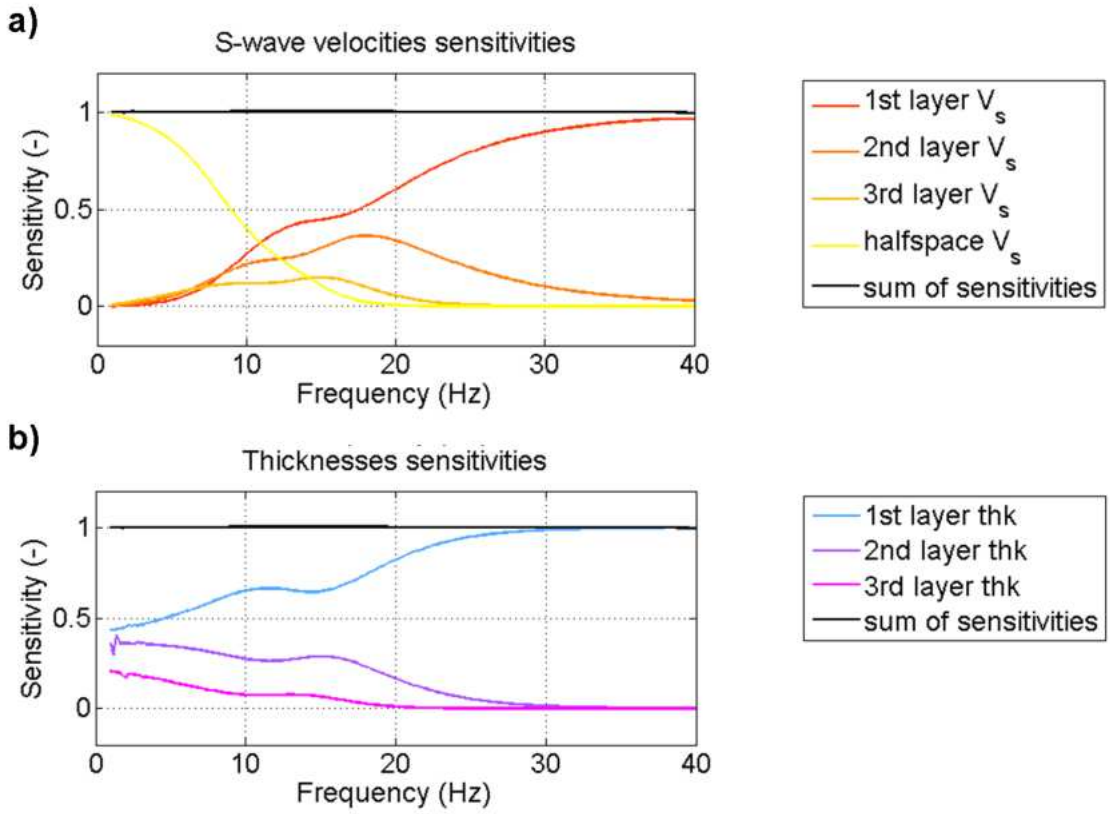

Figure 3.5 – Sensitivities for the parameters of V_s model 1 from Figure 3.1. a) sensitivities relevant to layers S-wave velocities, indicating how much phase velocity and frequency values of the points of the corresponding dispersion curve change with respect to a scaling of the S-wave velocities. b) sensitivities relevant to layers thicknesses, indicating how much phase velocity and frequency values of the points of the corresponding dispersion curve change with respect to a scaling of the S-wave velocities. In both plots sensitivities are here represented as a function of the frequency of the dispersion curve points, and black lines indicate the sum of the sensitivities for each dispersion curve point.

It is worth noting that the sum of the thickness sensitivities and the sum of the velocity sensitivities carried out for every frequency is one (black lines in Figure 3.5): in fact, the scaling in frequency and phase velocity of every point of the dispersion curve can be explained as the result of a weighted sum of the scaling of the V_s model parameters, where the weights correspond to the parameter sensitivities at the same frequency of the point itself.

Application of scale properties

We have shown that given two subsoil V_s models **M** and **M**' with the same number of layers whose thicknesses and S-wave velocities are homogeneously scaled, it is possible to derive the dispersion curve related to **M**' from the dispersion curve corresponding to **M** by properly scaling the frequencies and phase velocities of the known dispersion curve according to the scaling of the model parameters (equations 1 and 2). However, for the purposes of our work, we need to retrieve the scale factors for each V_s model parameter if not all layers thicknesses and not all layers S-wave velocities are scaled the same. To do this, we consider the scaling of the frequencies and phase velocities of the dispersion curve as the weighted sum of the effects of the scaling of the different model parameters, where the weights are provided by the sensitivity analysis. In other words, sensitivities are computed to know how much frequencies and phase velocities of the modal curve scale if one single parameter is scaled at a time: once sensitivities are known, they are used as weights for the application of the superposition principle. To specify the previous statements, we reconsider the scale properties (equations 1 and 2). A subsoil layered model $\mathbf{M(h,v_s,v,\rho)}$ is given, where **h**, $\mathbf{v_s}$, **v** and **ρ** refer to the vectors of the layers thicknesses, S-wave velocities, Poisson's ratios and densities respectively: its corresponding dispersion curve is constituted by *n* points whose frequencies and phase velocities are stored in vectors **f** and **v** respectively. The sensitivities of the dispersion curve points with respect to the scaling of the *m+1* layers S-wave velocities are computed as shown in the previous paragraph and can be stored in matrix $\mathbf{S_v}$:

$$\mathbf{S}_{\mathrm{v}} = \begin{bmatrix} s_{1,1} & \dots & s_{1,m+1} \\ \dots & \dots & \dots \\ s_{n,1} & \dots & s_{n,m+1} \end{bmatrix} \qquad (5)$$

whose generic element $s_{i,j}$ represents the sensitivity of the i^{th} point of the dispersion curve with respect to the j^{th} layer S-wave velocity. Similarly, the sensitivities with respect to the *m* thicknesses are stored in $\mathbf{S_h}$ matrix:

$$\mathbf{S}_{\mathrm{h}} = \begin{bmatrix} s_{1,1} & \dots & s_{1,m} \\ \dots & \dots & \dots \\ s_{n,1} & \dots & s_{n,m} \end{bmatrix} \qquad (6)$$

whose generic element $s_{i,j}$ represents the sensitivity of the i^{th} point of the dispersion curve with respect to the j^{th} layer thickness.

The dispersion curve related to model $\mathbf{M'(B \cdot h, \Gamma \cdot v_s, \nu, \rho)}$, where $\mathbf{B}$ and $\mathbf{\Gamma}$ are diagonal matrices whose main diagonal entries are the scaling factors for thicknesses and S-wave velocities respectively, can be derived from the curve corresponding to model $\mathbf{M(h, v_s, \nu, \rho)}$ by applying the superposition principle; the scaling of phase velocities is computed as follows:

$$\log(\mathbf{v'}) - \log(\mathbf{v}) = \mathbf{S}_v \cdot [\log(\mathrm{diag}(\mathbf{\Gamma}))] \quad (7)$$

and therefore

$$\mathbf{v'} = \mathbf{v} \cdot \exp\{\mathbf{S}_v \cdot [\log(\mathrm{diag}(\mathbf{\Gamma}))]\} \quad (8)$$

where $\mathbf{v'}$ is the vector of the phase velocities of the points of the dispersion curve corresponding to model $\mathbf{M'(B \cdot h, \Gamma \cdot v_s, \nu, \rho)}$.

The scaling of the frequencies can be estimated in a similar way:

$$\log(\mathbf{f'}) - \log(\mathbf{f}) = \mathbf{S}_v \cdot [\log(\mathrm{diag}(\mathbf{\Gamma}))] - \mathbf{S}_h \cdot [\log(\mathrm{diag}(\mathbf{B}))] \quad (9)$$

which can be rewritten as

$$\mathbf{f'} = \mathbf{f} \cdot \exp\{\mathbf{S}_v \cdot [\log(\mathrm{diag}(\mathbf{\Gamma}))] - \mathbf{S}_h \cdot [\log(\mathrm{diag}(\mathbf{B}))]\} \quad (10)$$

with $\mathbf{f'}$ the vector of the frequencies of the points of the dispersion curve corresponding to model $\mathbf{M'(B \cdot h, \Gamma \cdot v_s, \nu, \rho)}$.

As the scaling of frequencies and phase velocities is substantially evaluated by solving a system of linear equations (equations 8 and 10), it is then possible to solve the inverse problem as well, i.e. estimating the scaling factors of model parameters being known the scaling of frequencies and phase velocities. In other words, it is possible to estimate $\mathbf{B}$ and $\mathbf{\Gamma}$, and therefore the parameters of model $\mathbf{M'(B \cdot h, \Gamma \cdot v_s, \nu, \rho)}$ being given model $\mathbf{M(h, v_s, \nu, \rho)}$ and the two corresponding dispersion curves, defined by vectors $\mathbf{v}$, $\mathbf{f}$ and $\mathbf{v'}$, $\mathbf{f'}$. As both dispersion curves are known, it is possible to evaluate how frequencies and phase velocities of dispersion curve of model $\mathbf{M}$ need to be scaled to match the shape of dispersion curve of model $\mathbf{M'}$. However, this match cannot be interpreted uniquely, as there are infinite combinations of scaling able to make the curve of model $\mathbf{M}$ to assume the shape of the curve of model $\mathbf{M'}$: therefore it is necessary to assume that either only layers thicknesses or only layers S-wave velocities can vary, so that either the scaling of frequencies alone in the *f-v* plane or the scaling of frequencies alone in the *f-k* plane is evaluated. In both cases, the measured scaling vector can be referred to as $\mathbf{f'}/\mathbf{f}$, i.e. the vector of the ratios between frequency values of the curve of model $\mathbf{M'}$ and the frequency values of the curve of model $\mathbf{M}$, being either phase velocities or wavenumbers constant.

If the thicknesses are assumed to be constant and only S-wave velocities can vary, equation 9 can be rewritten as:

$$\log(\mathrm{diag}(\boldsymbol{\Gamma})) = \mathbf{S}_v^{-g} \cdot [\log(\mathbf{f}') - \log(\mathbf{f})] \quad (11)$$

and therefore

$$\mathrm{diag}(\boldsymbol{\Gamma}) = \exp\left\{\mathbf{S}_v^{-g} \cdot [\log(\mathbf{f}') - \log(\mathbf{f})]\right\} \quad (12)$$

where $\boldsymbol{\Gamma}$ is the diagonal matrix whose main diagonal entries are the ratios between corresponding S-wave velocities of model **M** and model **M'** and $\mathbf{S}_v^{-g}$ is the generalized inverse of sensitivity matrix $\mathbf{S}_v$ (see equation 5). $\mathbf{S}_v^{-g}$ is defined as

$$\mathbf{S}_v^{-g} = \left(\mathbf{S}_v^T \mathbf{S}_v\right)^{-1} \mathbf{S}_v \quad (13)$$

Note that the linear system of equations in 12 has one and valid solution and $\mathbf{S}_v^{-g}$ can be defined as in equation 13 if the number of elements of vector $\mathbf{f}'/\mathbf{f}$ is greater than the number of unknowns, which is equal to the number of layers in the models.

Similarly, if S-wave velocities are assumed to be equal in both models, the ratios between corresponding thicknesses of model **M'** and model **M** (the elements of the main diagonal of matrix **B**) can be obtained by rewriting equation 9 as

$$\log(\mathrm{diag}(\mathbf{B})) = -\mathbf{S}_h^{-g} \cdot [\log(\mathbf{f}') - \log(\mathbf{f})] \quad (14)$$

and therefore

$$\mathrm{diag}(\mathbf{B}) = \exp\left\{-\mathbf{S}_h^{-g} \cdot [\log(\mathbf{f}') - \log(\mathbf{f})]\right\} \quad (15)$$

where $\mathbf{S}_h^{-g}$ is the generalized inverse of sensitivity matrix $\mathbf{S}_h$ (see equation 6) and it is defined as: $\mathbf{S}_h^{-g} = \left(\mathbf{S}_h^T \mathbf{S}_h\right)^{-1} \mathbf{S}_h$ (16)

Two examples of the application aforementioned method are presented in Figures 3.6 and 3.7: in Figure 3.6 S-wave thicknesses are assumed constant, while in Figure 3.7 velocities are the same in both models.

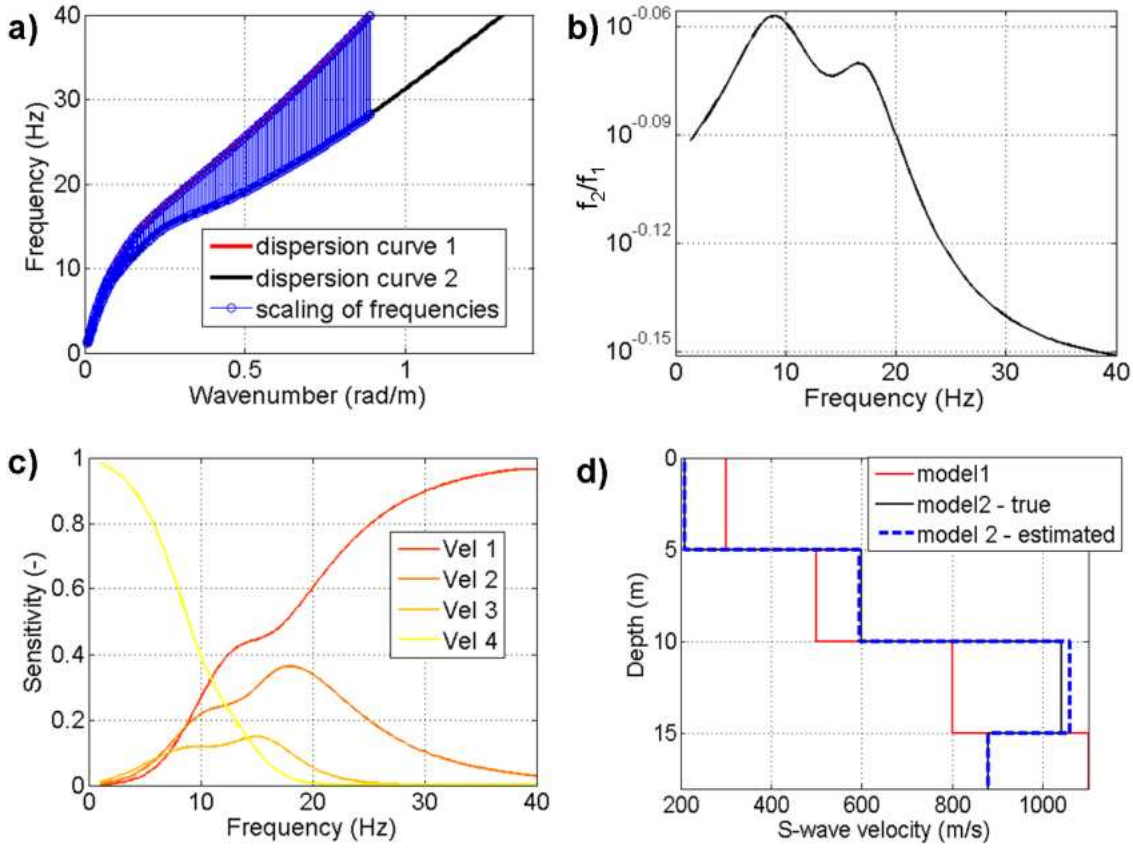

Figure 3.6 – Example of the application of the method exploiting the comparison between two dispersion curves to retrieve the ratios between corresponding parameters of both models. In this case, thicknesses are constant and only S-wave velocities can vary. a) The two dispersion curves, represented in a f-k plot, and the evaluation of the scaling of frequencies for the dispersion curve 1 (whose corresponding model is known) to match dispersion curve 2; b) the estimated scaling of frequencies; c) sensitivities of dispersion curve 1 computed with respect to the S-wave velocities of model 1; d) subsoil models: model 1 is given, model 2 is estimated and compared with its true V_s profile.

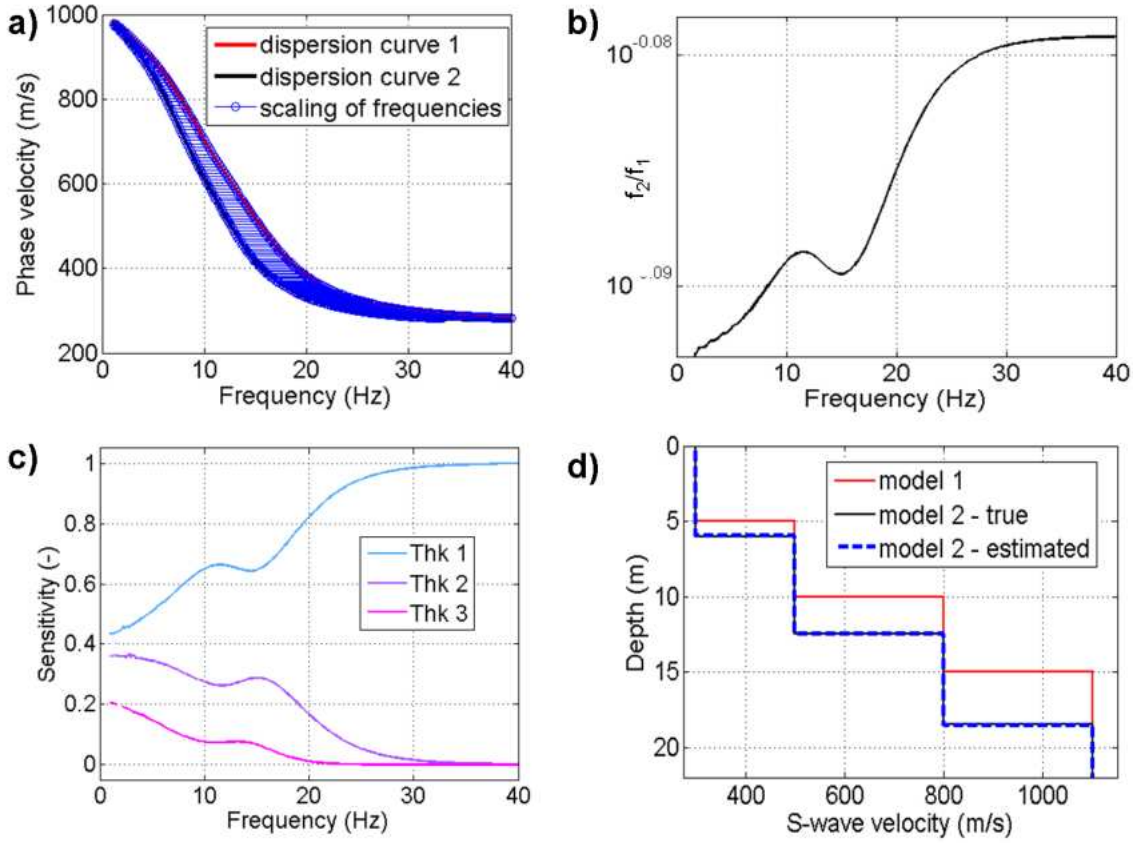

Figure 3.7 – Example of the application of the method exploiting the comparison between two dispersion curve to retrieve the ratios between corresponding parameters of both models. In this case, S-wave velocities do not vary and only thicknesses can change their value. a) The two dispersion curves, represented in a f-v plot, and the evaluation of the scaling of frequencies for the dispersion curve 1 (whose corresponding model is known) to match dispersion curve 2; b) the estimated scaling of frequencies; c) sensitivities of dispersion curve 1 computed with respect to the thicknesses of model 1; d) subsoil models: model 1 is given, model 2 is estimated and compared with its true V_s profile.

In both cases the unknown model is correctly estimated starting from the knowledge of the other model and having the two dispersion curves.

The main limitation of the presented approach is that it can be reliably applied if the scaling factors of model parameters, stored in the main diagonal of matrices **B** and **Γ**, are not too far from $1 \pm \alpha$, where α is the parameter perturbation relative quantity introduced in the sensitivity computation (see previous section): if this condition does not hold true, the approximation introduced by linearizing the problem (see equations 7 and 9) may not be valid anymore. From several numerical tests, we have concluded that the presented method can be reliably applied if the following inequalities:

$$0.1 \le \frac{\left|\mathrm{diag}(\mathbf{B}) - 1\right|}{\alpha} \le 10 \;;\; 0.1 \le \frac{\left|\mathrm{diag}(\boldsymbol{\Gamma}) - 1\right|}{\alpha} \le 10 \quad (15)$$

hold true for all the elements of the main diagonal of **B** and **Γ**.

Figure 3.8 displays a flow-chart of the presented method, by which it is possible to estimate the scaling factors between the parameters of two V_s models via the comparison of the corresponding dispersion curves.

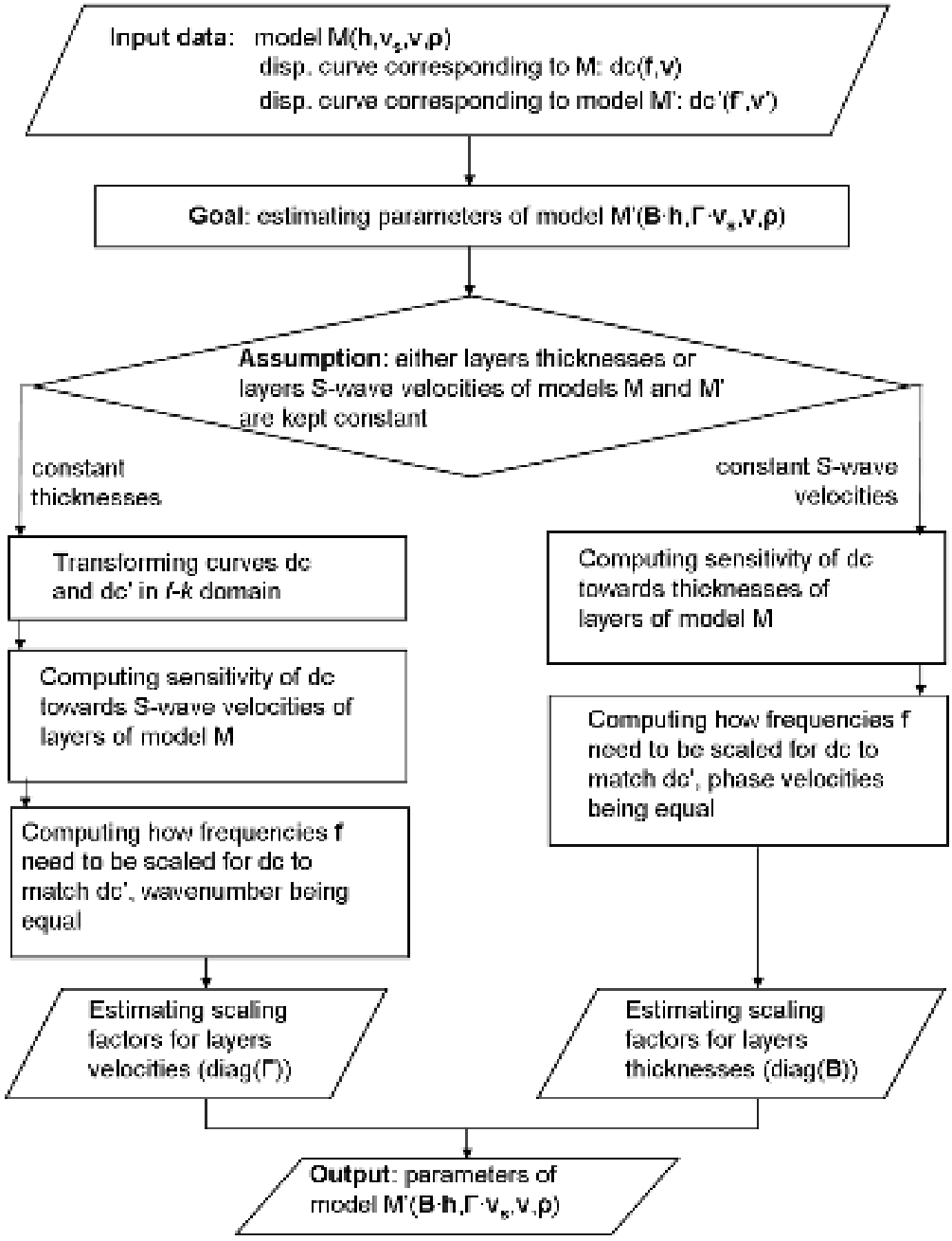

*Figure 3.8 – Flowchart of the method by which it is possible to estimate the scaling factors between the parameters of two V_s models (**M** and **M'**) via the comparison of the corresponding dispersion curves (indicated as dc and dc').*

Production of consistent initial model

The goal of our procedure is to use the a-priori information that may be available at a position in the neighbouring of the seismic line to build up a consistent initial model also for dispersion curves which are not close to the a-priori information location. This is achieved by updating the V_s model provided by the a-priori information available at one place to the location of the dispersion curve in a way which is consistent with the dispersion curve itself. The scaling factors for the model parameter update are retrieved by means of the comparison method presented in the previous paragraph.

The first step is to compute the theoretical dispersion curve relative to the V_s model that represents the a-priori information, usually derived from a down-hole or cross-hole test results. The curve is then used for the sensitivity analysis that supplies the weights for the application of the scale properties. Eventually, the available experimental dispersion curves are compared one by one to the theoretical curve through the application of scale properties of surface waves: this provides the update of the a-priori model at each experimental dispersion curve position (Figure 3.9). The obtained models are based on the parameterization obtained from the a-priori information and are modified according to the local information contained in the dispersion curve: they are hence consistent with both a-priori information and raw data. They can be hence used as consistent initial model for inversion.

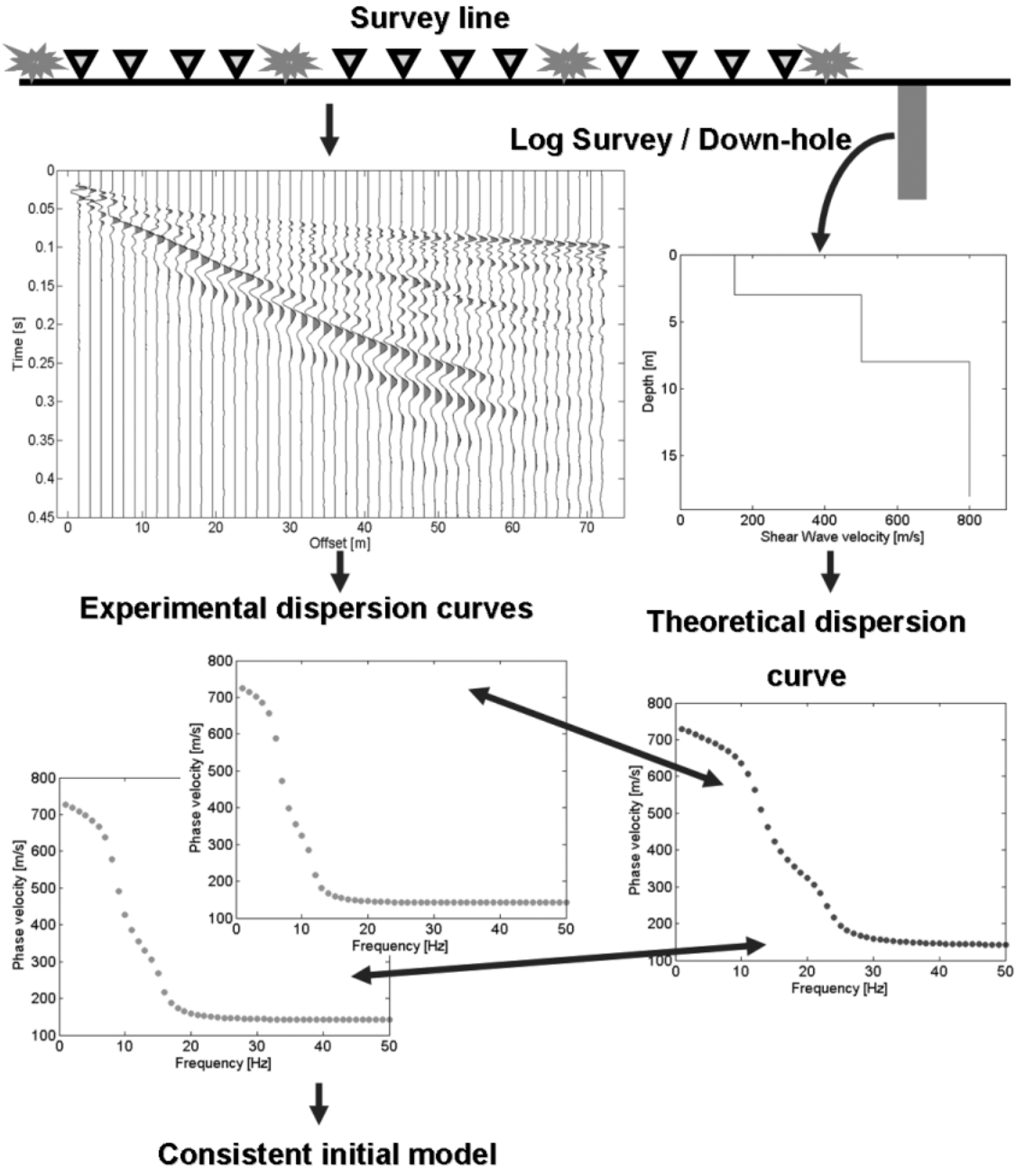

Figure 3.9 – Scheme of the procedure to estimate a consistent initial model for the inversion of a set of experimental dispersion curves. Experimental dispersion curves are compared with the theoretical curve corresponding the V_s profile retrieved from log survey or a down-hole test. The result of each comparison is a 1D V_s profile corresponding to the a priori information properly customized according to the considered experimental dispersion curve.

Estimation of expected lateral variability

The input data that is required for the estimation of the expected lateral variability of V_s model parameters is a set of dispersion curves spatially located at different positions along the seismic line they were extracted from. The preliminary step is attributing an estimate of the subsoil V_s profile to all available experimental dispersion curves by applying, for instance, the procedure for the production of a consistent initial model presented in the previous paragraph. If no a priori model is available this can be replaced, only for the purpose of estimating the lateral variability of the parameters, by the result of the inversion of one of the experimental curves. The aim of attributing a rough estimate of the subsoil model to the experimental dispersion curves is to provide each curve a V_s profile to perform a sensitivity analysis. The lateral variability of each model parameter can then be estimated by comparing the experimental dispersion curves two by two, thus retrieving the ratios between corresponding parameters, either S-wave velocities or thicknesses according to the chosen simplification assumption. For the necessity to choose such simplification assumption, see the "Comparison between two dispersion curves" paragraph. Therefore, if the set of dispersion curves to be inverted is made up of n curves, every model parameter of a V_s model has $n-1$ estimates of its ratio with respect to the corresponding parameter of the other models. For the k^{th} model parameter the reciprocal ratios between model parameters derived from the comparison of every couple of dispersion curves form the n x n matrix $\mathbf{R}_k$:

$$\mathbf{R}_k = \begin{bmatrix} r_{1,1} & r_{1,2} & \cdots & r_{1,n} \\ r_{2,1} & \cdots & \cdots & \cdots \\ \cdots & \cdots & r_{n-1,n-1} & \cdots \\ r_{,n1} & r_{n,2} & \cdots & r_{n,n} \end{bmatrix} \qquad (16)$$

where the generic element $r_{i,j}$ is derived from the comparison between the i^{th} and j^{th} dispersion curve. By subtracting to all the ratios the mean of the ratios belonging to the same row (i.e. each ratio turns into the relative deviation from the average value of the parameter) we obtain $\mathbf{R'}_k$:

$$\mathbf{R'}_k = \begin{bmatrix} r'_{1,1} & r'_{1,2} & \cdots & r'_{1,n} \\ r'_{2,1} & \cdots & \cdots & \cdots \\ \cdots & \cdots & r'_{n-1,n-1} & \cdots \\ r'_{n,1} & r'_{n,2} & \cdots & r'_{n,n} \end{bmatrix} \qquad (17)$$

whose generic element is $r'_{i,j} = r_{i,j} - \bar{r}_i$ with $\bar{r}_i$ the mean of the ratios from the i^{th} row of $\mathbf{R}_k$.

Then, by averaging over the columns of $\boldsymbol{R}'_k$, the expected spatial variability for the k^{th} parameter is obtained:

$$\mathbf{ESV}_k = \left[\sum_{i=1}^{n} \left(\frac{r'_{1,i}}{n} \right) \quad \sum_{i=1}^{n} \left(\frac{r'_{2,i}}{n} \right) \quad \ldots \quad \sum_{i=1}^{n} \left(\frac{r'_{n-1,i}}{n} \right) \quad \sum_{i=1}^{n} \left(\frac{r'_{n,i}}{n} \right) \right] \qquad (18)$$

where $\mathbf{ESV}_k$ is the expected spatial variability for the k^{th} model parameter, i.e. a vector whose elements represent an estimate of the trend of the k^{th} parameter value along the survey line. A simplified sketch of the presented method is displayed in Figure 3.10.

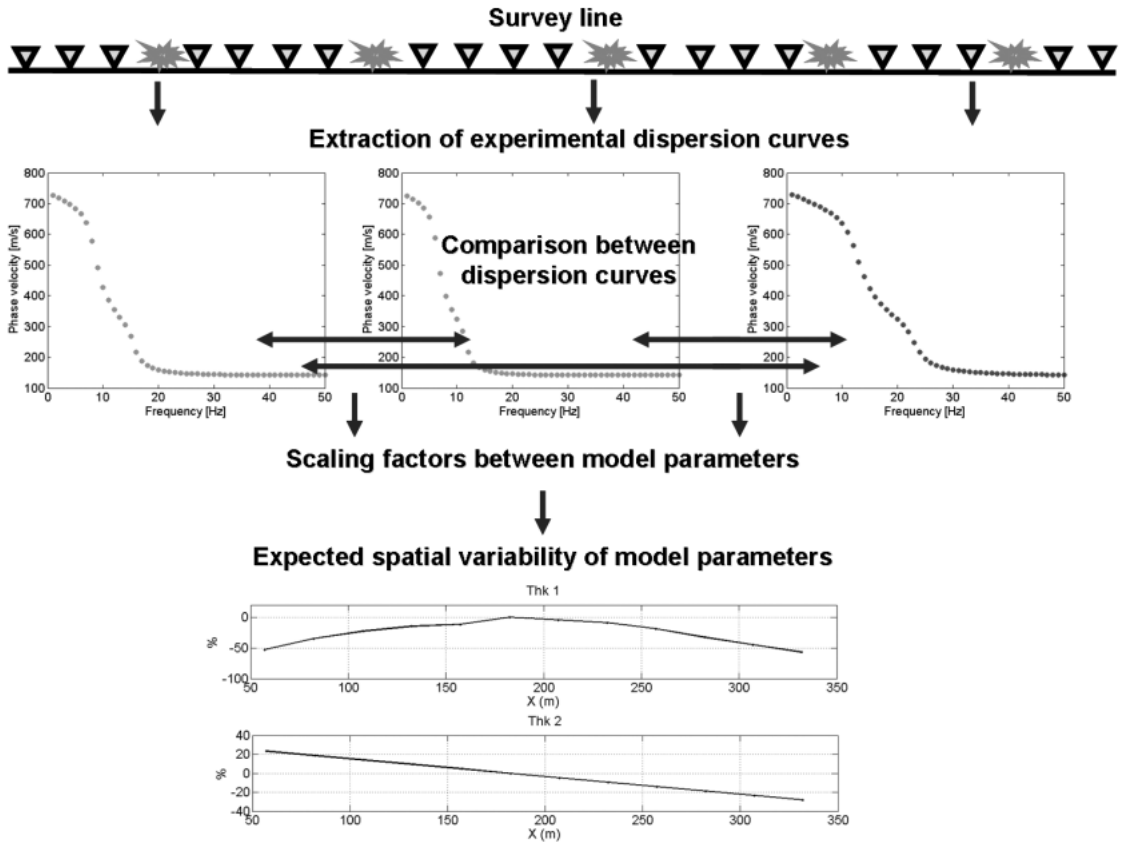

Figure 3.10 – Sketch of the method for the estimation of the expected lateral variability of V_s model parameters

The estimated lateral variability can then be used to tie different 1D model through spatial regularisation in the inversion, for instance using a laterally constrained inversion scheme (Socco et al., 2009). The basic idea is to customize the strength of lateral constraints on the expected lateral variability of the model parameters: where the

variability is higher, constraints can be loosened, while they can be strengthened where the model parameters are expected to assume similar values.

SYNTHETIC DATA

The procedures for the production of a consistent initial model and for the estimation of the lateral variability of V_s model parameters was firstly tested on two synthetic datasets.

The first synthetic dataset presented in this work was originally produced by Boiero and Socco (2010). The model was generated through a finite element method available code (COMSOL Multiphysics®, stress-strain module) using an axial symmetric scheme and a Ricker signal (dominant frequency 10 Hz) to simulate the seismic source. The model (Figure 3.11) is linear elastic isotropic and presents three layers, topographic unevenness and a dipping layer: its seismic properties are reported in Table 3.1.

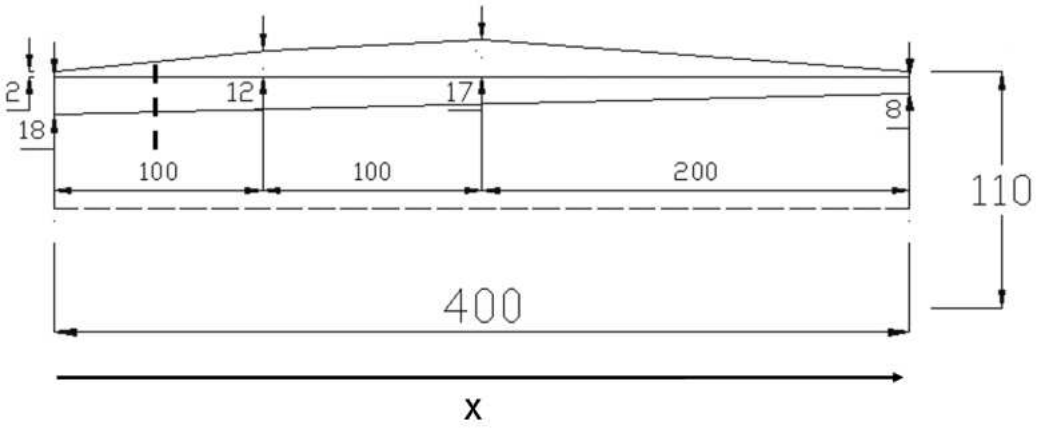

Figure 3.11 – Geometry of the first synthetic model: all dimensions are in meters. The vertical thick dashed line visible on the left side marks the position of the simulated down-hole test used to build the initial model.

Table 3.1 – Seismic properties of the layers of the first synthetic model.

Layer	V_P [m/s]	V_S [m/s]	ρ[kg/m^3]
1	240	120	1800
2	340	170	2100
3	500	270	2400

The generated dataset represents a typical multifold seismic survey with geophones every 5 m and shot points every 20 m. As for the dispersion curves extraction, the procedure is extensively described in the aforementioned paper by Boiero and Socco (2010). A set of 12 dispersion curves (Figure 3.12) was retrieved from the stacked *f-k* spectrum computed for each position of a moving window of 24 channels with an overlap between neighbouring positions of the window of 75%. The dataset to be inverted is hence a series of dispersion curves evenly-spaced along the seismic line.

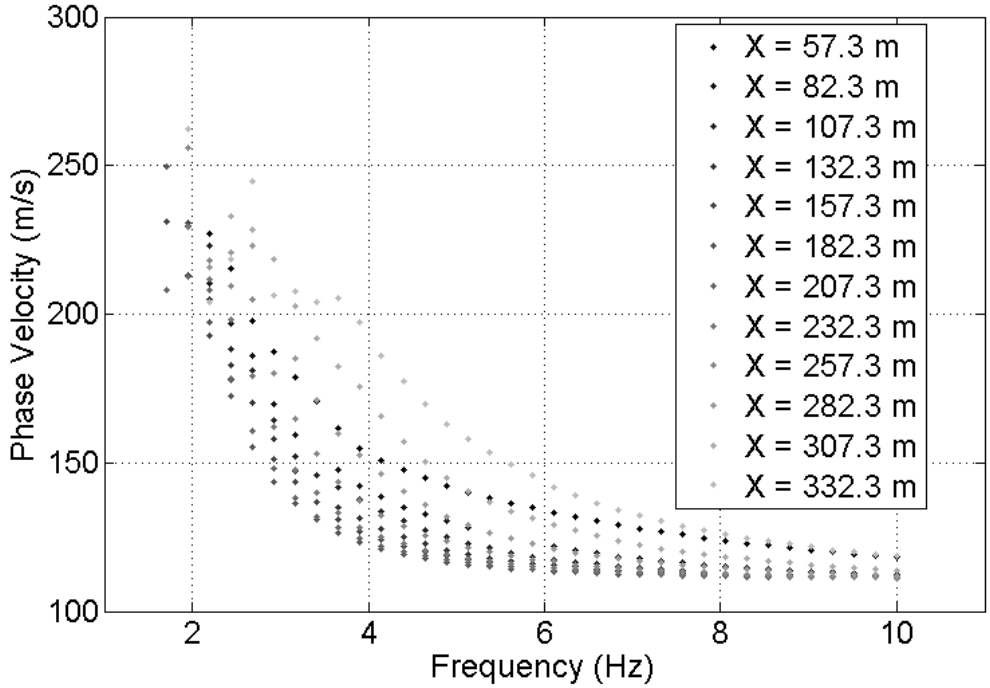

Figure 3.12 – Dispersion curves extracted from the first synthetic model. Each dispersion curve is identified by the X value of its corresponding reference point.

We applied our proposed methods to this dataset. First, we produced an initial model based on a priori information by supposing that a log survey had been performed by the position of the leftmost dispersion curve of the synthetic model (Figure 3.11, see thick black dashed line). The vertical V_s profile that is supposed to be known in that position was extended to the whole survey line, by adapting it according to the comparison of the dispersion curves. Velocities were assumed to be constant, and only thicknesses were left free to vary. The obtained initial model is displayed in Figure 3.13: both interfaces depth were reconstructed with a good degree of accuracy, as the relative estimation errors never exceed 12 % (Figure 3.14).

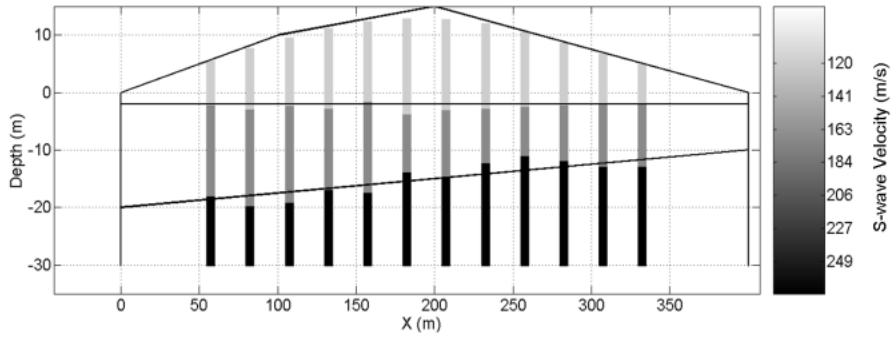

Figure 3.13 – Consistent initial model produced by spreading the exact Vs profile indicated in Figure 3.11 to the whole survey line. Thin black lines indicate the actual position of the model interfaces and its boundaries.

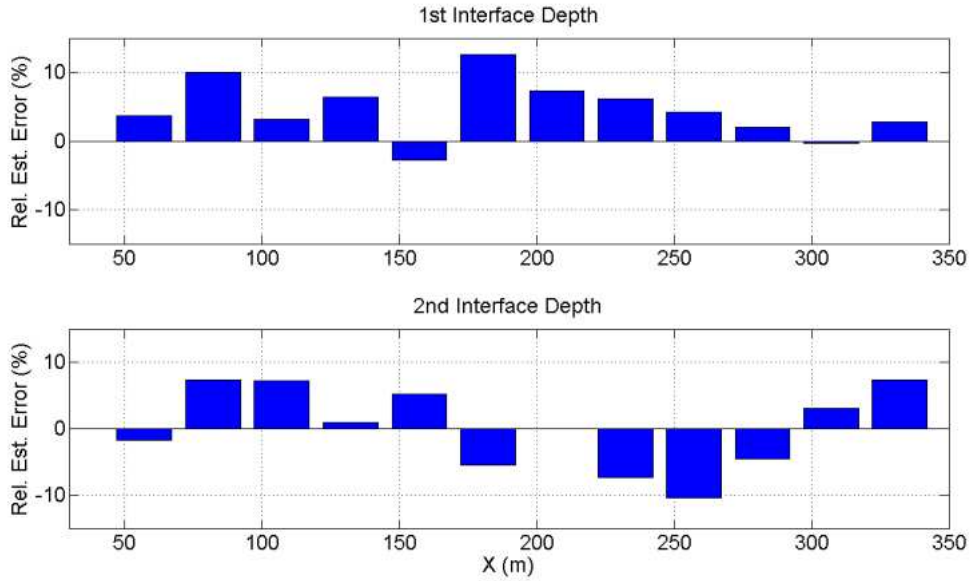

Figure 3.14 – Relative estimation errors for the interfaces depths of the first synthetic model.

We also computed the expected spatial variability for the V_s model layers thicknesses (Figure 3.15), assuming constant S-wave velocity values. In Figure 3.15b the expected spatial variability shows a good agreement with the actual trend of the corresponding parameters.

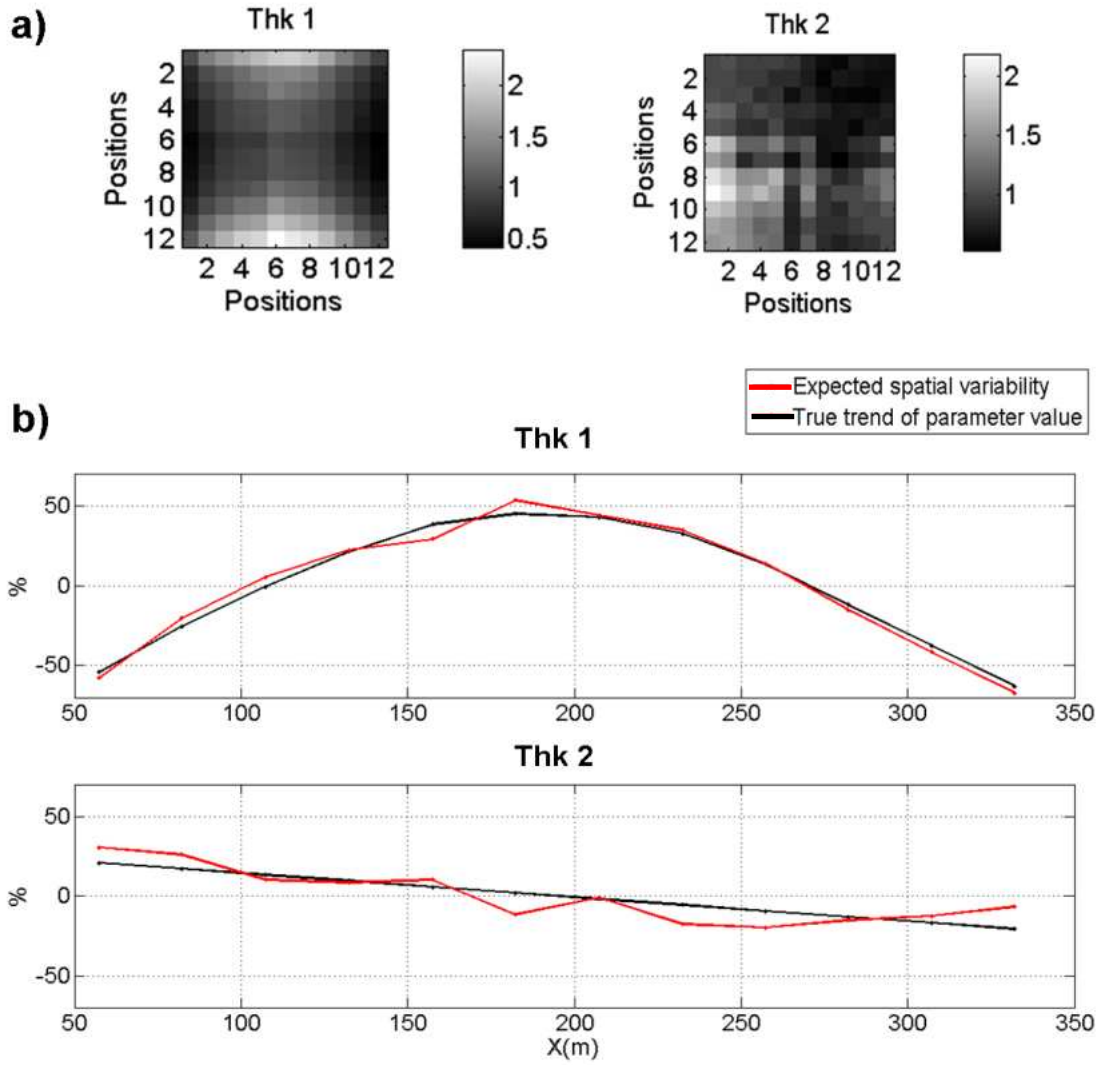

Figure 3.15 – Expected spatial variability of the thicknesses of the first synthetic model. a) ratios among corresponding the thicknesses computed for every couple of dispersion curves (matrices $\boldsymbol{R}_k$ of equation 16) and b) represents the derived expected spatial variability (vectors $\boldsymbol{ESV}_k$ of equation 18) compared with the true trend of the values of the two thicknesses.

The second synthetic dataset was originally produced and used by Socco et al. (2011). It was generated by means of a finite-difference code for numerical simulations FD2.0, implemented by the Geophysics Laboratory of Politecnico di Torino in FORTRAN 90/95 standard and based on the works by Chapman (1994) and Nyhoff (1997). FD2.0 is able to produce, starting from a 2D subsoil layered model described by the seismic properties of its materials, a seismic dataset characterized by spatial sampling consistent with the mesh size and by a fixed number of shots. The geometry of the synthetic model is represented in Figure 3.16 and the seismic properties of the layers

are reported in Table 3.2: again, the model is characterized by significant lateral variations, as a basin is present on the left side of the model while on the right side the second layer progressively emerges reducing the thickness of the shallower layer up to 10 m.

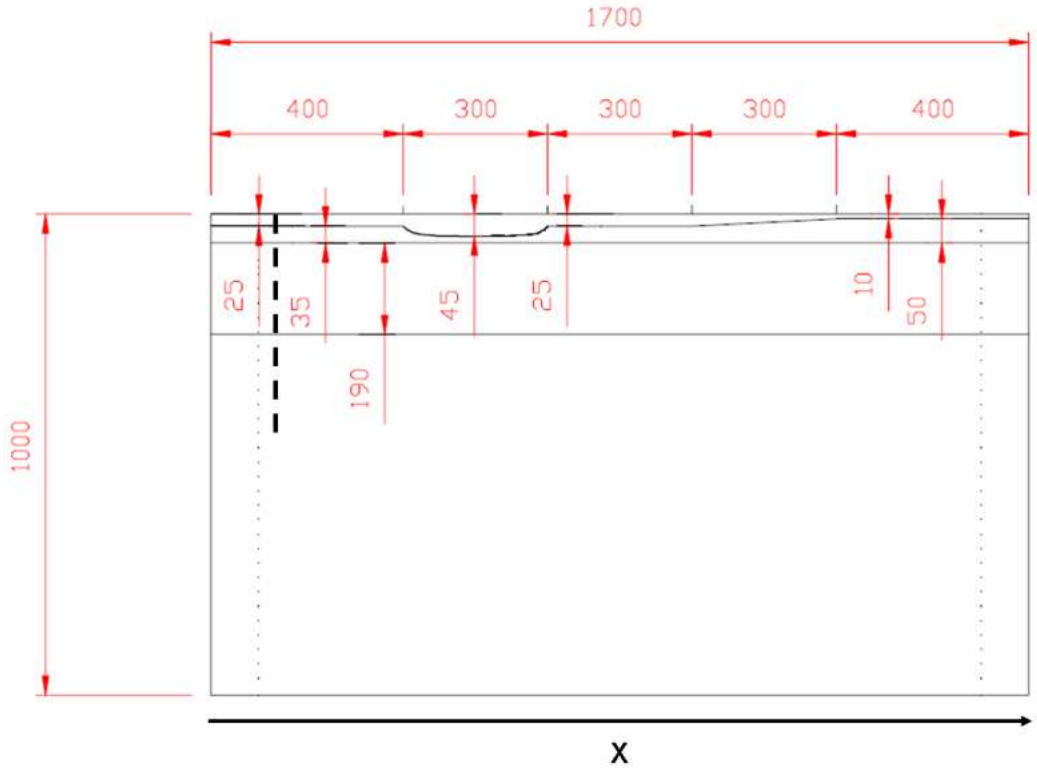

Figure 3.16 – Geometry of the synthetic model: all dimensions are in meters. The vertical dashed line visible on the left side marks the position of the simulated down-hole test used to produce the initial model. Side and bottom boundaries are modelled as absorbing boundaries.

Table 3.2 – Seismic properties of the layers of the second synthetic model.

Layer	V_P [m/s]	V_S [m/s]	ρ[kg/m^3]
1	800	500	1800
2	1300	800	1800
3	1800	1100	2000
4	2600	1600	2400

As for the shot simulations a Ricker source centred at 10 Hz was used: a multifold seismic survey was simulated, with shots every 10 m and spacing between neighbouring receivers of 5 m. A dispersion curves extraction technique, similar to that described in

Boiero and Socco (2010) for the previous synthetic model, was applied: a moving window 200 m wide was progressively shifted by 100 m steps along the simulated seismograms and a set of 14 dispersion curves was extracted (Figure 3.17). Again, the V_s profile located at the thick black dashed line in Figure 3.16 was supposed to be known and spread to the survey line and customized according to the available surface wave data, assuming constant velocities and estimating the trend of the layers thicknesses along the line.

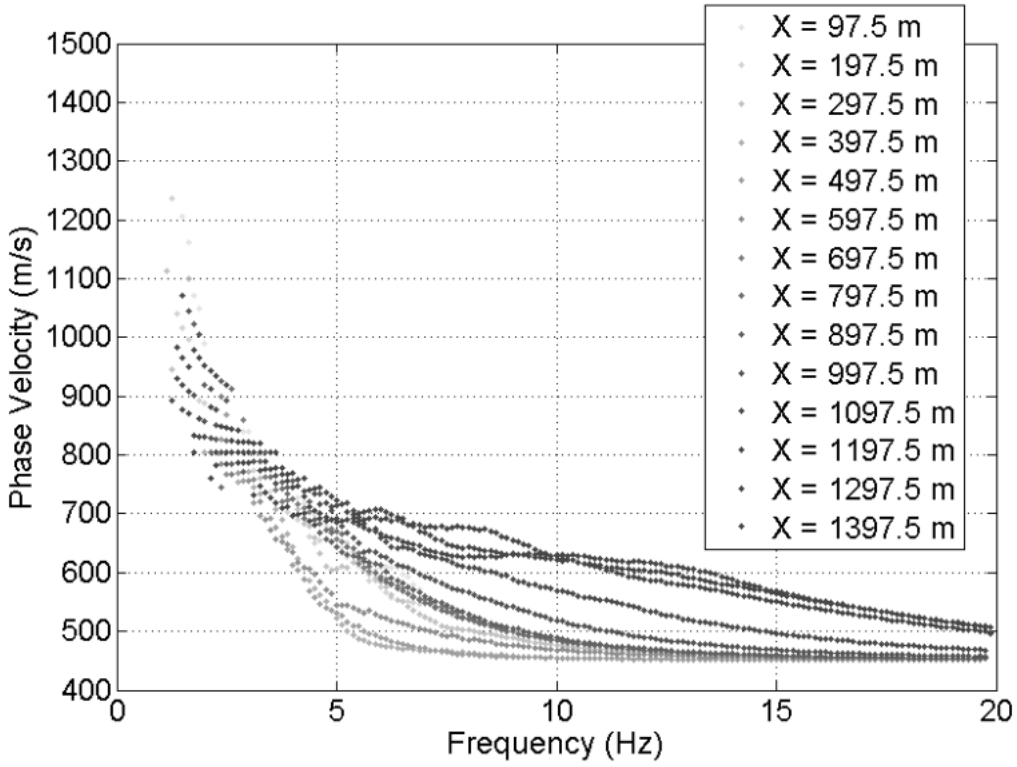

Figure 3.17 – Dispersion curves extracted from the second synthetic model. Each dispersion curve is identified by the X value of its corresponding reference point.

The obtained model is represented in Figure 3.18 and the relevant relative estimation errors for the interfaces depths are reported in Figure 3.19.

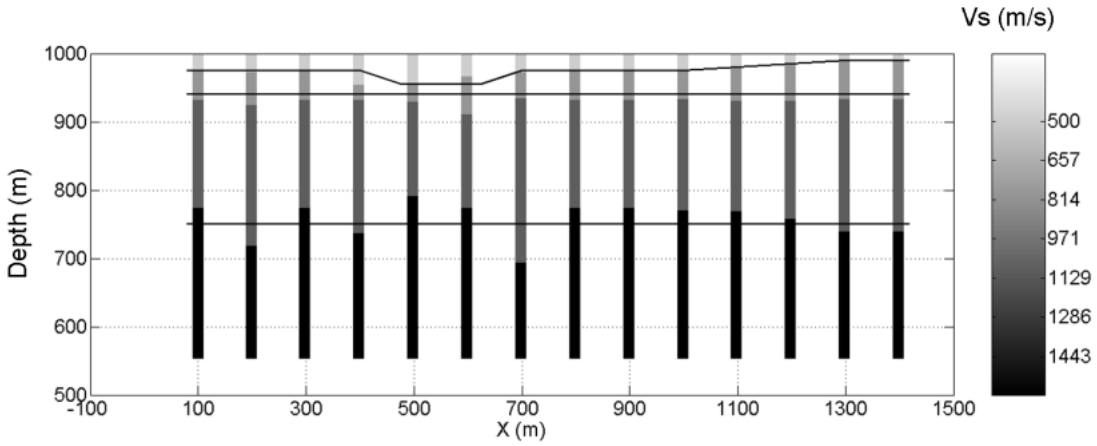

Figure 3.18 – Consistent initial model produced by spreading the exact V_s profile indicated in Figure 3.16 to the whole survey line. Thin black lines indicate the actual position of the model interfaces.

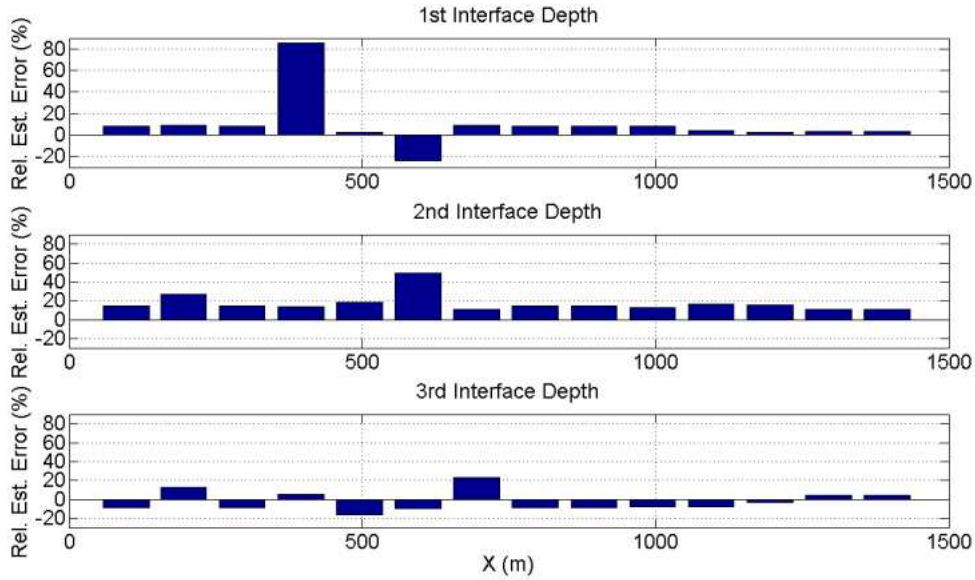

Figure 3.19 – Relative estimation errors for the interfaces depths of the second synthetic model.

On the whole, results are satisfying, as the majority of the errors are equal or lower than 20 %: however, estimation errors are greater than those found for the previous synthetic dataset, probably because of the lower quality of the dispersion curves. The most remarkable errors are produced for the vertical V_s profiles located at or near the basin on the left side of the model: being the window used for the dispersion curves extraction 200 m wide, the dispersion curves cannot perfectly follow the trend of

lateral variations as they are not representative of the vertical profile beneath the centre of the receiver spread.

We then estimated the expected lateral variability for the layers thicknesses (Figure 3.20).

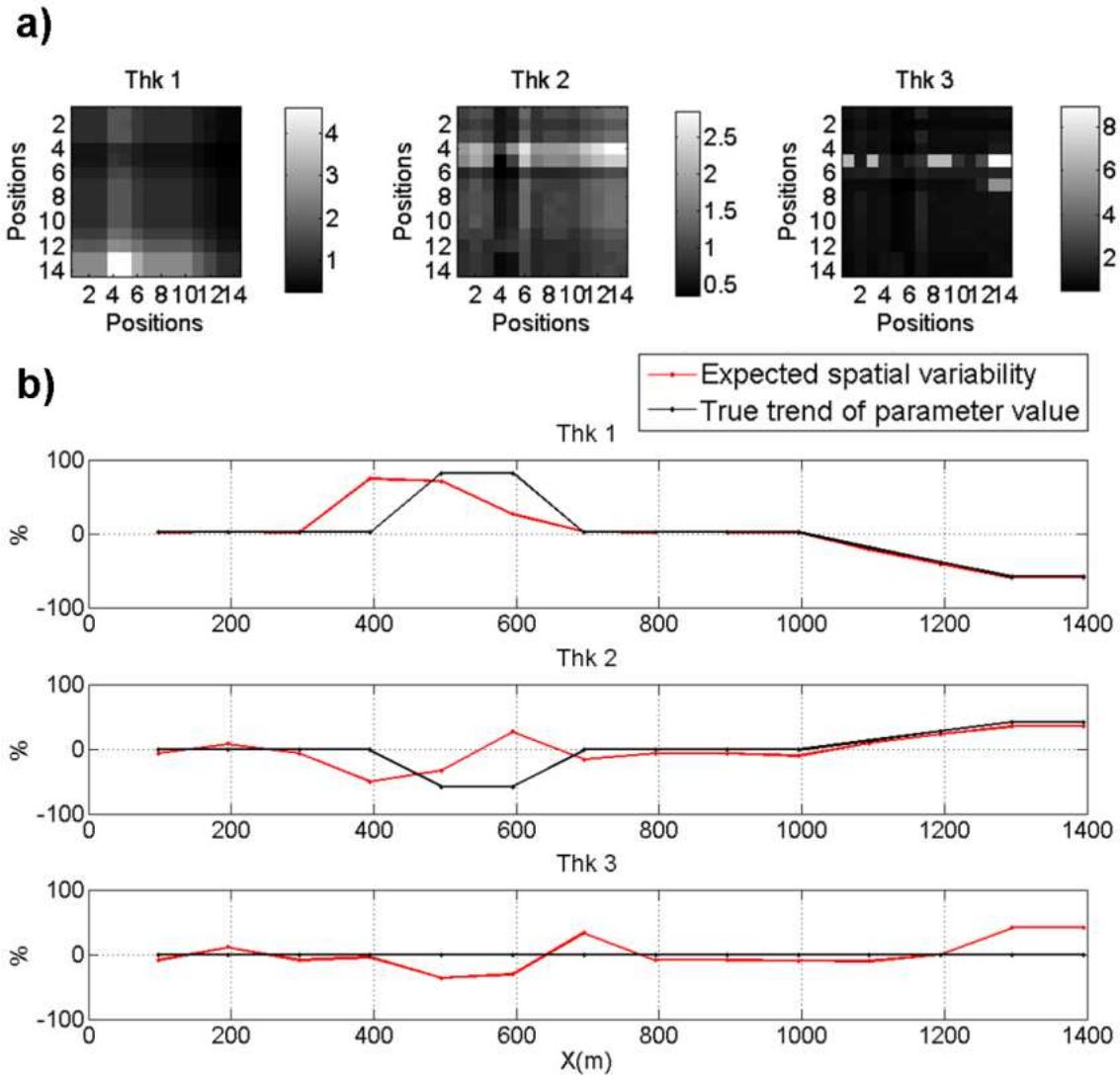

Figure 3.20 – Expected spatial variability of the thicknesses of the second synthetic model. a) ratios among corresponding the thicknesses computed for every couple of dispersion curves (matrices $\boldsymbol{R}_k$ of equation 16) and b) represents the derived expected spatial variability (vectors $\boldsymbol{ESV}_k$ of equation 18).

As it is shown in Figure 3.20b, the gradual emerging of the second layer in the right hand side part of the model is better reconstructed than the basin (see Figure 3.16 for the model geometry): in fact, being the window used for the dispersion curves

extraction 200 m wide, the dispersion curves cannot fully follow the trend of sharp lateral variations (such as the extremities of the basin) as they are not perfectly representative of the vertical profile beneath the centre of the receiver spread. Finally, it must be noticed that the trend of the third layer thickness is estimated with lesser accuracy when compared to the upper layers thicknesses, as the sensitivity of the dispersion curves with respect to this parameters is poorer.

REAL CASE

The dataset was acquired in an alpine valley in NW Italy for a seismic risk assessment campaign (Socco et al., 2009). The geology of the site is characterized by shallow fluvial sediments whose thickness may vary between 10 and 50 m interposed by lacustrine sediments: the bedrock is expected to have a depth greater than 100 m in the central part of the valley. Two high resolution reflection surveys were carried out across the valley: both lines are about 800 m long and were acquired using 240 active channels with 10 Hz vertical geophones, 2 m geophone spacing, 6 m shot spacing, 1 ms sampling rate and 2 s recording time. Surface wave data are significantly present in the recorded seismograms, and were used to estimate the V_s distribution in the overburden. We applied our technique to one of the two lines, for which two S-wave down hole tests are available in its proximity (see Figure 3.21).

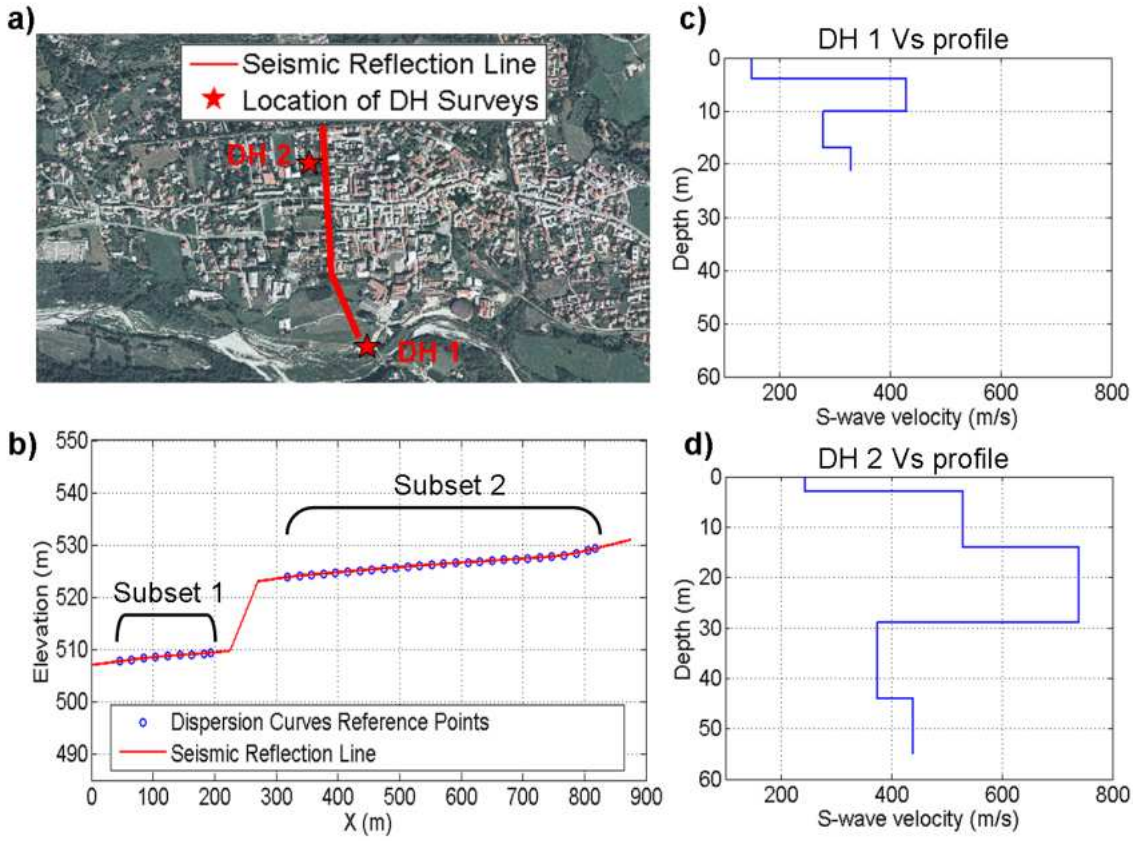

Figure 3.21 – a) Map of the site and location of the seismic refraction line (from which experimental dispersion curves were extracted) and of the down-hole tests; b) dispersion curves reference points and their division into two subsets; c) DH 1 test S-wave velocity profile; d) DH 2 test S-wave velocity profile.

As for the dispersion curves extraction, a moving window 24 channel wide with a 50% overlap between its neighbouring positions was chosen, so that a set of 36 dispersion curves was obtained (Figure 3.22). According to the topography of the site the curves can be easily divided into two subsets, separated by a steep slope: for each dispersion curves subset a V_s vertical profile estimated from a down-hole test is available, and so the profile from DH 1 test was used to build an initial model for subset 1 and the profile from DH 2 was spread along subset 2. Layer thicknesses were assumed to be constant in both cases, but thicker layers (second and third layer of DH 1 profile and third and fourth layer of DH 2 profile) were split into two sub-layers to allow for a greater complexity of the V_s distribution.

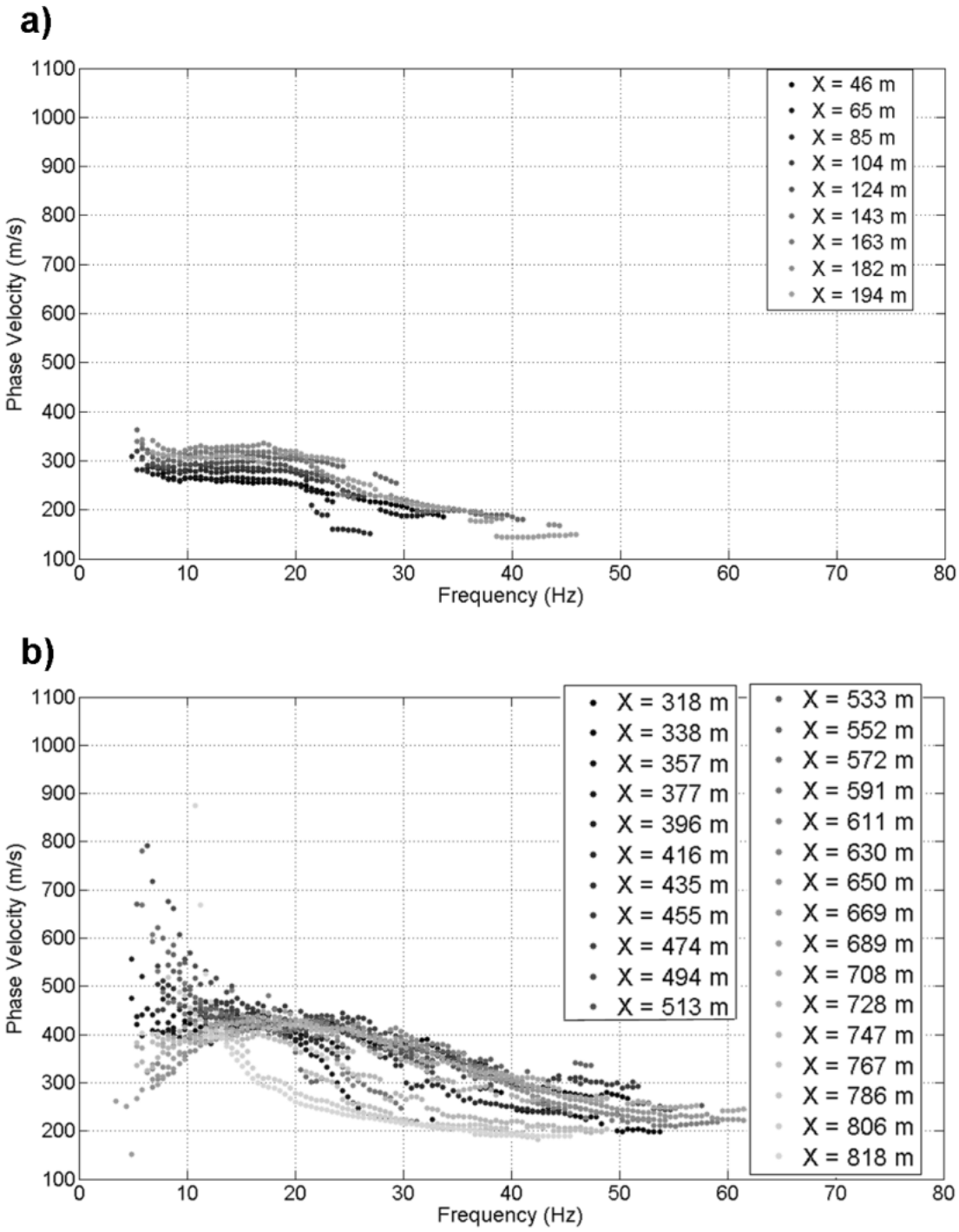

Figure 3.22 – Experimental dispersion curves from Torre Pellice site. Curves are represented with a colour scale according to the dispersion curves reference point. In a) the dispersion curves from the first subset (see Figure 3.21b) are reported, while in b) the second subset group is represented.

The corresponding two initial models are reported in Figure 3.23: both models highlight a velocity inversion linked to the presence of soft lacustrine deposits affecting almost all vertical V_s profile at around 500 m of elevation.

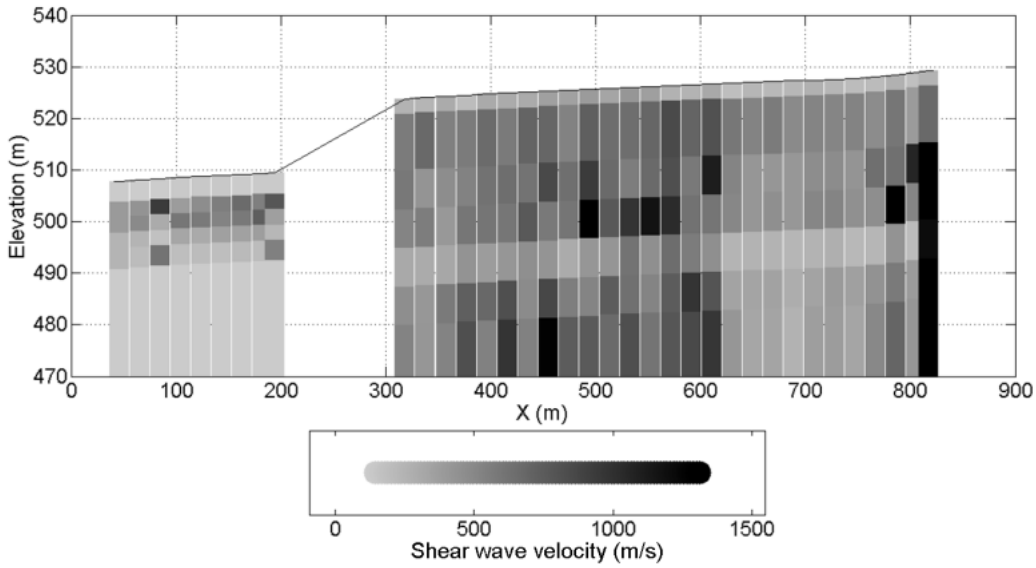

Figure 3.23 – Initial model for the real dataset. The model was obtained by extending the V_s profiles retrieved from two down-hole tests (DH 1 and DH 2 in Figure 3.21) to the experimental dispersion curves from subset 1 and 2 respectively (Figure 3.22).

Moreover, two regions characterized by higher values of S-wave velocity, especially at large depths, are detected at around X = 500 m and X = 800 m: as for the initial model for subset 1, an increase in S-wave velocity of the intermediate layers with greater X values is worth noticing. The reliability of both initial models is backed by their consistency (Figure 3.24) with the P-wave tomography performed on the same site and by their similarity to the results of a previously run laterally constrained inversion of the same experimental dispersion curves (Socco et al. 2009).

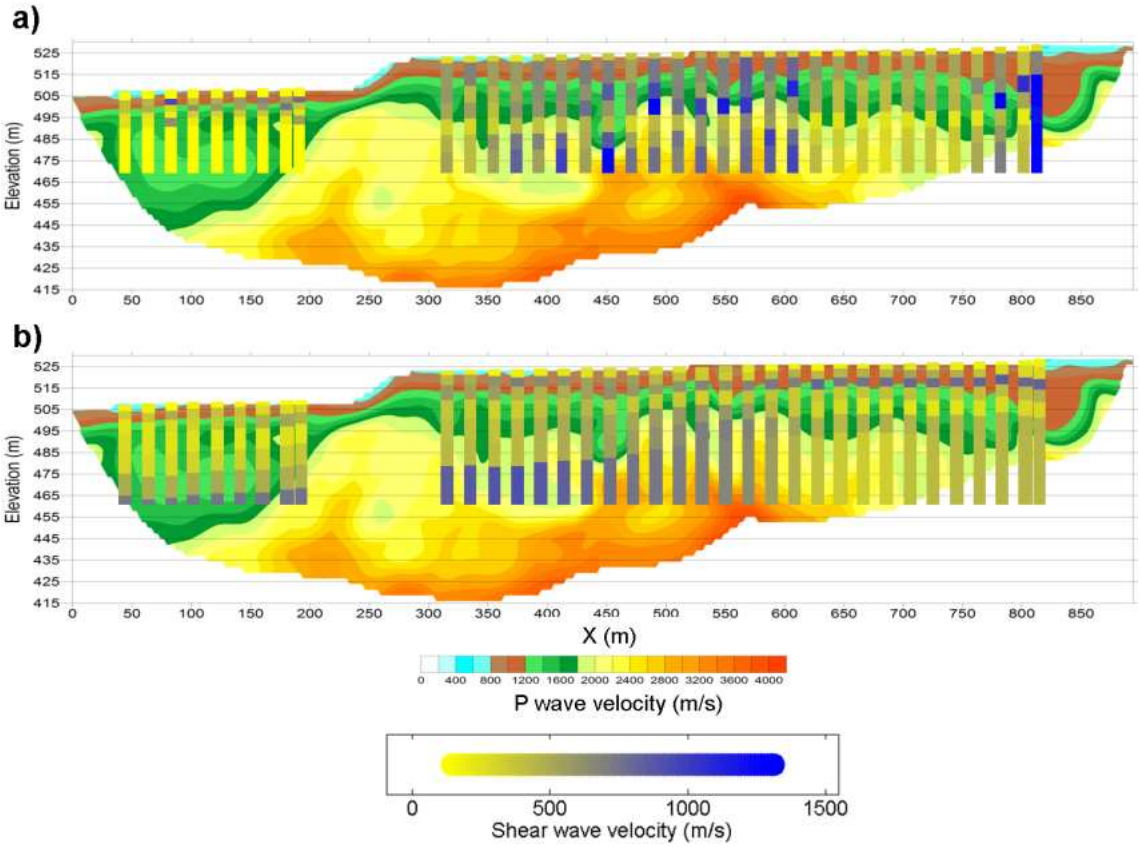

Figure 3.24 – a) Initial model for the real dataset, superimposed to the P-wave velocity tomography results; b) laterally constrained inversion results of same experimental dispersion curves datasets from Boiero et al. (2009) superimposed to the P-wave velocity tomography results.

We later computed the expected lateral variability of all layers S-wave velocities for both the dispersion curves subsets (see Figures 3.25 – 3.28).

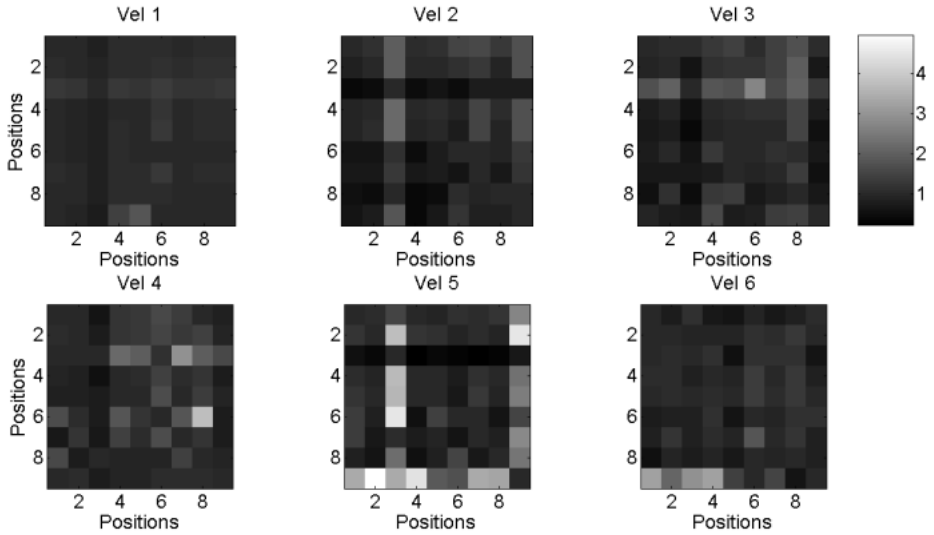

Figure 3.25 – Ratios among corresponding velocities (matrices $\mathbf{R}_k$ of equation 16) computed for every couple of dispersion curves from subset 1 (see Figure 3.21).

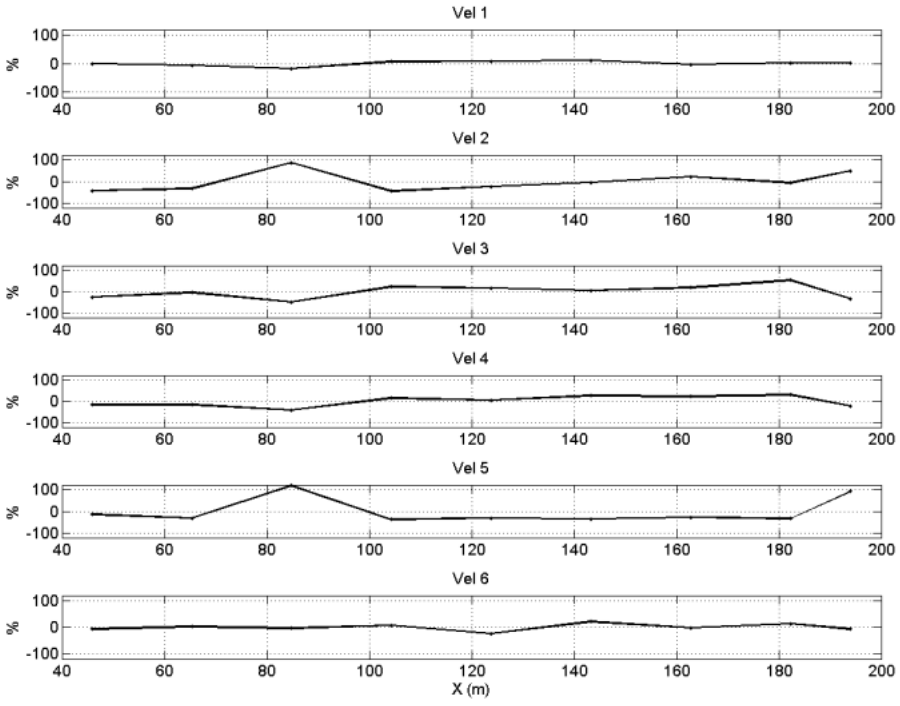

Figure 3.26 – Expected spatial variability (vectors $\boldsymbol{ESV}_k$ of equation 18) for the velocities of the layers relevant to the initial model retrieved for the dispersion curves from subset 1 (Figure 3.21).

As for the expected lateral variability for the first subset of curves (Figure 3.25 and 3.26), despite the anomalous behaviour of the V_s profile at X = 85 m, a gradual increase towards greater X values of the S-wave velocities of the second, third and fourth layer can be observed, while the shallowest and the two deepest layers velocities tend to remain almost constant. Switching to the estimated lateral variability for subset 2 (Figures 3.27 and 3.28), the two upper layers substantially keep their S-wave velocities constant, but the four deeper layers see their V_s values increase up to approximately X = 625 m, then their S-wave velocities are decreased until 750 m, where they increase again (probably, this latter increase is overestimated, reaching values of 250 % and more). The aforementioned features are in good agreement with the dispersion curves inversion results already presented by Socco et al. (2009) and with the results of the P-wave tomography performed on the same site (Figure 3.24).

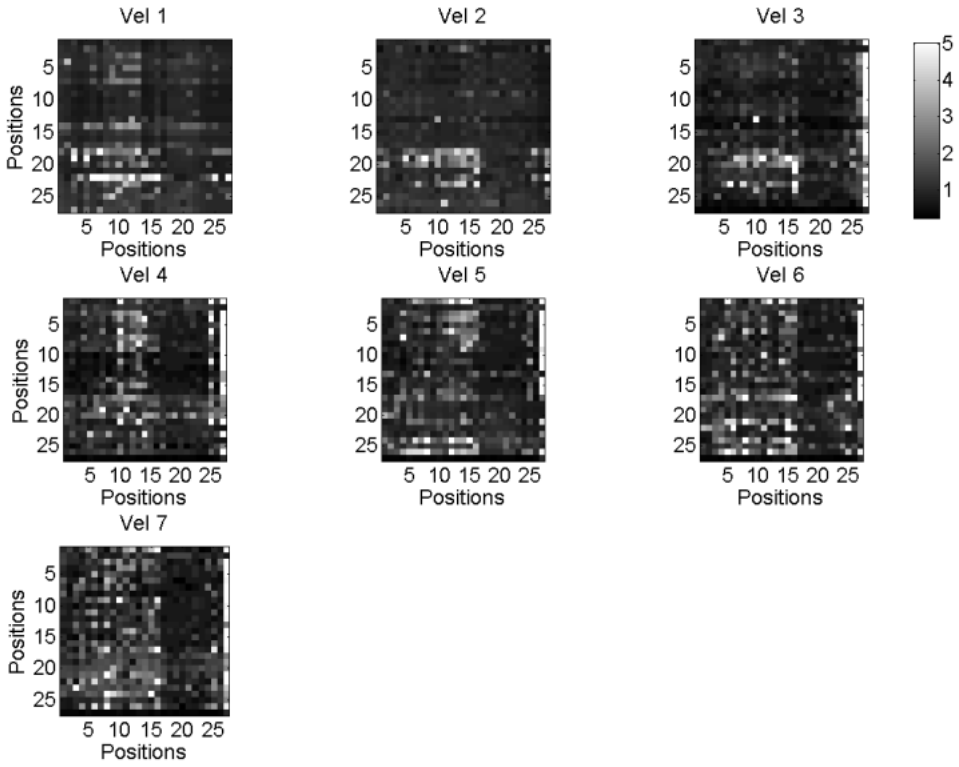

Figure 3.27 – Ratios among corresponding velocities (matrices $\boldsymbol{R}_k$ of equation 16) computed for every couple of dispersion curves from subset 2 (see Figure 3.21).

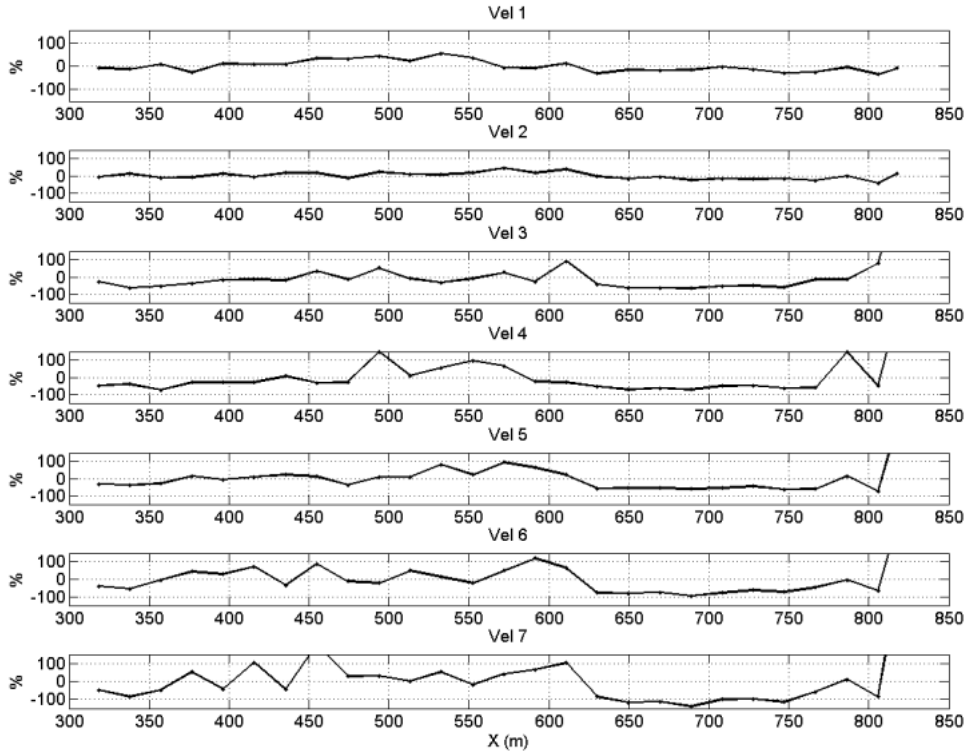

Figure 3.28 – Expected spatial variability (vectors $\boldsymbol{ESV}_k$ *of equation 18) for the velocities of the layers relevant to the initial model retrieved for the dispersion curves from subset 2 (see Figure 3.21).*

DISCUSSION

We applied the two processing techniques presented in this chapter (the construction of an initial model exploiting local a priori information and the estimation of the spatial variability of V_S model parameters) to two synthetic and one real datasets.

As far as the synthetic datasets are concerned, the 2D structures of both models were satisfyingly reconstructed both by "spreading" known V_S profiles (Figures 3.13 – 3.14 and 3.18 – 3.19) and by evaluating the lateral variability of V_S models parameters (Figures 3.15 and 3.20). However, in both procedures a lower accuracy in the estimation of deeper layers parameters can be observed, as dispersion curves have a poorer sensitivity to parameters belonging to deeper layers than to shallow layers. Besides, the reliability of the results has proven to be quite dependent on the quality of the input set of dispersion curves, as the results we got from the first synthetic dataset, characterized by higher quality, are better than those obtained from the second one. However, these

two problems can be also met in the actual inversion process, where deeper model parameters may be unresolved and poor data quality can indeed affect the inversion results.

We also applied the same processing techniques to a set of experimental dispersion curves from a real acquisition line. The real dataset geology is particularly challenging, being characterized by lateral heterogeneities and a velocity inversion: two V_s profiles from down-hole tests are available in proximity of the seismic line, and we managed to extend these profiles to the whole survey line (Figures 3.23 and 3.24). We also reconstructed the spatial trend of the V_s model parameters (Figures 3.25 – 3.28). Though preliminary and rough they may be, the results we got are meaningful and reliable, as their agreement with the P-wave tomography results and with the V_s distribution from a previously performed laterally constrained inversion is remarkable (Figure 3.24).

Eventually, the applications to both synthetic and field data point out the main limitation of the two methodologies, i.e. the fact that it is only possible to consider the variation of one kind of parameter (i.e. either layers S-wave velocities or thicknesses).

CONCLUSION

We have set up two procedures to enhance the reliability of the surface wave method in investigating smooth 2D structures in the subsurface. The aim of the first technique is to build an initial model for the deterministic inversion of surface wave data by systematically integrating a-priori local V_s information available in proximity of the locations of the available experimental dispersion curves. The robustness of the inversion process can be hence improved by providing a reliable initial model for the inversion using local a priori information that are extended to the survey line and updated according to surface wave data in the form of dispersion curves. The second technique provides an estimation of the spatial variability of V_s model parameters based on the analysis of surface wave dispersion data (in particular, of a set of neighbouring dispersion curves). This preliminary assessment of the lateral variability of the V_s model can direct the choice of the method for the inversion of surface wave dispersion data: if a laterally constrained inversion algorithm is preferred, such estimate can be exploited for the tuning of lateral constraints. The strength of the constraints can therefore be based on data analysis and not on a priori or a posteriori considerations.

Both procedures are based on an algorithm able to retrieve the scale factors between the parameters of two 1D V_s models via the comparison of the two corresponding dispersion curves: the procedure is based on a sensitivity analysis and the following exploitation of the scale properties of surface waves.

After formalizing the two approaches, we applied them to two synthetic and one real datasets, all of them sharing the presence of lateral heterogeneities. As for the synthetic data, we correctly reconstructed the V_s distribution of both models, providing proper initial models and reliable estimates of the spatial trend of V_s model parameters. Regarding the application to the field data, we managed to extend the local a priori knowledge of V_s distribution provided by two down-hole tests to all the seismic line; we also reconstructed the overall trend of the V_s model parameters along the survey line. The validity of the results we got is confirmed by their agreement with other geophysical surveys performed on the same site and other analyses of the same data.

The application to real and synthetic data has also pointed out the weaknesses of the proposed methodologies: the main drawback of the two procedures is that they require to assume that either layers thicknesses or S-wave velocities are constant, so that the trend of either velocities or thicknesses can be estimated. Overcoming this limitation could be a starting point for future developments. Another perspective of future work is making the developed approaches more robust, as the quality of their results has proven to be heavily dependent on the quality of the input dispersion curves: a possible strategy would be to exploit dispersion curves higher modes in the whole procedure.

ACKNOWLEDGEMENTS

The author would like to thank eni e&p management for the permission to publish data relevant to the second synthetic model.

REFERENCES

Auken, E., and A. V. Christiansen, 2004, Layered and laterally constrained 2D inversion of resistivity data: Geophysics, 69, 752–761.

Bohlen T., Kugler S., Klein G. and Theilen F. 2004. 1.5-D Inversion of lateral variation of Scholte Wave dispersion. Geophysics 69, 330–344.

Boiero D., Bergamo P. and Socco L.. 2009. Retrieving consistent initial model for Surface Wave Inversion from local a priori information. In: Proceedings of Near Surface Geophysics – EAGE. Dublin, 7-9 September 2009.

Boiero D., Maraschini M. and Socco L.V. 2009. P and S wave velocity model retrieved by multimodal surface wave analysis. In: Proceedings of 71st EAGE Conference and Exhibition 2009, Amsterdam, 8-11 June.

Boiero D., Socco L.V. 2010. Retrieving lateral variations from surface wave dispersion curves. Geophysical Prospecting 58, 977-996.

Chapman S.J. 1994. Fortran 90/95: guida alla programmazione. Milano, McGraw-Hill.

Forbriger T. 2003. Inversion of shallow-seismic wavefields: II.Inferring subsurface properties from wavefield transforms. Geophysical Journal International 153, 735-752.

Foti S., Comina C., Boiero D. and Socco L.V. 2009. Non-uniqueness in surface wave inversion and consequences on seismic site response analyiss. Soil Dynamics and Earthquake Engineering, 29, 982-993.

Grandjean G. and Bitri A. 2006. 2M-SASW: Multifold multichannel seismic inversion of local dispersion of Rayleigh waves in laterally heterogeneous subsurfaces: application to the Super-Sauze earthflow, France. Near Surface Geophysics 4, 367–375.

Haskell N.A. 1953. The dispersion of surface waves on multilayered media. Bulletin of the Seismological Society of America 43, 17-34.

Luke B., Calderòn C., Stone R. C. and Huynh M. 2003. Non-uniqueness in inversion of seimic surface-wave data. Proceedings of Symposium on the Application of Geophusics to Engineering and Environmental Problems (SAGEEP), Environmental and Engineering Geophysical Society, Denver, CD-ROM SUR05, 1342-1347.

Malovichko A. A., Anderson N. L., Dmitriy A., Malovichko A., Shyloakov D. Y. and Butirin P. G. 2005. Active-passive array surface wave inversion and comparison to borehole logs in southeast Missouri. Journal of Environmental and Engineering Geophysics 10, 243-250.

Maraschini M., Boiero D., Foti S. and Socco L.V. 2011. Scale properties of the seismic wavefield – perspectives for full-waveform matching. Geophysics 76 no. 5, 1-7.

Metropolis, N., M. N. Rosenbluth, A. W. Rosenbluth, A. H. Teller, and E. Teller, 1953, Equation of state calculations by fast computing machines: Journal of Chemical Physics, **21**, 1087–1092

Nazarian, S., 1984, In situ determination of elastic moduli of soil deposits and pavement systems by spectral-analysis-of-surface waves method: Ph.D. dissertation, University ofTexas at Austin.

Neducza B. 2007. Stacking of surface waves. Geophysics 72, V51–V58.

Nyhoff L. 1997. Fortran 90 for engineers and scientists, Sanford Leestma – Upper Saddle River: Prentice-Hall.

Sambridge M. 2001. Finding acceptable models in nonlinear inverse problems using a neighbourhood algorithm. Inverse Problems 17, 387-403.

Semblat, J. F., M. Kham, E. Parara, P. Y. Bard, K. Pitilakis, K. Makra, and D. Raptakis, 2005, Seismic wave amplification: Basin geometry vs soil layering: Soil Dynamics and Earthquake Engineering, 25, 529-538.

Socco L.V. and Boiero D. 2008. Improved Monte Carlo inversion of surface wave data. Geophysicsl Prospecting 56, 357-371.

Socco L.V., Boiero D., Foti S., Maraschini S., Piatti C., Bergamo P.,Garofalo F., Pastori M. and Del Molino G. 2011. Surface wave analysis for S-wave static corrections computation. SEG International Exposition & 80th Annual Meeting 17-22 October, 2010.

Socco L.V., Boiero D., Foti S. and Wisén R. 2009. Laterally constrained inversion of ground roll from seismic reflection records. Geophysics 74, 35-45.

Socco L.V., Foti S. and Boiero D. 2010. Surface-wave analysis for building near-surface velocity models – Established approaches and new perspectives. Geophysics 75, no. 5, 75A83-75A102.

Socco L.V. and Strobbia C. 2004. Surface-wave method for near-surface characterization: a tutorial. Near Surface Geophysics, 2004, 165-185.

Tarantola A. 2005. Inverse problem theory and methods for model parameter estimation . Philadelphia, USA: SIAM.

Thomson W.T. 1950. Transmission of elastic waves through a stratified solid medium. Journal of Applied Physics 21, 89-93.

Tian G., Steeples D.W., Xia J. and Spikes K.T. 2003. Useful resorting in surface-wave method with the Autojuggie. Geophysics 68, 1906–1908.

Wathelet M. 2005. Array recordings of ambient vibrations: surface-wave inversion. PhD thesis at Université de Liège – Faculté des Sciences Appliquées, France.

Wisén R. and Christiansen A. V. 2005. Laterally and mutually constrained inversion of surface wave seismic data and resistivity data. Journal of Environmental & Engineering Geophysics 10, 251-262.

4 - APPLICATION OF METHODS BASED ON SURFACE WAVES POWER AND PHASE SPECTRA FOR THE DETECTION OF DISCONTINUITIES ON SYNTHETIC AND REAL DATA

In the previous chapters (1-3) I have illustrated some techniques to provide the surface wave method the tools to handle smooth lateral variations in the subsurface: I have also presented some applications of these methods, which have been tested on synthetic and field data and, in one case, on a dataset derived from small-scale seismic experiments carried out on a physical model. The present chapter is instead devoted to address the problem of sharp, sudden lateral heterogeneities in the subsurface when applying the surface wave method. In case of abrupt lateral variations, I have adopted the strategy to identify the position of the discontinuity, to process separately the seismic traces located on the two sides of the heterogeneity. This chapter therefore presents several methodologies to determine the location and the embedment depth of sharp heterogeneities in the subsurface.

ABSTRACT

Surface Wave techniques are characterized by a 1D approach which might prove unsatisfactory when relevant 2D effects are present in the investigated subsoil. In case of sharp and sudden heterogeneities in the subsurface a strategy to tackle this limitation is to estimate the location of the discontinuities and to separately process seismic traces belonging to quasi-1D subsoil portions. In the present work we have addressed our attention to methods aimed at locating discontinuities already available in literature and sharing the exploitation of anomalies in surface wave propagation and attenuation detected by means of the computation of phase and power spectra. The considered methods are the phase analysis of surface wave (MOPA), the autospectrum computation and the attenuation analysis of Rayleigh waves (AARW). These methods were developed for different purposes and different scale problems, but we applied them to the same datasets (a synthetic data from a FEM simulation and a real dataset from a seismic reflection line) sharing the presence of an abrupt lateral variation (in the real case, a seismic fault) perpendicularly crossing the acquisition line. We also developed a method derived from the AARW for the detection of sharp discontinuities in the subsoil from large and redundant datasets and we tested it on our real case dataset. All three

methods proved to be effective for the detection of the discontinuity, by portraying phenomena linked to the presence of the heterogeneity, such as the interaction between forward and reflected wave trains, and energy concentration and subsequent decay at the fault location. Moreover, additional information were retrieved, such as the embedment depth and the sharpness of the retrieved discontinuity.

INTRODUCTION

In surface wave analysis, usually, the experimental dispersion curve of surface waves (i.e. phase velocities vs frequencies) undergoes an inversion process yielding as a result an estimate of the shear wave velocity profile in the subsoil. However, surface wave techniques are mainly used to retrieve 1D subsoil models: in 2D environments the 1D approach neglects the presence of lateral variations and, since the surface wave path crosses different materials, the retrieved dispersion curve results in a simplified or misleading description of the site (Boiero, 2009). In literature, some strategies to overcome this limitation are present. A first strategy is based on a spatial windowing of the seismic traces (Bohlen et al. 2004; Boiero and Socco, 2011), so that the dispersion curve becomes a local property of the subsoil beneath the receivers whose traces are weighted more. This solution can be effectively adopted in case of smooth lateral variations: if the spatial window is successively shifted along the seismic profile, a set of dispersion curves can be extracted and the gradual change in subsoil seismic parameters can be reconstructed with a laterally constrained inversion of the dispersion curves yielding a pseudo-2D section of the shear wave velocity in the subsurface (Bergamo et al.,2010; Socco et al. 2009). In case of sharp and sudden 2D effects in the subsurface, another strategy should be preferred: it consists in estimating the location of discontinuities seismic parameters and processing separately seismic traces belonging to quasi-1D subsurface portions. The latter strategy is studied in the present work; among the available methods able to point out lateral heterogeneities, we focus on three of them:

- multi-offset phase analysis of surface waves (MOPA) presented by Strobbia and Foti (2006) and modified by Vignoli and Cassiani (2010);

- computation of the austospectrum of the seismic traces, as suggested by Zerwer et al. (2005) for the detection of cracks in concrete beams;

- attenuation analysis of Rayleigh waves (AARW) as developed by Nasseri-Moghaddam et al. (2005) for the estimation of the location and embedment depth of underground cavities. We also set up a procedure for an effective and quick application of the AARW to large multifold datasets such as the seismic reflection line which is our real case dataset.

The above-mentioned techniques, which will be briefly described in the following section, were applied to both synthetic and real datasets. As for the synthetic dataset, the model presents a sharp lateral variation caused by the sudden rise of the stiff halfspace (Figure 5.1); in the real dataset, the seismic line crosses a fault, so that an abrupt discontinuity is expected. The surface wave phase analysis was already tested on real and synthetic datasets similar to the ones we present in this study (Vignoli et al, 2011): on the contrary, the autospectrum method and the AARW were developed for smaller scale problems and for differently shaped lateral variations, respectively. The aim of the study is to test the applicability of the two latter techniques in fault detection cases and to compare the results of the three methods.

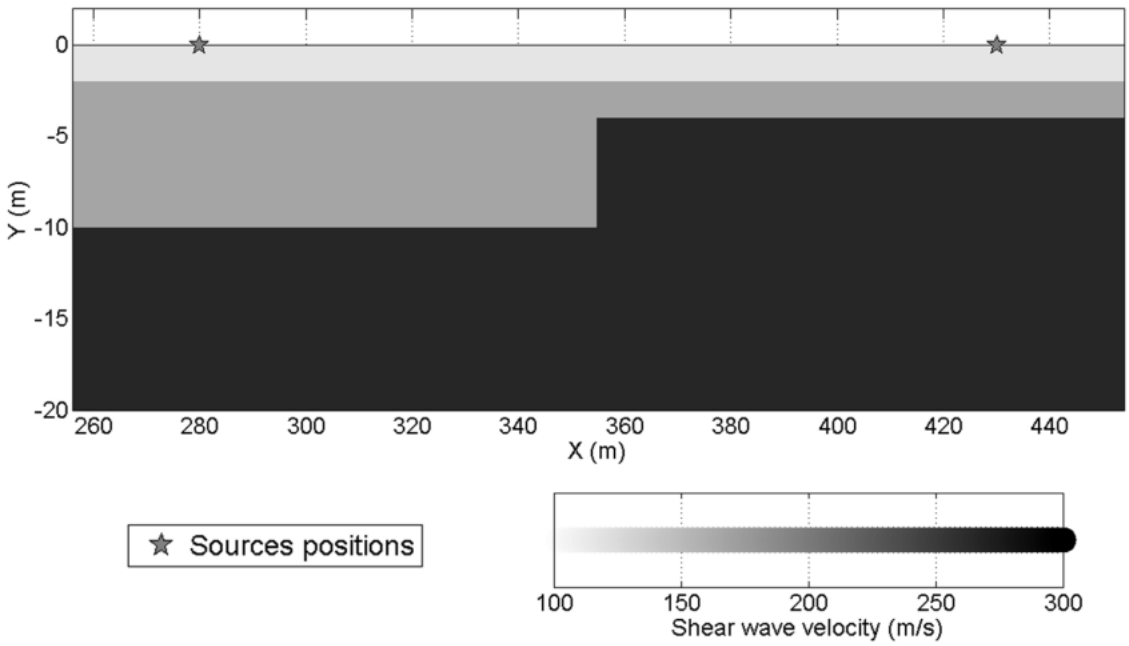

Figure 5.1- Synthetic model geometry: the V_S values for the three layers are (from top to bottom): 120 m/s, 170 m/s and 270 m/s. Only the central portion of the model is displayed: the synthetic model extends from X=0 to X=710 m and down to Y=-200 m without any other vertical or lateral variation.

METHODS

In the present section we briefly describe the three methods adopted in this work.

Multi-offset phase analysis of surface wave (MOPA).

This technique requires a multichannel seismic acquisition and it is based on the analysis of the phase of surface waves versus offset, frequency by frequency. The phase spectrum is computed for every seismic trace so that the trend of surface wave phase versus offset can be reconstructed for every frequency. By unwrapping the phase, the phase versus offset plot slope estimates the phase velocity for the considered frequency at a certain offset. As shown by Vignoli and Cassiani (2011), MOPA can be used for the evaluation of the local phase velocity of surface wave frequency by frequency and/or for the estimation of the position of sharp lateral variations, as a sudden change of the slope of the phase versus offset reveals a discontinuity in the phase velocity for the considered frequency. MOPA technique is able to exploit the data redundancy typical of a multifold seismic dataset for a robust extraction of the modal phase and a rigorous evaluation of the uncertainties and it has already proved its reliability when applied to datasets similar to those processed for this work (Strobbia and Foti 2006 and Vignoli and Cassiani 2011): therefore we limited ourselves to a rough application of MOPA, evaluating frequency by frequency the local phase velocity of surface wave simply derived from the slope of the unwrapped phase versus offset graph.

Autospectrum method.

This method is based on the computation of the autospectral density of every seismic trace *z(t)*:

$$|G_{xx}| = \{\mathrm{Re}[Z(\omega)]\}^2 + \{\mathrm{Im}[Z(\omega)]\}^2 \qquad (1)$$

where G_{xx} is the autospectral density and $Z(\omega)$ is the Fourier transform of $z(t)$ (from Zerwer et al. 2005). The autospectrum plot hence displays the energy content of a seismogram as a function of frequency and offset. Austospectrum calculations were exploited by Zerwer et al. (2005) for the detection of cracks in concrete members, as they observed that cracks cause strong Rayleigh wave reflections that are easily highlighted in the autospectrum plots: moreover they succeeded in estimating the depth of the cracks by pointing out the frequency marking the border between the frequencies

that undergo backward reflection phenomena and the frequencies that don't. Therefore, we applied the autospectrum method to our datasets with the aim of identifying anomalies in Rayleigh waves behavior due to lateral heterogeneities and to the propagation of the wave train through different materials.

Attenuation analysis of Rayleigh waves (AARW).

The procedure was developed by Nasseri-Moghaddam et al. (2005) to determine the location and the embedment depth of underground cavities using surface waves. Oddities in Rayleigh waves propagation are detected by means of the energy-distance (ED), logarithmic decrement (LD) and amplified logarithmic decrement (ALD) parameters: prior to the computation of such parameters, traces amplitudes are multiplied by a gain function to correct for the effect of geometrical spreading, so that anomalies only in surface wave propagation are detected. The energy-distance plot is based on the computation of the signal energy (E_z) for every receiver location as:

$$E_z = \sum_f \left| U_{f,z} \right|^2 \tag{2}$$

where $\left| U_{f,z} \right|$ is the amplitude of the spectrum at frequency f for receiver number z. Nasseri-Moghaddam et al. observed that the ED plot is characterized by fluctuations in the proximity of the void, allowing an estimation of the location of the cavity. The logarithmic decrement (LD) is defined as

$$LD = Ln \frac{U_{j,z}}{U_{j,z+1}} \tag{3}$$

where $U_{j,z}$ and $U_{j,z+1}$ are the Fourier spectrum amplitudes for frequency f_j computed at two consecutive receivers z and $z+1$. As stated by Nasseri-Moghaddam et al., LD highlights the either constructive or destructive interaction between the reflected and the propagating front: in particular, typical amplification-attenuation patterns can be spotted in the LD plot before and after the void location, and the frequency range at which such patterns are visible can help estimating the cavity embedment depth. To single out the frequencies most affected by the presence of the void, Nasseri-Moghaddam et al. suggest the computation of the Amplified Logarithmic Decrement (ALD):

$$ALD_j = \sum_{z=1}^{z_{max}-1} \left[Ln \left(\frac{U_{j,z} + \alpha}{U_{j,z+1} + \alpha} \right) \right]^{\beta} \tag{4}$$

where j refers to f_j, the frequency for which the ALD is computed, z_{max} is the maximum number of receivers, $U_{j,z}$ and $U_{j,z+1}$ are the Fourier spectrum amplitudes at frequency f_j for two consecutive receivers z and $z+1$, α is an experimental constant to reduce the effect of noise and β is an even exponent to magnify the peaks and keep the ALD values positive (in Nasseri-Moghaddam et al.'s paper α is assumed to be 0.5% the maximum value of the spectrum magnitude and β is 4: for the present work, we retained the same values). The ALD value can be normalized, thus obtaining the Nomalized Amplified Logarithmic Decrement (NALD):

$$NALD_j = \frac{ALD_j}{\max(ALD)} \qquad (5)$$

where j refers to the frequency f_j for which ALD_j and $NALD_j$ are computed. Nasseri-Moghaddam et al. show that values of NALD close to 1 are assumed by frequencies whose wavelengths are comparable with the embedment depth of the cavity. We applied the AARW procedure as developed by Nasseri-Moghaddam et al. to our synthetic and real datasets to test its effectiveness for an aim (detecting abrupt lateral heterogeneities) slightly different from the one it was primarily developed for (i. e. estimating the location of underground cavities). Moreover, we set up a procedure for a quick but effective analysis of the energy versus distance trend of a multifold seismic line, like the one constituting our real dataset. The procedure we propose requires a multifold 2D seismic acquisition and it is based on three steps:

- energy-distance plot is computed for all available shots, excluding the traces at small offsets whose geometrical attenuation follows the body waves attenuation trend. In this case, traces are not compensated by any gain function.
- a moving window is shifted along each ED plot and for each position of the window the exponent controlling the energy decay as a function of the offset (i.e. the slope of the ED plot reported in bi-logarithmic scale) is evaluated. In fact we assume that the intrinsic attenuation can be neglected, so that the energy trend as a function of offset is explained by the geometrical spreading alone:

$$\frac{E_{z+1}}{E_z} = \left(\frac{offset_{z+1}}{offset_z} \right)^{-\gamma} \qquad (6)$$

where E_z and E_{z+1} represent the signal energy at receivers z and $z+1$ (see equation 2), $offset_z$ and $offset_{z+1}$ are the distance from the source for receivers z and $z+1$ and γ is the decay exponent (γ = 2 for body waves and γ = 1 for surface waves geometrical spreading). Therefore, if the obtained γ value is 1, energy decays according to surface

wave geometrical attenuation rule; an γ value lower than 1 denotes energy accumulation and $\gamma > 1$ denotes an energy decay due to a reflection caused by a discontinuity in the subsoil. Decay exponents retrieved from the positive offset portion of ED plots are distinguished from the exponents obtained from negative offset portion of ED plots. Finally, all exponents derived from the same position of the moving window and from all available shots are averaged, so that for every position along the seismic line two exponents controlling the energy decay as a function of the offset are available: one for the positive offset traces and one for the negative offset traces. By following the trend of γ along the seismic line we expect to identify areas with sharp subsoil heterogeneities (e.g. faults) which should be characterized by values of γ far from 1, denoting energy concentrations and sudden decays: moreover, by separately processing decay exponents from negative and positive offset traces we expect to observe different behaviors according to the direction the wave front approaches the discontinuity. This procedure was applied only to the real dataset, as the synthetic data are not multifold, and its results are displayed in the "Real case" section.

SYNTHETIC DATA

We obtained the synthetic dataset by using the finite element method (FEM) code for numerical simulations COMSOL Multiphysics ®. Two mirror-like axial-symmetric, linear, elastic isotropic models were produced to simulate two shots whose sources are located at both ends of the synthetic recording array. We show the model in Figure 5.1: an upper 2 m thick layer tops a second layer whose thickness abruptly decreases from 8 to 2 m at the centre of the model. The model is a simplified representation of a fault-like pattern and to assess the applicability of the methods to this kind of lateral variations we simulated a very dense acquisition. As already mentioned, we simulated two shots, with the source position in (280,0) and (430,0) respectively: the used source signal was a Ricker source centred at 12.5 Hz. For both shots, we simulated the vertical vibration velocity at 301 synthetic receivers located on the top surface of the model between the two source positions with 0.5 m spacing (Figure 5.2).

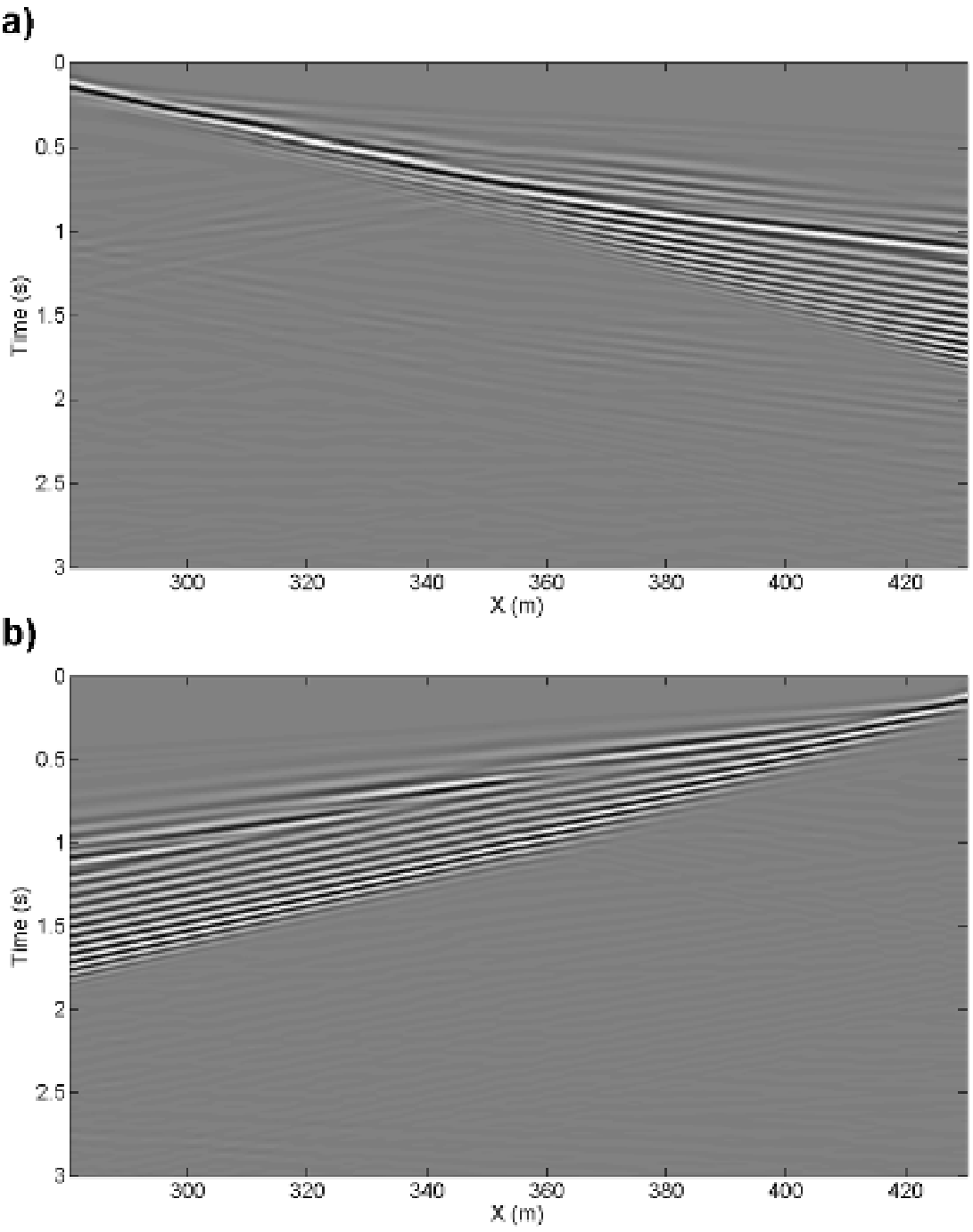

Figure 5.2 – a) Synthetic seismogram of the shot in (280,0) and b) synthetic seismogram of the shot in (430,0).

The time step for the numerical simulation was 1.25 ms, and the total simulation time was 3 s. Both seismograms are characterized by the presence of Rayleigh waves and P-guided waves phenomena, as shown in Figure 5.3. In Figure 5.3a and 5.3b the normalized *f-k* spectra of the traces belonging to the two 1D portions of the synthetic model are displayed: in both cases, P-guided wave dispersion modes can be spotted, as

dispersive events with phase velocities greater than 270 m/s (that is the cut-off velocity for Rayleigh waves, being the greatest S-wave velocity of the synthetic model) are present. In Figure 5.3c and 5.3d the energy maxima picked in 3a and 3b are reported in *f-v* domain and superimposed to the modulus of the determinant of the Haskell-Thomson forward modelling for the two respective 1D portions of the synthetic model (Maraschini et al. 2010) : the picked dispersive events (white dots) lie in the regions of the determinant surface whose modulus is close to 0, thus validating the synthetic dataset.

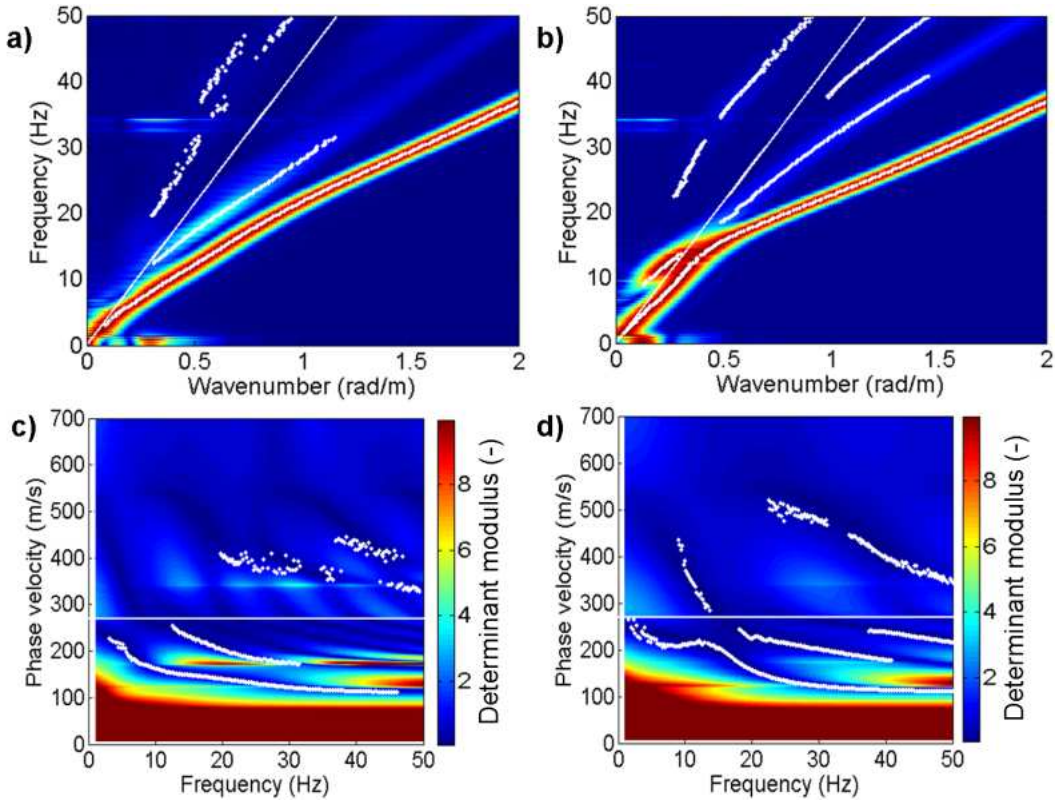

Figure 5.3 – a) Normalized f-k spectrum of the traces with X < 355 m of the shot in (280,0): white dots represent the picked energy maxima; b) normalized f-k spectrum of the traces with X > 355 m of the shot in (430,0): white dots represent the picked energy maxima; c) surface of the modulus of the determinant of the Haskell-Thomson forward modelling for the 1D portion of the model at X < 355 m: white dots represent the experimental dispersion curve and correspond to the energy maxima picked in a); d) surface of the modulus of the determinant of the Haskell-Thomson forward modelling for the 1D portion of the model at X > 355 m: white dots represent the experimental dispersion curve and correspond to the energy maxima picked in b). In all plots, the white continuous line is the constant velocity line at 270 m/s, marking the upper bound for Rayleigh wave dispersive events.

We applied the above-mentioned methods for the detection of lateral variations in surface wave propagation to both simulated shots; in Figure 5.4 the theoretical dispersion curves related to the S-wave velocity (V_s) profiles of the two 1D portions of the synthetic model are reported, in order to identify the range of frequencies that are most affected by the lateral heterogeneity (i.e. the frequencies whose phase velocity changes when switching from one 1D portion to another) and therefore to assess the reliability of the experimental results subsequently described.

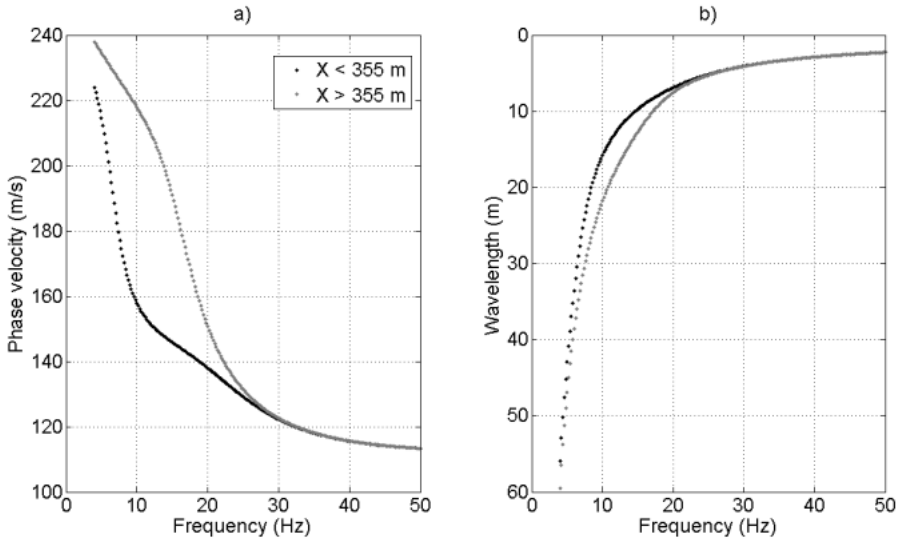

Figure 5.4 – Theoretical dispersion curves relevant to the two 1D portions of the synthetic model in Figure 5.1: a) dispersion curves in frequency-phase velocity domain and b) in frequency-wavelength domain.

Figure 5.5 reports the phase velocity-offset-frequency distribution plot retrieved by applying the MOPA technique to both synthetic seismograms: the position of the lateral heterogeneity clearly corresponds to the discontinuity in phase velocity that can be observed at around X=355 m in the 5-20 Hz frequency range. This result is coherent, both in terms of phase velocities and frequency range affected by the lateral variation, with the theoretical dispersion curves in Figure 5.4. In fact, the rise of the high S-wave velocity halfspace induces higher phase velocities in the lower frequencies. Moreover, the presence of ripples in the plot region before the discontinuity (X<355 m), mainly in the seismogram whose source is located before the step (Figure 5a), reveals an interaction between the propagating and the reflected wave train. The same effect is visible in the autospectrum plots (Figure 5.6): again, undulations due to the constructive or destructive interaction between propagating and back reflected wavefront are present

on the left hand side of Figure 5.6a plot and, at a lesser extent, on the right hand side of Figure 5.6b.

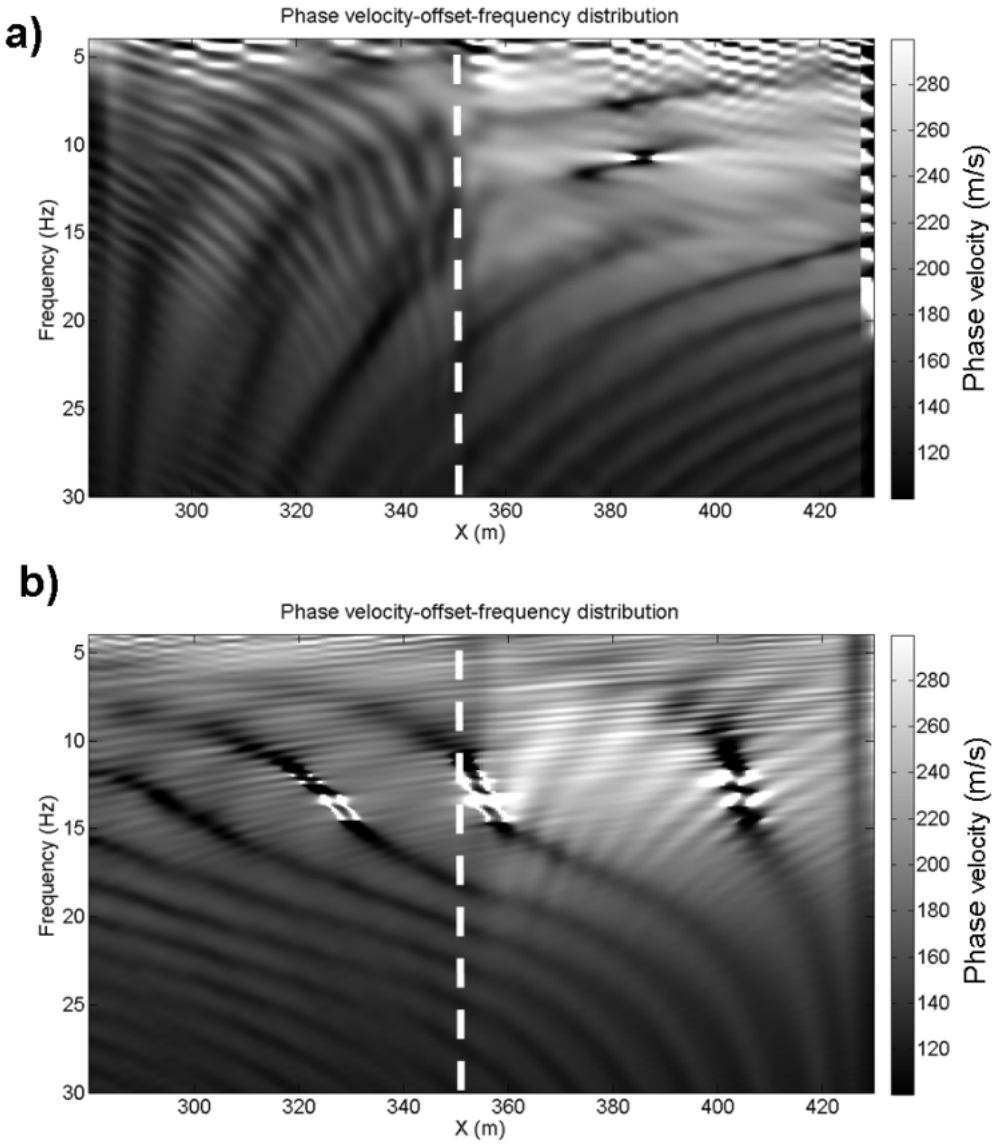

Figure 5.5 – Synthetic data: phase velocity distribution in offset-frequency domain for the shot in (280,0) (a) and for the shot in (430,0) (b). The vertical dashed white line marks the border between the two 1D portions of the synthetic model geometry (Figure 5.1).

Moreover, in Figure 5.6a, which refers to the seismogram whose shot is before the step, a clear energy decay occurs for frequencies lower than 15 Hz at around X=355 m: similarly to what was observed by Zerwer et al. 2005, the rise of the stiff halfspace blocks the propagating wave energy.

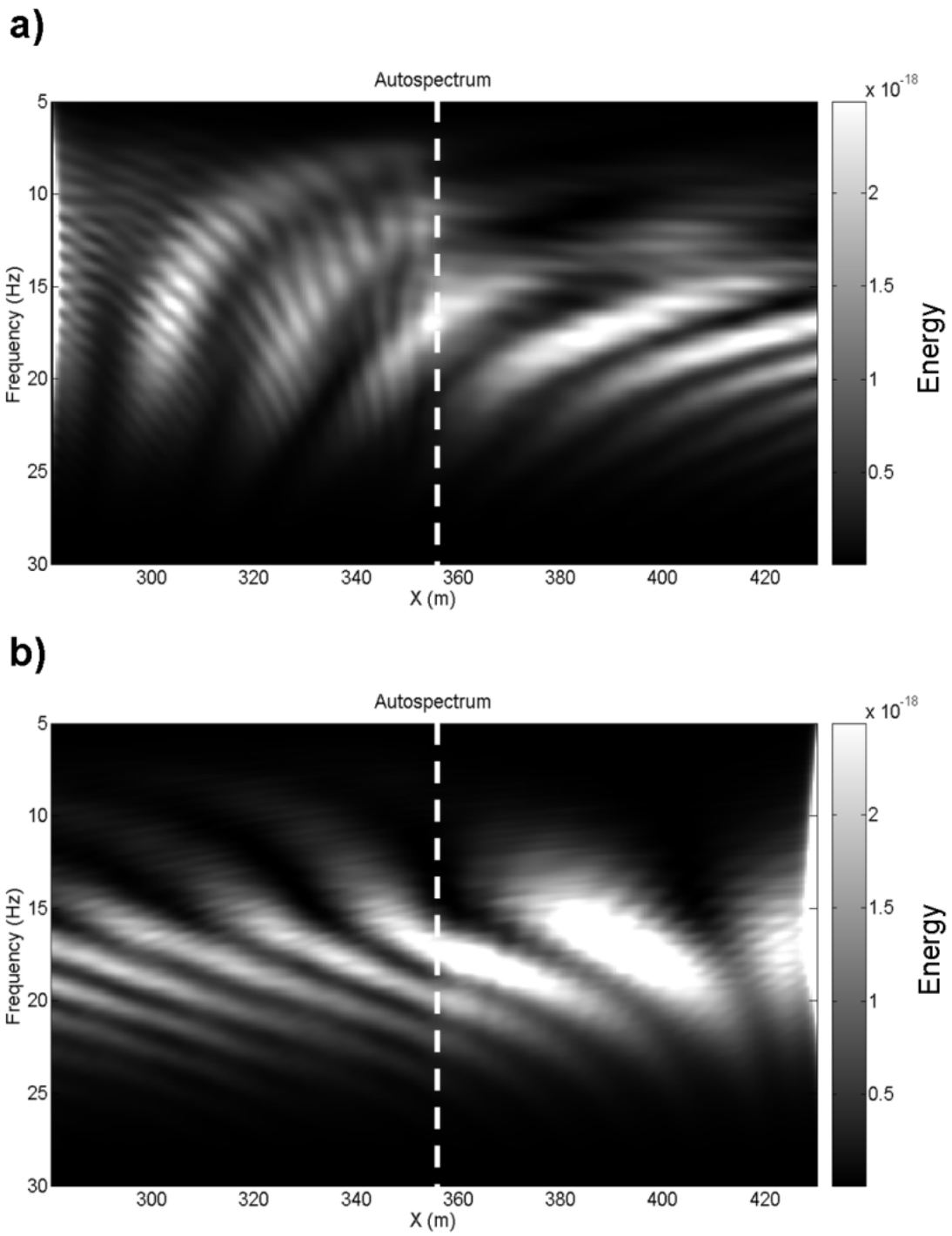

Figure 5.6 – Synthetic data: autospectrum plot for the shot in (280,0) (a) and for the shot in (430,0) (b). In both plots, the vertical dashed white line marks the position of the lateral variation in the synthetic model geometry (Figure 5.1).

The range of the frequencies affected by the lateral heterogeneity is therefore narrower than the one observed in Figure 5.5 and expected from Figure 5.4, probably because a dramatic energy decay does not occur for the frequencies whose wavelengths are only partially affected by the lateral heterogeneity (Figure 5.4b). As for the opposite

shot (Figure 5.6b) no substantial energy decay can be observed because the energy released by the seismic source cannot significantly spread beyond the top of the stiff halfspace, and in fact energy is concentrated at higher frequencies with respect to Figure 5.6a: the transition between the two 1D parts of the model is marked by a slight energy decrease as past the fault the energy is not bounded anymore by the shallow and stiff halfspace. Observations in good agreement with the autospectrum results can be retrieved from the energy-distance plot in Figure 5.7. At small offsets, signal energy decays very quickly following body waves geometrical spreading law: besides, the peaks that are present in the energy-distance trend of both shots are linked to P-guided wave events. The energy-distance plot of the shot in (280,0) shows an energy concentration at the location of the lateral variation (marked with "A" in Figure 5.7), similarly as observed by Masseri-Moghaddam et al. (2005): the energy concentration is due to the fact that, as it is shown in Figure 5.6a, part of the energy of the direct wave train is back reflected by the "step" of the halfspace and cannot spread beyond the lateral variation. The energy decline noticed in the energy-distance plot for the shot in (430,0) and labelled with "B" in Figure 5.7, instead, is due to change of depth of the upper boundary of the stiff halfspace: as the wave train passes beyond the "step", its energy is no more bounded by the shallow top of the halfspace and so an energy decay is noticed on the upper surface of the model, where the synthetic geophones are placed.

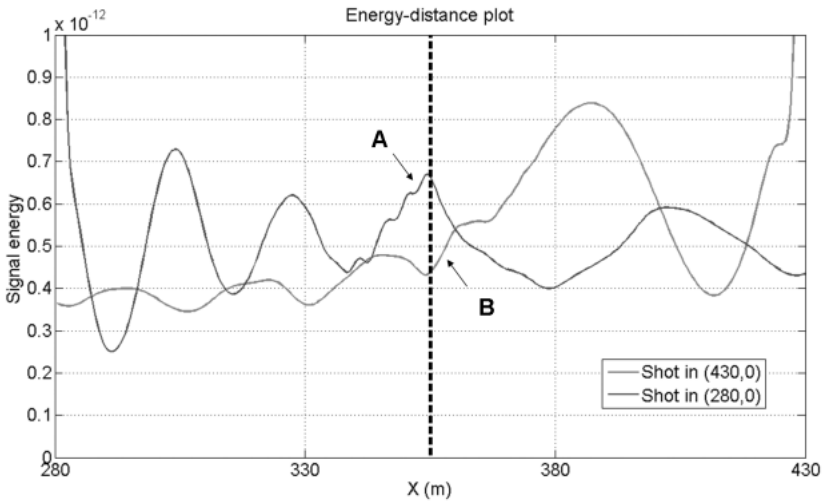

Figure 5.7 – Energy-distance plot for both simulated shots. The vertical dashed line marks the location of the lateral variation of the synthetic model geometry (Figure 5.1). "A" indicates the energy concentration due to the backward reflection of the direct wave train against the halfspace vertical interface while "B" points out the energy decay at the border between the two 1D portions of the synthetic model.

The interaction between forward and back reflected wave train is enhanced in the logarithmic decrement plot (Figure 5.8) where the logarithm of the ratio between $U_{j,z}$ and $U_{j,z+1,}$ which are the Fourier spectrum amplitudes at frequency f_j for two consecutive receivers z and $z+1$ (Equation 3), is displayed as a function of frequency and offset: positive values of logarithmic decrement show attenuation (as $U_{j,z}>U_{j,z+1}$), negative values correspond to amplification ($U_{j,z}<U_{j,z+1}$).

The patterns appearing in Figure 5.8a and, at a lesser extent, in Figure 5.8b between the source position and the lateral heterogeneity are attenuation/magnification curves denoting the interaction between the wave front propagating from the source and the waves backward reflected by the halfspace vertical boundary: these patterns are pretty similar to the ones observed by Nasseri-Moghaddam et al. (2005) and exhibit the same shape, as they asymptotically bend against the "step" location. The other curves that are present on the LD plots, turning from vertical to horizontal as the frequency decreases, are caused by the propagation of P-guided waves through the two upper layers of the model.

Finally, by applying Equation 4 and 5 we obtained the trend of NALD (Normalized Amplified Logarithmic Decrement) versus frequency for both synthetic seismograms. As already proved by Nasseri-Moghaddam et al. (2005), high NALD

values characterize the frequencies whose propagation is particularly affected by the lateral heterogeneity. As shown in Figure 5.9 NALD values close to 1 are retrieved in the frequency range 12-20 Hz: these frequencies correspond to wavelengths of approximately 10 m (that is the deepest position of the halfspace upper surface) and therefore their propagation touches entirely the lateral heterogeneity.

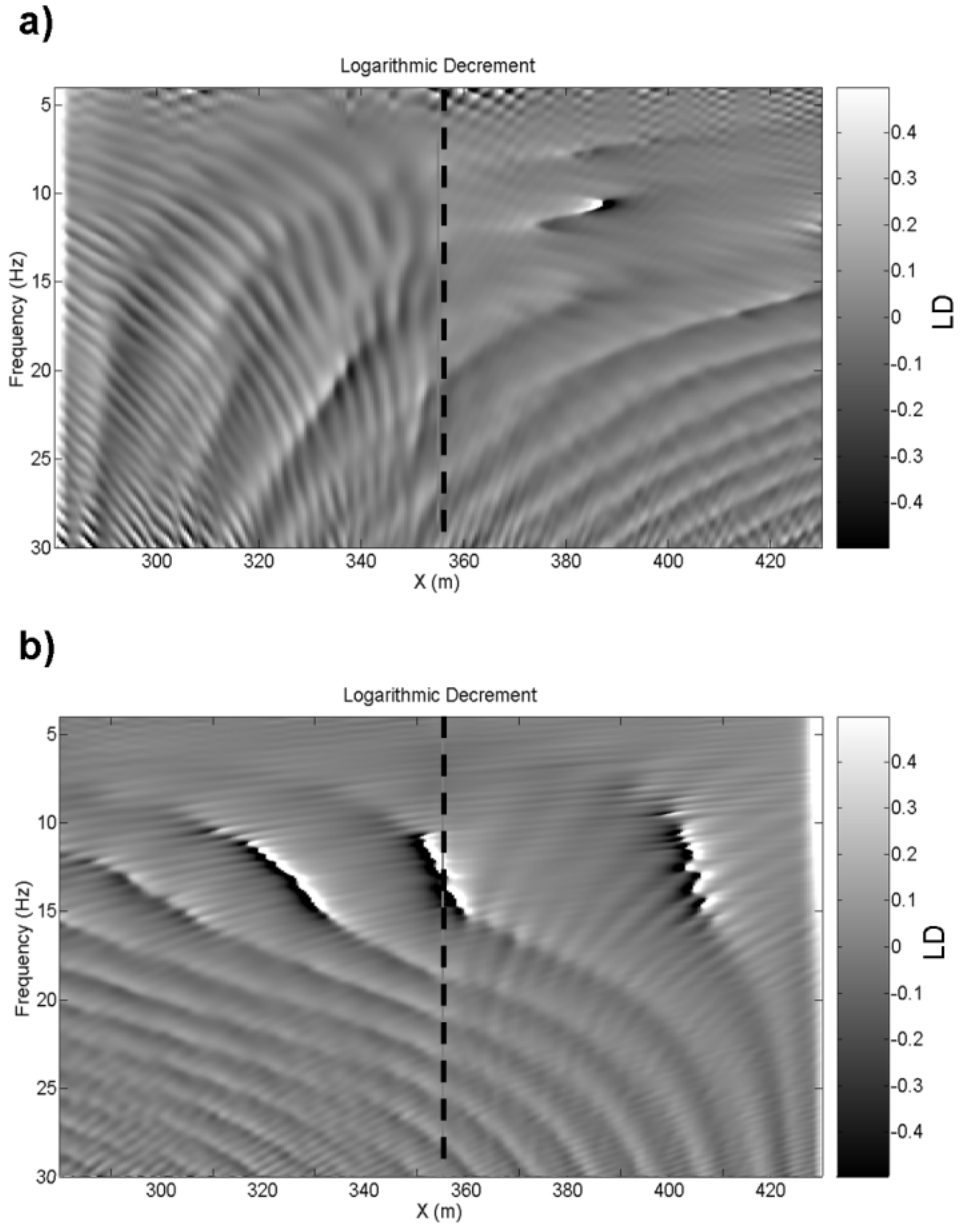

Figure 5.8 – Synthetic data: logarithm of the ratio between the spectral amplitude values assumed by the same frequency at neighbouring receiver locations for a) the seismogram whose shot is located at (280,0) and b) for the opposite shot. The vertical dashed black line marks the position of the lateral variation in the synthetic model geometry (Figure 5.1).

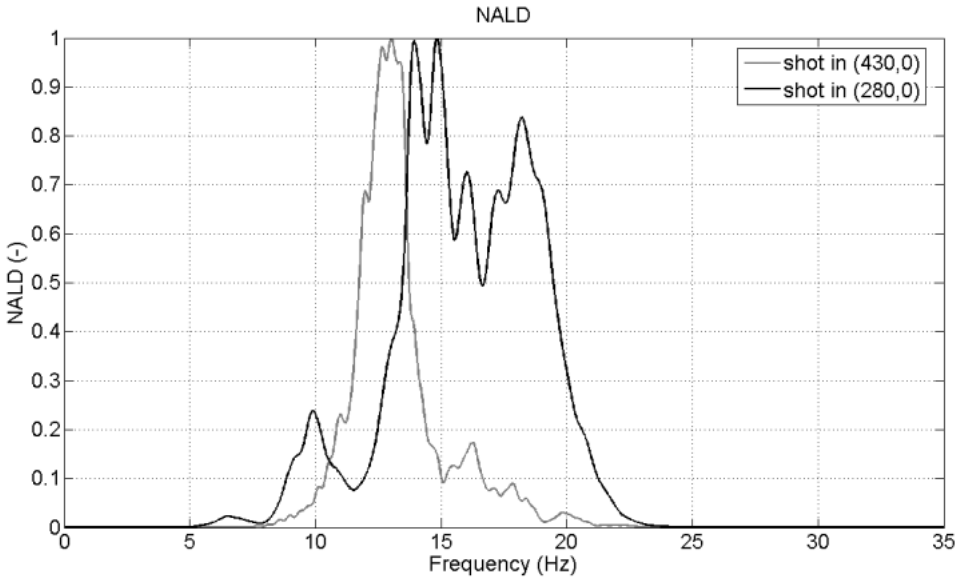

Figure 5.9 – Synthetic data: NALD versus frequencies for both simulated shots.

REAL CASE

Real dataset was acquired in New Zealand by ETH Zurich: the aim of the recording campaign (Carpentier et al., 2010) was the characterization of the Alpine fault in the South Island (Figure 5.10). Five seismic reflection lines between 400 and 1200 m long were acquired across the fault: 30 Hz vertical geophones were used, but nevertheless the presence of surface waves in the seismograms is significant. The five seismic datasets have already been interpreted by the geophysics group of ETH Zurich (Carpentier et al., 2010), and a seismic reflection section and a P-wave tomography results are available for every seismic line, allowing a localization of the main fault and of the minor side faults and an estimation of their maximum depth (500 m approximately). Being the presence of ground roll in the seismograms significant, surface wave data too were analyzed and interpreted, with aim of estimating the S-wave velocity behavior and the Poisson's ratio of the shallower layers (Garofalo et al. and Konstantaki 2011). Without going into details, both the P-wave tomography sections and the surface wave analysis results have pointed out that the fault marks the border between two different stratigraphies: in particular, NW of the of the fault higher S-wave velocity values were observed. Besides this, it is also worth mentioning the fact that the dispersion curves that were extracted from the seismic reflection lines are characterized by the presence of energetic higher modes, generally for frequencies greater than 20-30 Hz: this has had

consequences on the application of the methods considered in the present work, the MOPA technique in particular. We decided to test lateral variation detection techniques on two shots from the same seismic line whose sources are located on both sides of the main fault (Figure 5.11 and Figure 5.12). Sources locations are approximately 70 m far from the fault, and we considered the first 240 m of offset (spacing between receivers is 2 m). A topographic unevenness is also present, as the fault is located at the lower end of a 10 m slope stretching for 70 m approximately.

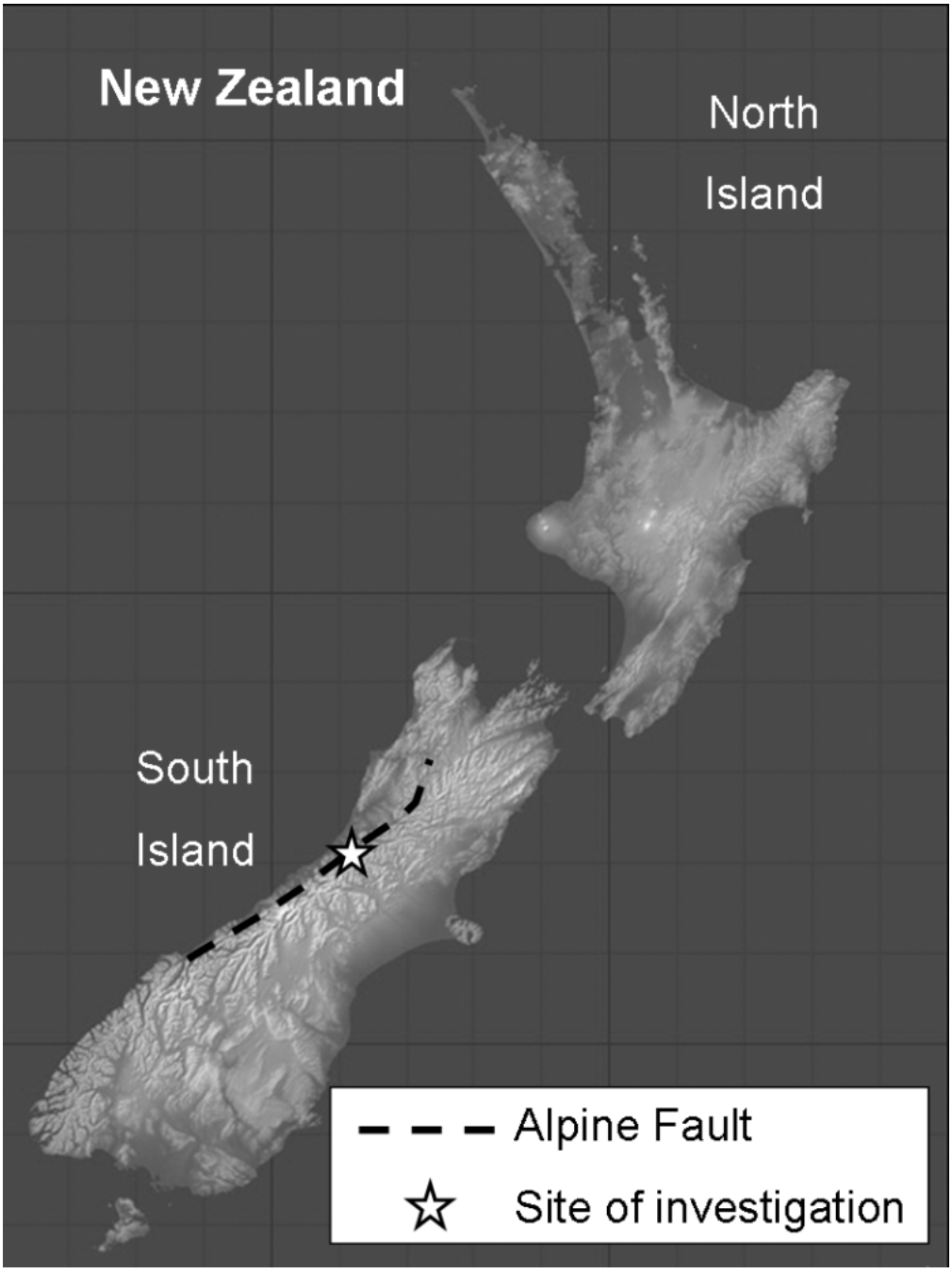

Figure 5.10 – Map of the Alpine Fault in New Zealand and location of the site of investigation.

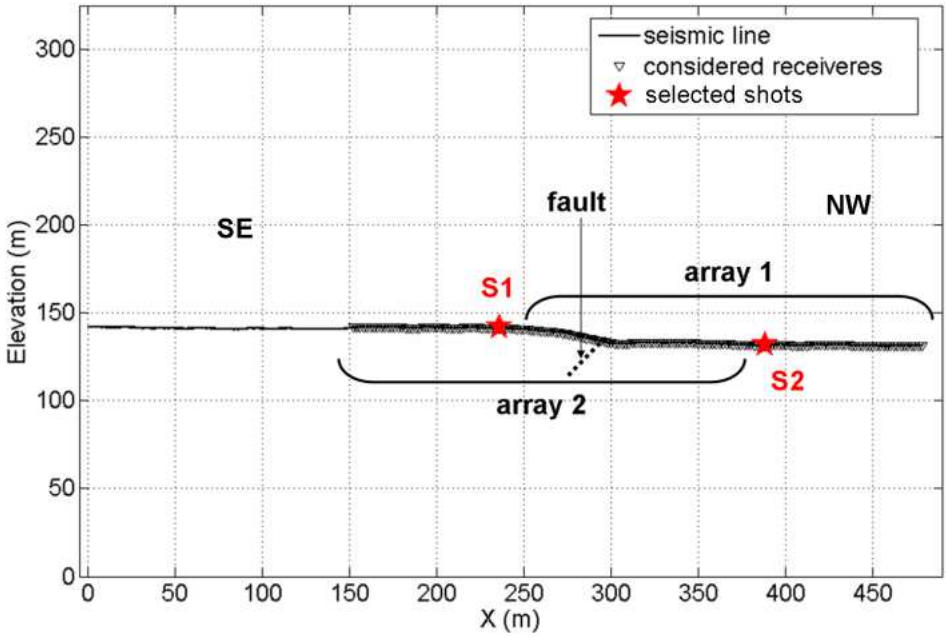

Figure 5.11 – Real case shots. S1 and S2 indicate the position of the source for shot 1 and shot 2, array 1 and array 2 denote the location of the array for shot 1 and shot 2. The seismic line stretches from south-east (SE) to north-west (NW).

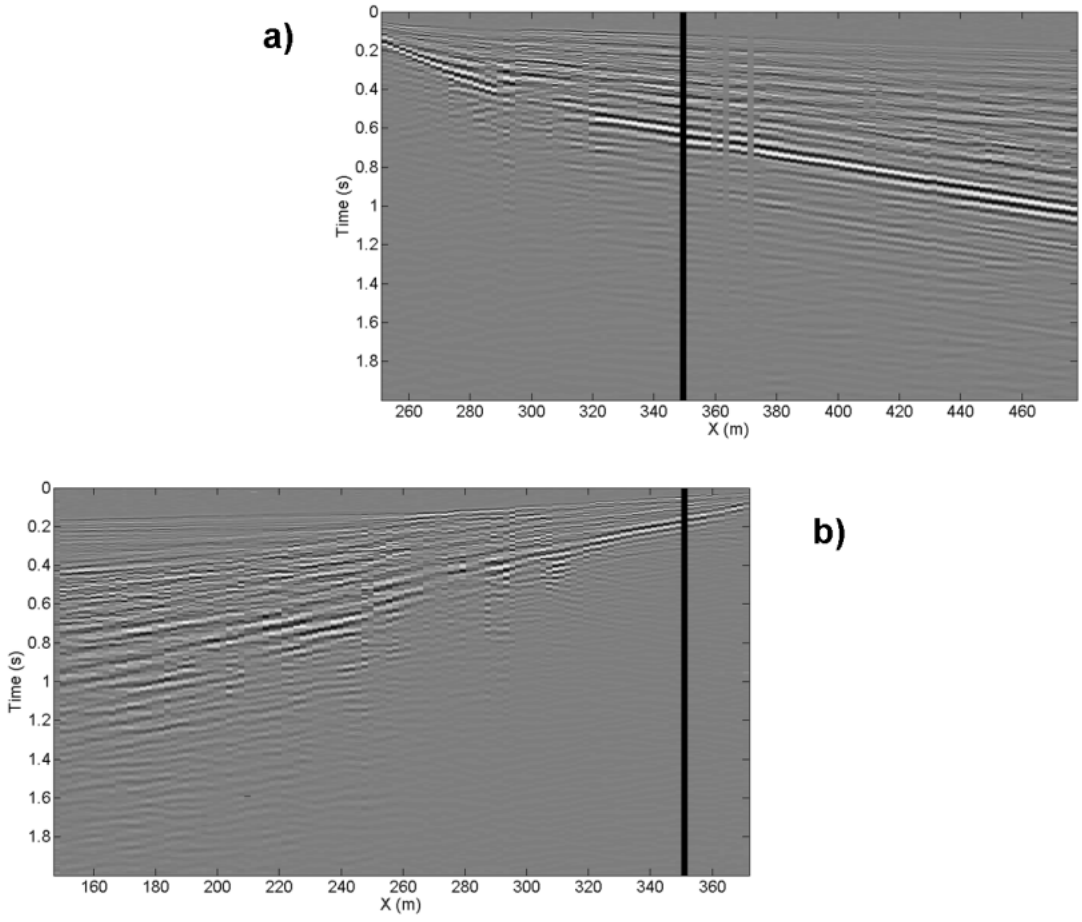

Figure 5.12 – Seismograms of the real case selected shots: shot 1 (a) and shot 2 (b).

Figure 5.13 presents the phase velocity distribution in frequency-offset domain derived from the application of MOPA on both considered seismograms. In both images a discontinuity in the phase velocity distribution is visible at about X = 300 m, marking the border between a higher velocities region (X > 300 m, NW of the fault) and a lower velocities zone (X < 300 m, SE of the fault). This result is coherent with the results of the surface wave analysis performed in the same area of the seismic line (Garofalo et al. 2011, Konstantaki 2011): in particular, the velocities retrieved by applying MOPA technique are consistent with the phase velocities of the fundamental mode of the dispersion curves extracted from the same stretch of the seismic line. In Figure 5.13 the phase velocities retrieved in the 4-20 Hz frequency range only are displayed, as for higher frequencies we obtained substantially higher velocity values, higher modes becoming energetically prevailing.

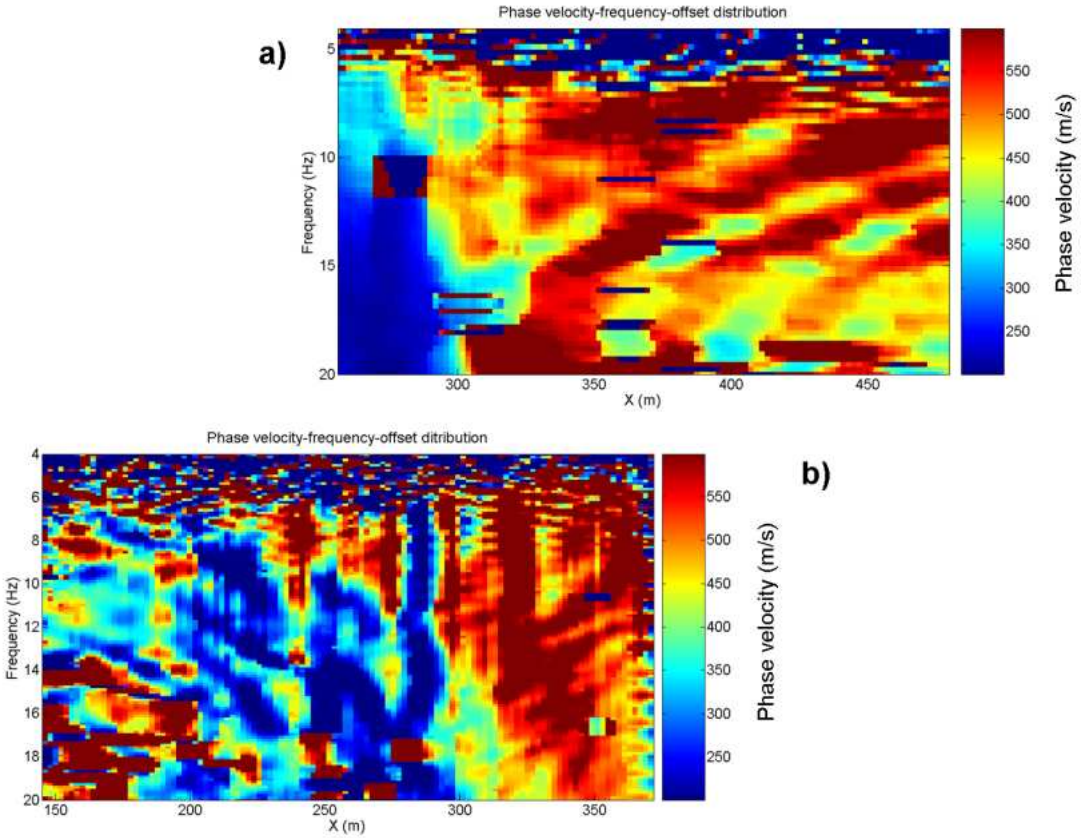

Figure 5.13 – Real data: phase velocity distribution in offset-frequency domain for shot 1 (a) and for shot 2 (b).

The presence of an abrupt discontinuity at around X = 300 m is even more clear in Figure 5.14, that shows the autospectrum plots for both shots: seimic energy clearly undergoes a dramatic decay at X = 300 m, as it is almost entirely back reflected by the fault. Unlike what has been observed for the synthetic data and by Zerwer et al. 2005,

the energy decay affects all the considered frequency range, suggesting that the fault stretches deeper than the investigation depth of surface wave (which is very approximately one half of the array length, that is 120 m in this case).

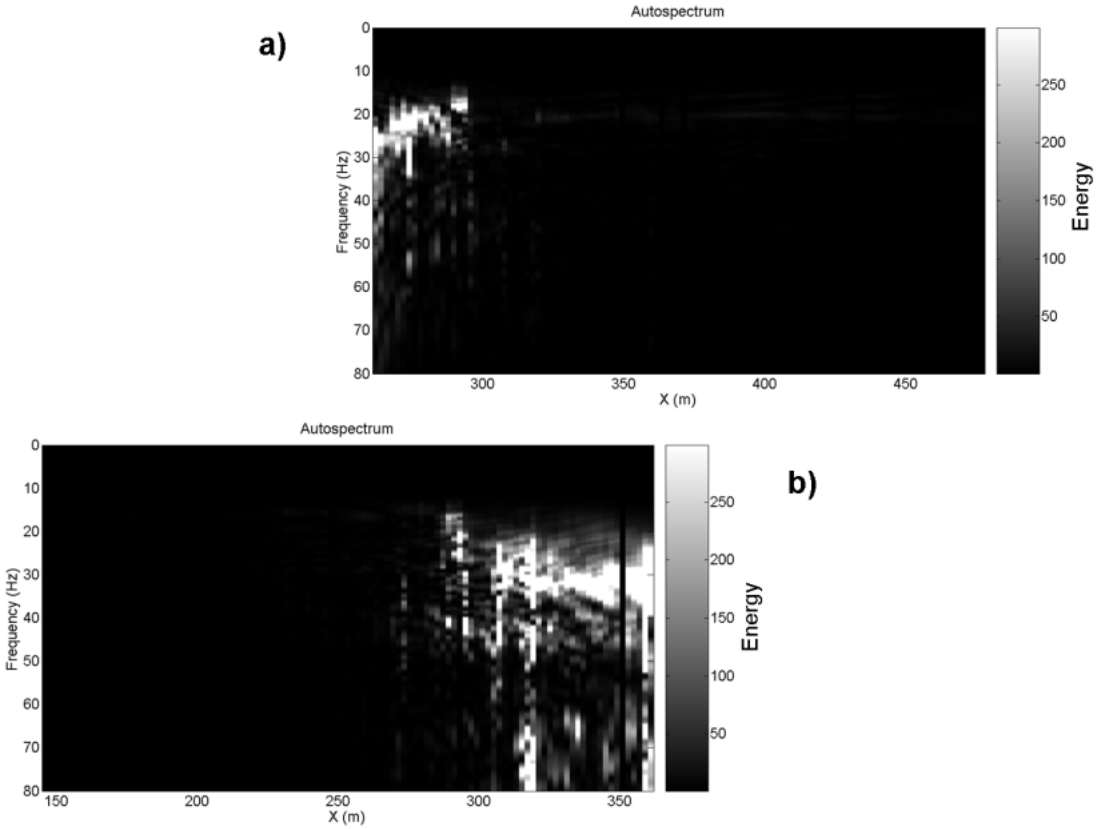

Figure 5.14 – Real data: autospectrum plots for a) shot 1 and b) shot 2.

We also generated the energy-distance graph and we plotted it on a logarithmic scale (Figure 5.15) for graphical clarity reasons. Again, sharp energy decays are visible at X = 300 m (labelled with A and B in Figure 5.15) and in both shots these decays are significantly preceded by a concentration of energy (C and D) due to the reflection of surface wave against the fault (similarly as observed by Nasseri-Moghaddam et al. 2005). We show the logarithmic decrement plots in Figure 5.16: amplification/attenuation patterns similar to the ones observed for the synthetic dataset and by Nasseri-Moghaddam et al. (2005) are visible for X < 300 m for shot 1 (Figure 5.16a) and, for X > 300 m for shot 2 (Figure 5.16b). However, they are less evident than the ones observed in the synthetic dataset LD plots (Figure 5.8) and they are present only in a limited frequency range (5-40 Hz). In Figure 5.17 we present the NALD values computed in the 2-80 Hz frequency range for both shots. The frequencies between 15 and 45 Hz appear to be the ones whose propagation is most perturbed by the presence of the fault: however, the NALD plots for the two shots are not completely

consistent with each other and a more robust estimate of frequencies most affected by the fault could be derived from the computation of the NALD plot for a greater number of shots.

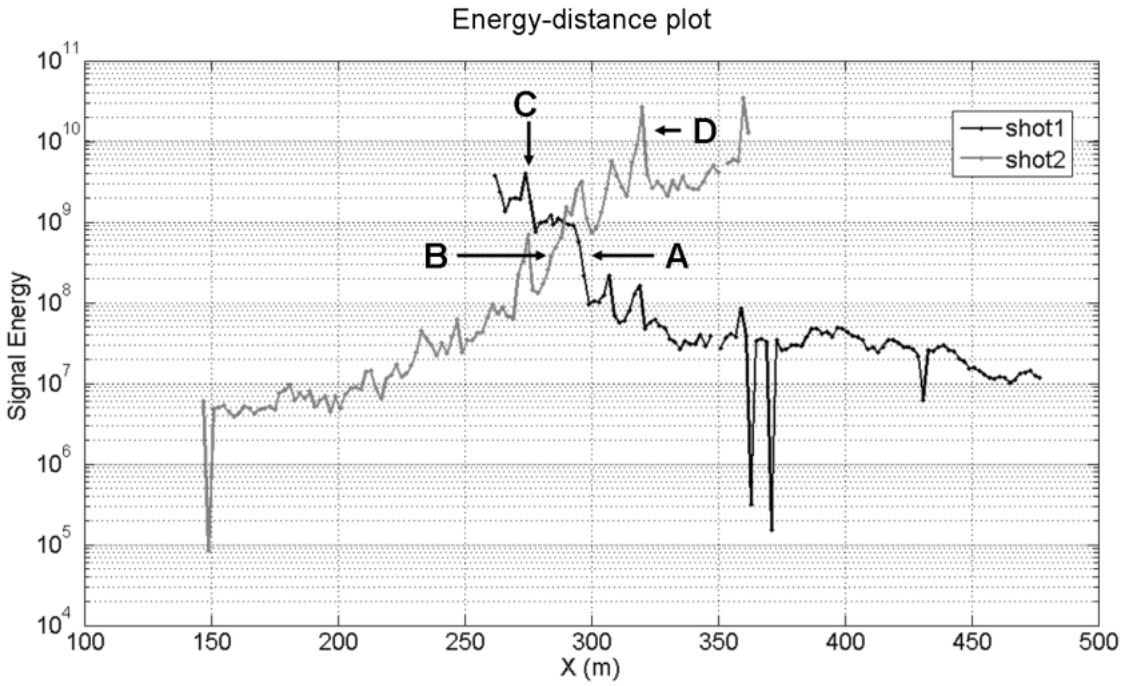

Figure 5.15 – Real data, energy-distance plot for shot 1 and shot 2. A and B label the sudden energy decay at and past the fault while C and D mark the energy accumulation right before it.

Finally, since the energy-distance plot had proven to be a simple but effective tool to estimate the position of discontinuities by retrieving energy accumulations and decays, we decided to exploit it and the data redundancy proper of a seismic reflection line dataset for a more robust and automatic detection of sharp subsoil discontinuities, as explained in the "Method" section. In Figure 5.18 we show the results of the application of the proposed procedure to the whole seismic line: in Figure 5.18a we show the trend of the energy decay exponent, computed for negative and positive offset traces and compared with the estimate of the location of the faults from seismic reflection interpretation (Figure 5.18b). Discontinuities are characterized by an energy accumulation followed by a sudden energy decay in the positive offset decay exponent graph (black line) and, at the same location, by a sharp energy decay followed by an energy accumulation in the negative offset decay exponent graph (gray line). Four faults

were detected (their approximate position is marked by a dashed line) and their location is consistent with the seismic reflection results for the same line: moreover, it should be noted that the main fault produces the most remarkable perturbations in the decay exponent plot.

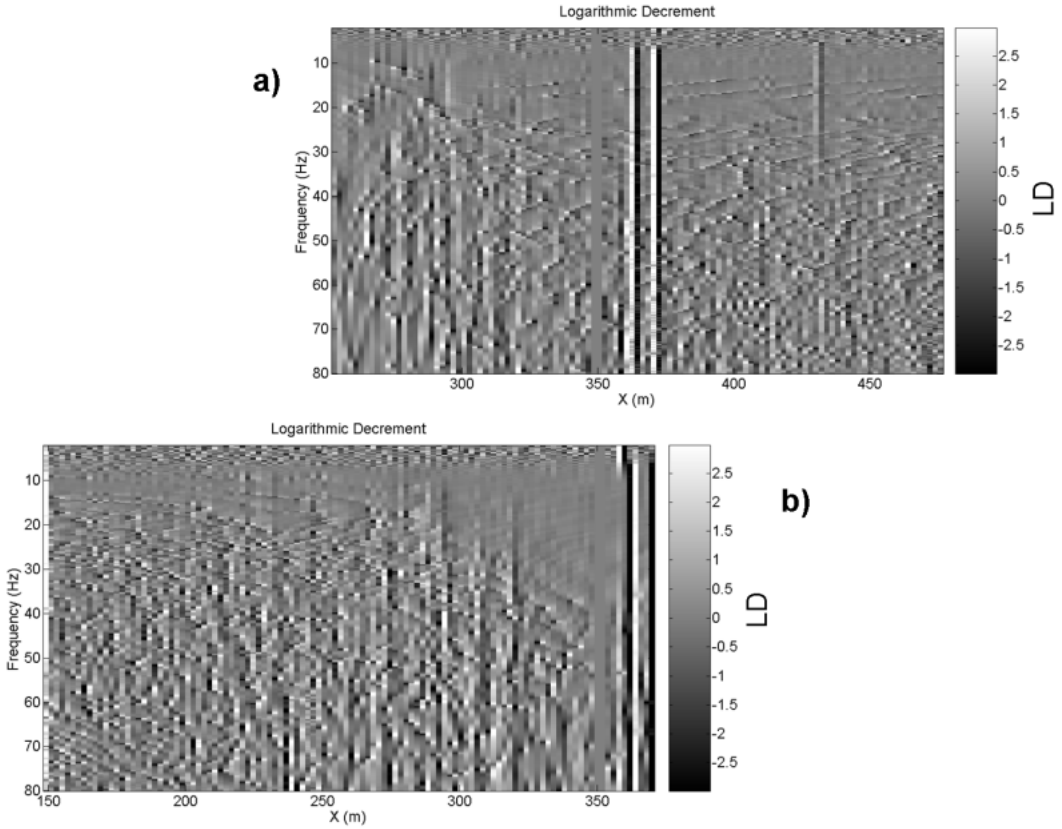

Figure 5.16 – Real data, logarithmic decrement plots for a) shot 1 and b) shot 2.

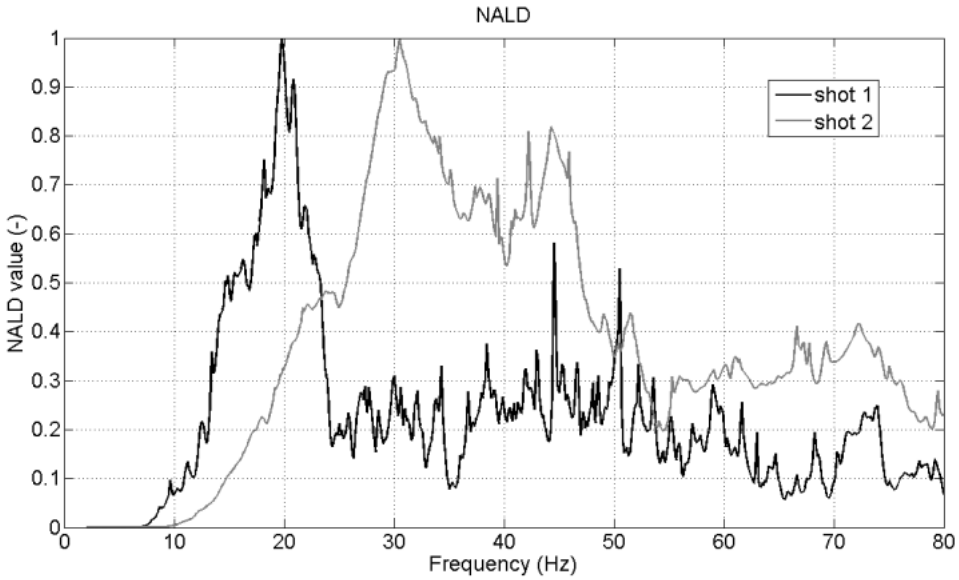

Figure 5.17 – Real data, NALD graph for shot 1 and shot 2.

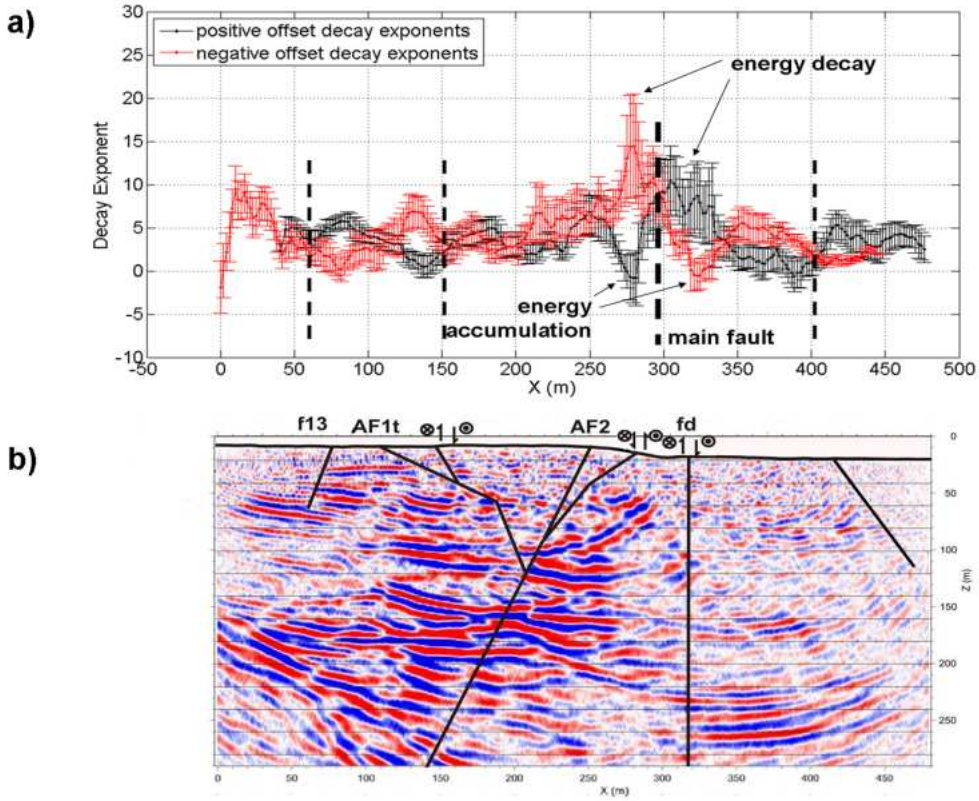

Figure 5.18 – a) Real data, positive and negative offset decay exponents plot. Continuous red and black lines join the averages of the decay exponents available for each positions and the error bars denote the corresponding standard deviations. Vertical dashed lines indicate the estimated positions of the faults; "energy accumulation" and "energy decay" labels refer to the energy trend anomalies linked to the presence of the main fault; b) seismic reflection section of the same seismic line: black continuous lines mark the location of the faults.

DISCUSSION

As far as the synthetic dataset results are concerned, they are satisfying and in good agreement with the ones presented in the papers that introduced the methods applied in the present work (Nasseri-Moghaddam et al. 2005, Zerwer et al. 2005 and Vignoli et al. 2011): we could thoroughly analyze the phenomena linked to the effects produced by a sharp lateral variation on the surface wave propagation. All methods yielded consistent information on the location and embedment depth of the discontinuity (Figures 5-9) : besides, we could also appreciate the differences in the surface wave propagation and attenuation depending on the direction the direct wave front approaches the step (Figures 6-8). As we moved to the real dataset, MOPA, the autospetrum method and the

energy distance analysis (Figures 13-15) proved to be equally effective as in the synthetic case: on the contrary the logarithmic decrement method for the detection of the interferences between direct and back reflected wave trains turned out to be less robust and more sensitive to noise, as well as the NALD computation (Figures 16 and 17). Finally, we got promising results from the procedure we developed to apply the energy-distance analysis to large datasets involving multifold 2D acquisition (Figure 5.18): a strategy to overcome the relative weakness of the logarithmic decrement plot and of the NALD would be to adapt them to such datasets to exploit their redundancy.

CONCLUSIONS

We applied to real and synthetic data three methods for the detection of sharp lateral variations exploiting anomalies in surface wave propagation and attenuation. The considered methods are the phase analysis of surface wave (MOPA), the autospectrum computation and the attenuation analysis of Rayleigh waves (AARW). These methods were developed for different purposes and different scale problems, but we applied them to the same datasets (a synthetic data from a FEM simulation and a real dataset from a seismic reflection line) to compare their results and test their effectiveness in a particular condition: the two sets of data, in fact, share the presence of an abrupt lateral variation (in the real case, a seismic fault) perpendicularly crossing the acquisition line. All three methods proved to be effective for the detection of the location of the discontinuity, by portraying phenomena linked to the presence of the heterogeneity, such as the interaction between forward and reflected wave trains, and energy concentration and subsequent decay at the fault location. Moreover, additional information were retrieved, such as the embedment depth and the sharpness of the retrieved discontinuity. The results we got, disregarding the scale and the geometry of the applications, are consistent with the results presented in the papers that originally introduced the methods. Finally, we developed the attenuation analysis of Rayleigh waves method by proposing a procedure allowing to effectively and quickly apply the AARW to large and redundant datasets (such as seismic reflection datasets) for the detection of sharp lateral discontinuities. Even though we could apply this novel procedure to the real case dataset only, results are satisfying and encourage further developments.

REFERENCES

Bohlen T,, Kugler S., Klein G. and Theilen F. 2004. 1.5 D inversion of lateral variation of Scholte-wave dispersion. Geophyiscs, vol. 69, no. 2, pp. 330-344.

Boiero D., 2010. Surface Wave Analysis for Building Shear Wave Velocity Models, PhD thesis, Politecnico di Torino.

Bergamo P., Boiero D., Socco L.V., 2010. Retrieving 2D structures from surface wave data by means of a Space-varying spatial windowing. EAGE Near Surface 2010, September 6-8 2010, Zurich Switzerland.

Carpentier S., Green A., Horstmeyer H., Kaiser A., Hurter F., Langridge R., Finnemore M. 2010. Reflection seismic surveying across the Alpine Fault immediately north of the intersection with the Hope Fault. EAGE Near Surface 2010, September 6-8 2010, Zurich Switzerland.

Garofalo F., Socco L.V., Bergamo P., Konstantaki L.A. and Carpentier S.F.A. Surface wave analysis over a fault system in New Zealand. In: proceedings of 30th GNGTS, , 30th GNGTS, 14-16 November 2011, Trieste Italy

Konstantaki L.A. 2011. Determining hydrological and soil mechanical parameters from multichannel surface wave analysis across the Alpine Fault at Inchbonnie, New Zealand. Master thesis at ETH Zurich.

Maraschini M., Ernst F., Foti S., Socco L.V. 2010. A new misfit function for multimodal inversion of surface waves. Geophysics 75, G31-G43.

Nasseri-Moghaddan A., Cascante G. and Hutchinson J. 2005. A new quantitative procedure to determine the location and embedment depth of a void using surface waves. Journal of Environmental and Engineering Geophysics 10, 51-64.

Socco L.V., Boiero D., Foti S. and Wisén R. 2009. Laterally constrained inversion of ground roll from seismic reflection records. Geophysics, vol. 74, pp. 35-45.

Strobbia C. and Foti S. 2006. Multi-offset phase analysis of surface wave data (MOPA). Journal of Applied Geophysics, 59, pp. 300-313.

Vignoli G. and Cassiani G. 2010. Identification of lateral discontinuities via multi-offset phase analysis of surface wave data. Geophyiscal Prospecting., 58, pp.389-413.

Vignoli G., Strobbia C., Cassiani G. and Vermeer P. 2011. Statistical multi offset phase analysis for surface –wave processing in laterally varying media. Geophyics, vol. 76, no. 2, pp. U1-U11.

Zerwer A., Polak M.A. and Santamarina J.C. 2005. Detection of surface breaking cracks in concrete members using Rayleigh waves. Journal of Environmental and Engineering Geophysics, vol. 10, issue 3., pp. 295-306.

CONCLUSIONS

In the present work I have presented a series of procedures and processing tools to enhance the reliability of the surface wave (SW) method when investigating 2D structures in the subsoil.

I propose some methods to face both smooth lateral variations and sharp changes in materials properties in the subsoil. As suggested by literature, I adopted two different strategies, one to handle gentle changes in subsoil geometry and one devoted to abrupt discontinuities. In the first case, the aim is following the lateral variability of subsoil seismic parameters. I therefore developed a procedure able to retrieve 2D structures from SW acquired with a limited number of receivers by extracting a set of neighbouring local dispersion curves out of a single seismogram. The technique consists of the extraction of local dispersion curves along the survey line using a spatial windowing based on Gaussian windows with different maximum position; every curve therefore refers to a slightly different subsurface portion, so that gradual changes in subsoil seismic parameters can be reconstructed through the dispersion curves inversion. I thoroughly studied the consequences of the spatial windowing both on the lateral resolution of the dispersion curves and on the wavenumber resolution of the relevant *f-k* spectra (which is linked to the possibility to distinguish two different events in the *f-k* domain and to the maximum investigation depth): I pointed out the clash between the two resolutions (the more one is fostered, the more the other worsens and vice versa) and the necessity to find a compromise to ensure a correct and accurate description of the subsoil lateral variations. I therefore provided a chart quantitatively representing the relationship existing among the Gaussian windows width, the lateral resolution and the wavenumber resolution they ensure. In the context of characterizing smooth 2D structures in the subsurface via the surface wave method, I also developed a second procedure to quantitatively estimate the lateral variability of model parameters by comparing the shape of local dispersion curves, without the need to perform their inversion. The method is based on a sensivity analysis and on the applications of the scale properties of surface wave. The procedure can be devoted to different applications: I exploited it to extend a priori punctual information to subsoil portions for which an experimental dispersion curve is available and for an estimation of the lateral variability of S-wave velocity model parameters for a set of neighbouring dispersion curves. Thanks to the first application I managed to produce a consistent initial model

based on a priori information accustomed according to local SW data; the evaluation of the expected spatial variability of model parameters was used to provide a data-consistent setting of the lateral constraints for a laterally constrained inversion. Switching from gradual and smooth to abrupt and sudden lateral variations, I focused my attention on the estimation of the location and of the embedment depth of such heterogeneities, in order to process separately the traces belonging to quasi 1D subsoil portions and therefore to overcome the drawbacks caused by sudden changes in subsoil materials properties on SW method. I used three methods (multi-offset phase analysis of surface wave or MOPA, autospetrum method and attenuation analysis of Rayleigh waves or AARW) all of them exploiting the detection of anomalies in surface wave propagation by means of the analysis of phase and power spectra of the recorded seismograms. Although developed for different purposes and different scales, I adapted them to the detection of discontinuities in the subsoil by means of near-surface characterization surveys.

The aforementioned algorithms were first tested on synthetic datasets and then applied to real data. In one case, the algorithm was also tested on seismograms derived from a small scale seismic survey performed on an analogue model.

I applied the procedure to reconstruct smooth lateral variations by means of a spatial windowing to three synthetic datasets extracted from models with an increasing degree of complexity in 2D structures and on a real case: I was able to reliably retrieve the 2D behaviour of the S-wave velocity in the subsurface. However, particularly when commenting on synthetic data results, I felt the necessity to adopt a laterally constrained inversion (LCI) algorithm and tune the lateral constraints according to the expected lateral variability of the model parameters, adapting the constraints to the physical reality of the materials properties in the subsoil. I finally managed to provide a tool to estimate the overall trend of the model parameters by exploiting the scale properties of surface waves. The same procedure was also applied to a dataset obtained from a small scale seismic experiment performed on an analogue model. The two main tasks of the experiment were a) to produce a small scale physical model constituted by granular materials and characterized by lateral heterogeneities and b) to obtain a characterization of the model itself by means of surface wave analysis, also applying the aforementioned technique to handle its 2D structure. Both goals were achieved, and the technique based on Gaussian windows proved to be effective in producing a good pseudosection of the S-wave velocity behaviour of the model.

In a similar fashion, I first tested the algorithm I developed to quantitatively estimate the lateral variability of model parameters by comparing the shape of local dispersion curves on two synthetic datasets from numerical simulations; later, I applied the same procedure to a real case, again a seismic reflection survey. In all cases I exploited the algorithm to customize punctual a priori information according to the available experimental dispersion curves and to estimate the spatial variability of model parameters. As far as the synthetic data results are concerned, in both cases I got a satisfactory description of the global trend of model parameters. I then applied the method to the real case, managing to spread the a priori information provided by two down-hole test to the whole set of dispersion curves extracted from a seismic reflection line. The reliability of this result is confirmed by its agreement with other geophysical survey and data processing results available for the same site. However, despite the good results retrieved from real and synthetic data, further work is needed to make the whole procedure more robust and less sensitive to data quality.

As for the detection of sharp heterogeneities, I applied the selected methods (MOPA, AARW and autospectrum method) to a synthetic dataset, obtained from a FEM simulation on a model with an abrupt lateral variation, and on real data from a seismic reflection survey acquired over a fault in New Zealand. I got meaningful and consistent results from the three methods, similar to the ones observed in their original applications. I was able to investigate the anomalies in Rayleigh wave propagation due to the presence of an abrupt discontinuity in the subsoil, to estimate its location and embedment depth. Being the real dataset a multifold seismic acquisition, I partly adapted one of the methods (AARW) to such datasets to exploit their data redundancy. A further development of the work will be to fully customize the whole procedure to multifold datasets to enhance the robustness of its results.

On the whole, this thesis provides several processing tools for the improvement of the reliability of the surface wave method, particularly suitable for its applications to near surface subsoil characterization by means of active surveys. In particular, these tools aim at mitigating the effects of the 1D approach proper of SW method, so that it can be effectively applied to laterally varying media. A future development of the work would extend these tools to 3D seismic data.